UNIVERSITY OF CALIFORNIA SAN DIEGO

A Molecular Perspective on Ion Hydration

A dissertation submitted in partial satisfaction of the
requirements for the degree of Doctor of Philosophy

in

Chemistry

by

Pushp Bajaj

Committee in charge:

       Professor Francesco Paesani, Chair
       Professor Seth Cohen
       Professor Michael Gilson
       Professor John Weare
       Professor Wei Xiong

2018

ProQuest Number: 10837753

ProQuest 10837753

The Dissertation of Pushp Bajaj is approved and is acceptable in quality and form

for publication on microfilm and electronically:

_____

_____

_____

_____

_____
Chair

University of California San Diego

2018

TABLE OF CONTENTS

LIST OF FIGURES

ACKNOWLEDGEMENTS

I first and foremost would like to thank my doctoral research advisor, co-author, mentor, and role model, Professor Francesco Paesani. I feel privileged to have been a part of your research group and have access to all the resources and collaboration opportunities. I will forever be grateful for the knowledge and wisdom that you have given me over the years of my PhD. Most of all, you made me understand the meaning and importance of living with a purpose and following my passion which will surely help me make better decisions in the future.

I would also like to thank Dr. Andreas W. Götz, whom I have always considered to be a second mentor. I developed most of my computer programming skills early on under your guidance which helped me greatly during my PhD. I also learned a lot from you about how to be organized and rigorous in my academic and personal life.

Francesco; "Halide ion microhydration: structure, energetics and spectroscopy of small halide-water clusters". The dissertation author was the primary investigator and author of this material.

Finally, I would like to thank my family, friends and group mates for their constant support and encouragement during my PhD.

VITA

2011	Bachelor of Science in Chemistry, University of Delhi, India
2013	Master of Science in Chemistry, Indian Institute of Technology Madras, India
2013–2018	Teaching Assistant, Department of Chemistry and Biochemistry University of California San Diego
2013–2018	Research Assistant, University of California San Diego
2018	Doctor of Philosophy in Chemistry, University of California San Diego

PUBLICATIONS

Medders, G. R., Götz, A. W., Morales, M. A., Bajaj, P., Paesani, F., "On the Representation of Many-Body Interactions in Water", *J. Chem. Phys.*, 143, 104102, **2015**.

Arismendi-Arrieta, D. J.†, Riera, M.†, Bajaj, P.†, Prosmiti, R., Paesani, F., "i-TTM Model for Ab Initio-Based Ion-Water Interaction Potentials. 1. Halide-Water Pontential Energy Functions ", *J. Phys. Chem. B*, 120, 1822, **2016**.

Bajaj, P., Götz, A. W., Paesani, F., "Toward Chemical Accuracy in the Description of Ion-Water Interactions Through Many-Body Representations. 1. Halide-Water Dimer Potential Energy Surfaces", *J. Chem. Theory Comput.*, 12, 2698, **2016**.

Reddy, S. K., Straight, S. C., Bajaj, P., Pham, H. C., Riera, M., Moberg, D. R., Morales, M. A., Knight, C., Götz, A. W., Paesani, F., "On the Accuracy of the MB-pol Many-Body Potential for Water: Interaction Energies, Vibrational Frequencies, and Classical Thermodynamic and Dynamical Properties from Clusters to Liquid Water and Ice", *J. Chem. Phys.*, 145, 194504, **2016**.

Riera, M., Mardirossian, N., Bajaj, P., Götz, A. W., Paesani, F., "Toward Chemical Accuracy in the Description of Ion-Water Interactions Through Many-Body Representations. Alkali-Water Dimer Potential Energy Surfaces", *J. Chem. Phys.*, 147, 161715, **2017**.

Bajaj, P., Wang, X-G., Carrington Jr., T., Paesani, F., "Vibrational Spectra of Halide-Water Dimers: Insights on Ion Hydration from Full-Dimensional Quantum calculations on many-body potential energy surfaces", *J. Chem. Phys.*, 148, 102321, **2018**.

Bajaj, P., Richardson, J. O., Paesani, F., "Ion-Mediated Hydrogen Bond Rearrangement Through Tunneling in the Iodide Dihydrate Complex", *Nature Chemistry*, under review.

FIELDS OF STUDY

Major Field: Chemistry (Physical Chemistry)

Theoretical and Computational Chemistry
Professor Francesco Paesani

ABSTRACT OF THE DISSERTATION

A Molecular Perspective on Ion Hydration

by

Pushp Bajaj

Doctor of Philosophy in Chemistry

University of California San Diego, 2018

Professor Francesco Paesani, Chair

Hydration of anions, particularly halide ions, presents a particularly challenging problem where due to strong intermolecular interactions the ion can significantly alter the hydrogen bonding network of water. The extent to which varies greatly depending on the nature of ion-water interactions. An accurate description of the interplay between ion-water and water-water interactions is necessary to achieve a molecular level understanding of ion hydration. In this work, we present a bottom-up analysis of the structure, energetics, vibrational spectroscopy and hydrogen bond arrangement of small halide-water clusters ($X^-(H_2O)_n$, $X^- = F^-$, Cl^-, Br^-, I^-) using state-of-the-art computational chemistry tools. We begin by developing *ab initio* based many-body potential energy functions PEFs, called MB-nrg, for describing halide-water

intermolecular interactions that include many-body effects for all system sizes by taking into account explicitly the two-body and three-body interactions, and all higher order interactions implicitly through a mean field approximation.

To directly probe the strength of halide-water intermolecular interactions, full dimensional vibrational spectra are calculated for both $X^-(H_2O)$ and $X^-(D_2O)$ dimers at the quantum-mechanical level. Followed by an analysis of the structure, hydrogen bond arrangement and temperature dependent dynamics of the $I^-(H_2O)_2$ and $I^-(D_2O)_2$ through quantum path integral molecular dynamics simulations. Tunneling pathways leading hydrogen bond rearrangement were identified and the corresponding tunneling splitting patterns were calculated using the ring polymer instanton method. Finally, we studied the structural, thermodynamic and spectroscopic properties of small $X^-(H_2O)_n$ clusters where $X^- = F^-$, Cl^-, Br^-, I^-), n=3-6, using replica exchange molecular dynamics simulations. Across all sizes, fluoride-water clusters exhibit qualitatively different structures and properties compared to the chloride-, bromide- and iodide-water clusters which, on the other hand, are found to be similar to each other. This is a direct consequence of the exceptionally strong fluoride-water intermolecular interactions, which significantly affect the water-water hydrogen bonding strength and arrangement in the vicinity. Through extensive comparisons between the MB-nrg PEFs and classical polarizable force fields and approximate *ab initio* methods like density functional theory and MP2, our results emphasize the importance of an accurate description of the quantum mechanical many-body intermolecular interactions for a robust molecular level understanding of halide ion hydration. Follow-up studies of larger cluster sizes will focus on the evolution of the hydration shells in a systematic way.

Introduction

Water is ubiquitous in nature and often mediates fundamental chemical, biological, and environmental processes. Due to many extraordinary physical and chemical properties, it is by all accounts different from all other liquids. Most of the anomalous properties of water, including the unusually high boiling and melting points, the unusually high surface tension, the higher density of solid water compared to liquid water, the different phases of solid water, and others, are related to its ability to form flexible and extended hydrogen bond networks in the condensed phase. Electrolytes dissolved in water dissociate into ions that are hydrated. Depending on the charge, size and nature of the specific atomic/molecular ions, they can significantly alter the structure and dynamics of the water molecules around them, with direct implications in biology, atmospheric sciences and electrochemistry.[3–6]

Aqueous Ca^{2+}, Na^+, K^+ and Mg^{2+} ions play a key role in biological processes in mammals that are responsible for the rigidity and hardness of bones and teeth, blood clotting, muscle contraction, transport of water and nutrients through cell membranes and transmission of nerve impulses. Anions like Cl^- and PO_4^{3-} are also important in maintaining the acid-base balance of blood, water balance of the body, formation of bones and teeth and in transfer and storage of energy in ATP. In the atmosphere, ions are involved in numerous chemical reactions that affect the production and composition of trace gases, the oxidation of Cl^- to Cl_2 in sea-salt aerosol particles contributes to ozone formation in the polluted marine boundary layer,[7,8] halogen chemistry is also responsible for tropospheric ozone layer depletion,[9] hydrolysis of SO_2 in cloud droplets produces sulfuric acid which leads to acid rain.[10] Sea spray aerosol (SSA) particles that are ejected into the atmosphere by the breaking of waves in the ocean consist primarily of

aqueous inorganic ions. Specific ions and their concentration impacts the size, composition and physical and chemical properties of SSA particles. These particles impact our climate directly by scattering incident solar radiation and indirectly by changing cloud properties.[11]

In terms of their effects on the structure of water, ions are typically classified as kosmotropes (structure-makers) and chaotropes (structure-breakers). Kosmotropes are generally ions with high charge density which have the ability to order the surrounding water molecules, while chaotropes are ions which disrupt the hydrogen-bond network of liquid water.[12,13] However, a strong consensus about the extent to which specific ions affect the structure of water beyond the first hydration does not exist.

Another aspect of ion-hydration that has remained elusive is the propensity of specific ions to the solution-air interface. Until about 20 years ago, it was commonly assumed that ions are repelled from the air-water interface and prefer to remain hydrated in the bulk. However, more recent MD simulations with polarizable interaction models predicted small hard ions with high charge density (such as alkali cations or fluoride) are indeed repelled from the aqueous surface. But, other heavier soft anions (like heavier halides) show a significant propensity towards the interface.[14–17] Ions present at the surface can then participate in interfacial reactions which can lead to exciting chemistry across biological and atmospheric interfaces. Experimental measurements of the second harmonic generation (SHG), vibrational sum-frequency generation (VSFG), and photoelectron spectroscopy have since validated the predictions of the simulations.[18–23] Although, a general agreement on the propensity of more polarizable ions to go to the surface is well established, a quantitative description of the factors responsible for this behavior is yet to be achieved. The results from theoretical and computational studies vary greatly depending on the particular interaction model used to describe the ion-water and water-water interactions.[6,24,25]

0.1 Studying ion-hydration using computer simulations

Understanding the structure and properties of aqueous systems across phases has been a monumental and long sought-after goal. In this regard, computational chemistry and molecular dynamics techniques have emerged as extremely useful methods to gain insights into the structure and dynamics, at the molecular level. This is a particularly challenging problem from a theoretical and computational point of view because for a quantitative analysis not only does one require an accurate potential energy surface describing the anharmonic and quantum mechanical effects in intermolecular interactions, but also a robust way of including the nuclear quantum effects in the molecular dynamics simulations. Despite much progress, a quantitative description of how specific ions interact with water remains an outstanding challenge.

Among the commonly used interaction models for ion-hydration, empirical potential energy functions or force fields (FFs) are typically made up of terms for the hard-core repulsive and attractive dispersion forces using Lennard-Jones potentials, and coulomb interactions between fixed charges on the ions and water molecules. Polarization effects are accounted for explicitly by induced dipoles[16,26–31] or Drude oscillators.[32–35] The FFs are usually parametrized to reproduce particular structural and thermodynamic properties of bulk solutions[16,31,36] of particular ions and may not be transferable to other ions or other environments, for instance gas phase clusters or interfaces. The parameters in FFs often need to be fine tuned to reproduce the experimental data which limits the scope and makes them less robust. *Ab initio* or first principles methods typically based on Density Functional Theory (DFT) have also been used to perform molecular dynamics simulations of aqueous ionic systems. However such studies are often limited to small system sizes due to the prohibitively high computational cost of ab initio molecular dynamics (AIMD) simulations. Moreover, the functional form and accuracy of the particular electronic structure method must also be taken into account when interpreting the results from such simulations.

In this regard, we have recently undertaken the development of full-dimensional ion-water potential energy functions (PEFs), called MB-nrg[37] (for Many-Body-energy), which are derived

entirely from correlated electronic structure data with the goal of accurately and systematically describing the properties of ion-containing aqueous systems from the gas phase to the condensed phase. The MB-nrg PEFs are built upon the many body expansion of the total energy which is discussed in detail in Section 0.2 below.

0.2   Many-body representation of the total energy

The many body expansion of the total energy (MBE)[38] of any N-molecule system (or N-mer) is a formally exact expression that is composed of individual terms of the one-body (1B), 2-body (2B), 3-body (3B) and so on, up to the N-body (NB) interaction energies.

$$E_{N-mer}(1,...,N) = \sum_i^N V^{1B}(i) + \sum_{i<j}^N V^{2B}(i,j) + \sum_{i<j<k}^N V^{3B}(i,j,k) + ... + V^{NB}(i,..,N) \quad (1)$$

where, $V^{1B}(i') = E_{mon}(i')$ corresponds to the potential energy of the internal distortions of individual molecules or "monomers" from their equilibrium geometry. This 1B term depends on all the 3M atomic coordinates of the molecule, where M is the number of atoms in the molecule, and they are collectively referred to by a single index, i. The sum over all such 1B contributions from all the molecules, which could be same (in a homogenous system) or different (in a heterogenous system), in the N-molecule system, makes the total one-body contribution. The higher-order, $V^{2B}(i,j)$, $V^{3B}(i,j,k)$, ..., $V^{NB}(i,...,N)$ terms, correspond to interactions between groups of 2, 3, ..., N interacting monomers, called "dimers", "trimers", ..., "N-mers".

In the MBE in equation 1, the higher-order interactions can be derived recursively through the lower-order terms, as described below for the 2B and 3B interaction energies:

$$\begin{aligned}
V^{2B}(i',j') &= E(i',j') - (V^{1B}(i') + V^{1B}(j')) \\
&= E(i',j') - (E(i') + E(j'))
\end{aligned} \quad (2)$$

where, $E(i', j')$ is the energy of the (i', j') dimer,

$$
\begin{aligned}
V^{3B}(i', j', k') &= E(i', j', k') - (V^{2B}(i', j') + V^{2B}(i', k') + V^{2B}(j', k')) \\
&\quad - (V^{1B}(i') + V^{1B}(j') + V^{1B}(k')) \\
&= E(i', j', k') - (E(i', j') + E(i', k') + E(j', k')) \\
&\quad + (E(i') + E(j') + E(k'))
\end{aligned}
\tag{3}
$$

where, $E(i', j', k')$ is the energy of the (i', j', k') trimer.

The MBE has been shown to converge to quickly for most insulators, including water, with most of the contribution to the total energy coming from up to the three-body interactions.[39–42] Due to the absence of long-range order in non-conductors, the higher-body interactions exhibit negligibly small contributions. This allows for a stratified or even truncated approach to calculating interaction energies of large N-body systems using cheaper and lower levels of electronic structure methods to compute the higher-order terms or even neglecting them altogether.[43–45] This provides a computationally cheaper alternative to the canonical supermolecular approach to calculating interaction energies, i.e. subtracting the energies of the monomers from the cluster total energy.

0.3 Molecular level aspects of ion hydration

Over the past couple of decades, advances in computational chemistry and experimental spectroscopy techniques have made it possible to study the hydration phenomena of charged species at the molecular scale. Hydration of anions, specifically halide ions, presents a particularly interesting and also challenging problem as they can participate in strong hydrogen bonding with the water molecules and significantly alter the structure and dynamics of the system in their vicinity. The nature of anion-water interactions is strikingly different from cation-water interactions. Strong electrostatic forces, charge transfer and many-body effects dominate the physics and chemistry. Whether these effects extend beyond the first hydration shell has been

5

a topic of much debate in the literature. In this context, studies of small gas-phase clusters can provide molecular level insights into the fundamental questions regarding intermolecular interactions, energy transfer and reactivity. Studying ionic clusters with increasing cluster size also provides a systematic *bottom-up* approach to understanding ion hydration in bulk solutions and interfaces. From a theoretical perspective, these small systems also act as model systems which can be used to test and validate ion-water interaction potentials.

Early experimental work in this area, used temperature-controlled, high pressure mass spectrometry and flow tubes to obtain thermodynamic data such as enthalpies, entropies and free energies of step-wise solvation of ions.[46–50] The structure and coordination numbers of the first hydration shell were determined for several positively and negatively charged ions, by studying the solvation free energies as a function of number of solvent molecules. However, these studies were limited in their ability to study ions in larger clusters, with greater than eight water molecules. Following that photoelectron spectroscopy emerged as another useful technique to probe the energetics of the formation of hydration shells around negatively charged ions.[51–55] It can measure the binding energy of the anionic electron in the cluster, which is directly influenced by the ion-solvent interaction strength, distance and orientation. Solvent-solvent interactions have hardly any effect on the energetics since photoelectron ejection occurs at very fast time scales, faster than the relaxation times of solvent molecules. Additionally, photoelectron spectroscopy is a general technique, and can be extended to large clusters containing hundreds of solvent molecules and bulk systems.

More recently, infrared spectroscopy has become an extremely powerful diagnostic tool to study the structure and hydrogen bond topology of aqueous ionic clusters and directly probe the strength of ion-water interactions, due to the high sensitivity of OH stretch to the local environment. Anions can participate in strong hydrogen bonding with water resulting in the characteristic red shift of the OH stretch frequencies in the vibrational spectrum, which can be as large as a couple of hundred wavenumbers. In the early 1990s, several research groups reported the vibrational spectra of $X^-(H_2O)_n$ clusters using the predissociation or photoinduced

water monomer evaporation technique. However, the initial anion cluster spectra for more than one water molecule and strongly bound complexes were found to be quite diffuse compared to the distinct vibrational bands displayed by both neutral and cationic clusters in the same size range, such that quantitative assignments were not possible. Later experiments, using argon predissocation or "messenger" technique provided the breakthrough to beautifully resolved spectral features in the OH stretching region which could be measured for the first time for anionic clusters across a wide range of clusters sizes. These spectra have now become the "gold standard" for validation ion-water interaction models.

Numerous computational studies have helped understand the experimental observations, providing a molecular level picture, focussed on the structure and spectroscopy of small halide-water clusters. Much effort has been made to identify the various structural isomers of these clusters, their thermodynamic properties and vibrational spectra for comparisons with experiments. The structures of the small halide-water clusters have been a topic of much controversy around the surface or internal state of the halide ion. The general understanding is that heavier, weakly interacting halides tend to stay on the surface while lighter, strongly interacting halides prefer internal arrangements. However, a quantitative, unified experimental and theoretical picture remains elusive. The balance between halide-water and water-water intermolecular interactions, and non-additive many-body effects play a key role in determining the arrangement of water molecules around the ion. Due to the relatively small number of atoms in such systems, they can be studied efficiently using *ab initio* methods, unlike the large bulk systems.

0.4 Summary

This dissertation focuses on the development and applications of the MB-nrg halide-water PEFs, derived entirely from highly accurate explicitly correlated coupled cluster (CCSD(T)-F12) calculations, in simulations of halide-water systems across all phases. In Chapter 2, the two-body (2B) term of the MB-nrg PEFs is presented in detail. Comparisons of $X^-(H_2O)$ (X^- =

F$^-$, Cl$^-$, Br$^-$, I$^-$) dimer interaction energies and harmonic vibrational frequencies are made with other polarizable force fields and with commonly used density functional theory (DFT) methods to show the unmatched accuracy and consistency of the MB-nrg PEFs. In Chapter 3, full-dimensional vibrational spectra for both X$^-$(H$_2$O) and X$^-$(D$_2$O) dimers, calculated using the symmetry-adapted Lanczos algorithm with a product basis set including all six vibrational coordinates, are reported. The calculations were carried out with two sets of polarizable PEFs, TTM-nrg and MB-nrg, which differ only in their treatment of the short-range interactions. The comparison between the TTM-nrg and MB-nrg results show the importance of having an accurate representation of the quantum mechanical anharmonic effects in the short range for a correct description of the hydration phenomena at the molecular level. Moving forward to the next size cluster, Chapter 4, provides an extensive analysis of the hydrogen bonding and nuclear quantum effects in the I$^-$(H$_2$O)$_2$ trimer and its isotopologues. Quantum tunneling pathways leading to complete rearrangement of the hydrogen bonding at low temperatures, along with the corresponding ground state tunneling splitting patterns are reported for the first time. Through quantum simulations performed at increasing temperatures, the partial dissociation of the trimer is studied as it melts at high temperatures. In Chapter 5, the evolution of X$^-$(H$_2$O)$_n$ (X$^-$ = F$^-$, Cl$^-$, Br$^-$, I$^-$ and $n = 3 - 6$) clusters as a function of cluster size and temperature is studied using molecular dynamics simulations with the MB-nrg PEFs. The various minimum energy structural isomers for all X$^-$(H$_2$O)$_n$ clusters are reported, along with their corresponding vibrational spectra. The thermodynamic equilibria between the different isomers is analyzed as a function of temperature.

Chapter 1

Many-body potential energy functions for aqueous ionic systems

1.1 Introduction

As described in detail before, specific ions in water can significantly alter the structure and dynamics of the water molecules around them with implications in many chemical, biological and environmental processes. In order to achieve a molecular-level understanding of ion hydration we need an accurate and robust description of ion-water interactions across all system sizes and phases. This has been a long standing challenge in computational chemistry. While classical polarizable models are fast and can be used to study large systems and thermodynamic properties which require long simulation times, they lack the accuracy that is needed to model the real world and all its complexity to make reliable predictions. *Ab initio* methods like MP2 and coupled cluster theory are highly accurate but are intractable for large systems due to the high computational cost. Density functional methods have emerged as the cost-efficient alternatives but they lack consistency. Depending on the nature of the ion and the corresponding ion-water interactions, different DFT methods can give very different results which may or may not be reliable.

This chapter describes the many-body MB-nrg potential energy functions (PEFs) for halide-water interactions which can be used in molecular dynamics simulations of halide-water systems from the gas phase to the condensed phase and interfaces. The functional form of the

MB-nrg PEFs is discussed in detail in section 1.2. The details of the training sets used to build the two-body (2B) interaction term and the electronic structure method used to calculate the reference interaction energies for fitting, are given in section 1.3. The accuracy of the MB-nrg 2B PES is assessed in section 1.4 by comparing the energies and harmonic frequencies against previously reported models and electronic structure methods including CCSD(T)-F12, MP2 and various DFT methods.

1.2 Description of the MB-nrg model

1.2.1 The functional form

As mentioned in Section **??**, the MB-nrg[37,56] PEFs are built upon the many-body expansion (MBE), given in Equation 1, according to which the ion-water interactions are decomposed into individual contributions from the two-body (2B), three-body (3B), and so on, up to the N-body contributions. Within the MB-nrg representation, all water properties i.e., monomer distortion corresponding to the 1B contribution, dipole moment, polarizability, intermolecular water-water interactions, are described by the MB-pol potential.[57–59] MB-pol has been shown to predict the structural, thermodynamic, dynamical and spectroscopic properties of water from the gas phase to the condensed phase with unmatched accuracy.[60–65] The intermolecular ion-water 2B and 3B contributions are included explicitly, with all higher-order contributions taken into account implicitly through classical many-body permanent and induced electrostatics. The 2B term of the MB-nrg halide-water PEFs is described below and was developed in this work. The explicit 3B term of the MB-nrg halide-water PEFs will be a subject of future studies.

The 2B term includes three contributions,

$$V^{2B}(H_2O - X^-) = V^{2B}_{short}(H_2O - X^-) + V^{2B}_{TTM}(H_2O - X^-) + V^{2B}_{disp}(H_2O - X^-) \qquad (1.1)$$

Following the framework of the MB-pol potential, for consistency, the MB-nrg electrostatic term ($V^{2B_{TTM}}$) is given by a slightly modified version of the extended Thole-type model (TTM)

10

originally introduced in the TTM4-f potential.[66] In the induced electrostatics, CCSD(T) dipole polarizabilities (see Section 1.3.2) are employed for all halide ions. The dispersion energy is represented as

$$V_{\text{disp}}^{2B}(\text{H}_2\text{O} - \text{X}^-) = - f_6(D_6^{\text{HX}} R_{\text{H}_1\text{X}}) C_6^{\text{HX}} \frac{1}{R_{\text{H}_1\text{X}}^6}$$
$$- f_6(D_6^{\text{HX}} R_{\text{H}_2\text{X}}) C_6^{\text{HX}} \frac{1}{R_{\text{H}_2\text{X}}^6} - f_6(D_6^{\text{OX}} R_{\text{OX}}) C_6^{\text{OX}} \frac{1}{R_{\text{OX}}^6} \tag{1.2}$$

where

$$f_n(\zeta) = 1 - \exp(-\zeta) \sum_{k=0}^{n} \frac{\zeta^k}{k!} \tag{1.3}$$

is the Tang-Toennies damping function.[67] The C_6^{HX} and C_6^{OX} dispersion coefficients were computed from "first-principles" using the exchange-hole dipole model (XDM) developed by Becke and Johnson.[68] The XDM calculations were carried out with the LC-ωPBE[69–71] functional using the Postg software.[72,73]

The classical electrostatic and dispersion contributions (V_{TTM}^{2B} and V_{disp}^{2B}, respectively), which are the dominant forces at long $\text{X}^- - \text{O}$ distances, are supplemented by a short-range term (V_{short}^{2B}) in order to effectively describe the quantum-mechanical effects, arising from the overlap of the individual halide ion and water electron densities (e.g., charge transfer, charge penetration, and Pauli repulsion), that become important as the molecules come closer to each other. V_{short}^{2B} is represented by permutationally invariant polynomials[74] that smoothly switch to zero as the distance between the halide ion and oxygen of the water molecule is greater than a predefined cutoff value

$$V_{\text{short}}^{2B}(\text{H}_2\text{O} - \text{X}^-) = s_2\left(\frac{R_{\text{OX}} - R_i}{R_o - R_i}\right) V_{\text{poly}} \tag{1.4}$$

with

$$s_2(x) = \begin{cases} 1 & \text{if } x < 0 \\ 1 + x^2(2x - 3) & \text{if } 0 \leq x < 1 \\ 0 & \text{if } 1 \leq x \end{cases} \tag{1.5}$$

11

The inner and outer cutoff radii (R_i and R_o) of the switching function s_2 are set to 5.0 Å and 6.0 Å for fluoride, 5.5 Å and 6.5 Å for chloride and bromide, and 6.0 Å and 7.0 Å for iodide. The cutoffs were chosen based on a systematic analysis of one-dimensional potential energy scans of the H_2O–X^- dimer, considering the O–X^- distance at which the difference between the reference 2B energy calculated at the CCSD(T)-F12b level and the energy obtained from the sum of V_{TTM}^{2B} and V_{disp}^{2B} is negligible. In Eq. 1.4, V_{poly} corresponds to the permutationally invariant polynomial that is a function of all pairwise distances involving both the physical atoms (H, O, and X^-) and the additional lone pair sites (L_1 and L_2) located on the oxygen atom of the MB-pol water molecule. All distances $d_{n=1-8}$ entering the expression of V_{poly} are listed in Table 1.1 along with the corresponding variables.

The variables associated with the distances $d_{n=1-8}$ can be divided into three categories: intramolecular variables (ξ_1, ξ_2, ξ_3), intermolecular Coulomb-type variables (ξ_4, ξ_5, ξ_6), and intermolecular variables with the lone pair (L) sites (ξ_7, ξ_8). V_{poly} is then constructed as a permutationally invariant polynomial in ξ_i. The invariance is imposed with respect to permutations of equivalent sites in the water molecule (H_1, H_2; L_1, L_2). A total of 874 symmetrized monomials form V_{poly}: 3 first-degree monomials formed from all intermolecular variables ($\xi_4, \xi_5, \xi_6, \xi_7, \xi_8$), 15 symmetrized second-degree monomials with at most a linear dependence on intramolecular variables, 49 symmetrized third-degree monomials, 119 symmetrized fourth-degree monomials, 243 symmetrized fifth-degree monomials, and 445 symmetrized sixth-degree monomials all with at most a quadratic dependence on the intramolecular variables. V_{poly} thus contains 874 linear fitting parameters (c_i), and 9 nonlinear fitting parameters, $D_6^{OX}, D_6^{HX}, \gamma_\parallel, \gamma_\perp, k_{HH_{intra}}, k_{OH_{intra}}, k_{XH_{coul}}, k_{XO_{coul}}, k_{XL}$.

1.2.2 Modifications to the potential

A few modifications[75] were made to the original MB-nrg halide-water 2B functional form,[37] as described in the previous section, for improved stability of the model across the entire $X^-(H_2O)$ dimer potential energy surfaces. The distance variables (ξ) composing the permutation-

Table 1.1. Distances and the corresponding variables entering the short range part of the potential, V_{poly}.

d_1	H1	H2	$\xi_1 = e^{-k_{\text{HH}_{\text{intra}}} d_1}$
d_2	O	H1	$\xi_2 = e^{-k_{\text{OH}_{\text{intra}}} d_2}$
d_3	O	H2	$\xi_3 = e^{-k_{\text{OH}_{\text{intra}}} d_3}$
d_4	X	H1	$\xi_4 = e^{-k_{\text{XH}_{\text{coul}}} d_4} / d_4$
d_5	X	H2	$\xi_5 = e^{-k_{\text{XH}_{\text{coul}}} d_5} / d_5$
d_6	X	O	$\xi_6 = e^{-k_{\text{XO}_{\text{coul}}} d_6} / d_6$
d_7	X	L1	$\xi_7 = e^{-k_{\text{XL}} d_7}$
d_8	X	L2	$\xi_8 = e^{-k_{\text{XL}} d_8}$

ally invariant polynomials, given in Table 1.1, of the form e^{-kd_i} and e^{-kd_i}/d_i, corresponding to the intra-molecular and inter-molecular internuclear distances, were replaced with $e^{-k(d_i - d_{0,i})}$ and $e^{-k(d_i - d_{0,i})}/d_i$, respectively. The $d_{0,i}$ variables were fit along with other non-linear parameters, to provide additional flexibility to the polynomials. All 445 symmetrized sixth-degree monomials were removed from the polynomials leaving only a total of 429 symmetrized monomials with highest degree five. The D_6^{OX} and D_6^{HX} parameters were fixed to their corresponding values in the TTM-nrg (originally introduced with i-TTM acronym) model,[76] for a consistent description of the long-range dispersion interactions. The overall accuracy and results of the potentials were only marginally changed by these modifications. All the analyses reported in this dissertation in the following chapters were performed with this modified version of the MB-nrg potentials.

1.3   Training sets and reference interaction energies

1.3.1   Halide-water two-body training sets

The original MB-nrg training sets as introduced in Ref. 37, were comprised of more than 12,000 distinct configurations for each $X^-(H_2O)$ dimer complex. Specifically, 12,773 configurations were used for $F^-(H_2O)$ with $F^- - O$ distances ranging between 1.8 and 7.5 Å, 17,256 configurations were used for $Cl^-(H_2O)$ with $Cl^- - O$ distances ranging between 2.1 and

8.0 Å, 17,738 configurations were used for $Br^-(H_2O)$ with Br^--O distances ranging between 2.2 and 7.9 Å, and 13,783 configurations were used for $I^-(H_2O)$ with I^--O distances ranging between 2.5 and 8.0 Å. The configurations used for each ion were obtained from (a) molecular dynamics (MD) simulations of dilute aqueous ionic solutions carried out at 298 K temperature and 1 atm pressure, (b) MD simulations of dilute aqueous ionic solutions carried out at 298 K temperature and 2000 atm pressure, (c) path integral molecular dynamics (PIMD) simulations of dilute aqueous ionic solutions carried at 298 K temperature and 1 atm pressure, (d) PIMD simulations of $X^-(H_2O)_4$ cluster carried out at 298 K temperature, (e) optimized structures of $X^-(H_2O)_n$ (n=1−8) clusters, (f) a polar grid constructed by rotating and translating each halide ion around the water molecule which was kept fixed in its vibrationally averaged geometry, and (g) scans along the vibrational normal modes of the $X^-(H_2O)$ dimers. The simulations mentioned in (a)−(e) were performed using the TTM-nrg potential energy functions.[76] Due to the high charge density and consequently high covalent character of F^-, at short distances fluoride ion can form very strong hydrogen bonds with water and significantly distort the geometry of the water molecule. To account for such distortions in the short-range, additional configurations obtained from one-dimensional relaxed scans on the $F^-(H_2O)$ dimer PES as well as from multi-dimensional grids were added to the $F^-(H_2O)$ two-body training set.

These training sets were later found to be incomplete in the high binding energy regions of the PES, which resulted in unphysical energies for configurations with small halide-water intermolecular distances. Such configurations (also called as *holes* on the PES) are not uncommon for potentials generated from high dimensional fits to electronic structure data and can appear if the training set is incomplete in certain regions of the configuration space.[77] Due to this, new training sets were generated for all four halide-water dimers from a full-dimensional polar grid, including intramolecular distortions of the water molecule. Starting from an initial set of about $2x10^6$, configurations were screened using a root mean squared deviation (RMSD) criterion of all internuclear distances to select dissimilar configurations. The threshold value for the the RMSD was varied as a function of the halide-oxygen distance and the two-body interaction

energy of the dimer calculated with the TTM-nrg potential energy functions, in order to obtain a weighted yet balanced representation of the PES with more configurations sampled around global minimum. Following the screening process, 15,643 configurations were obtained for $F^-(H_2O)$, 13,894 configurations for $Cl^-(H_2O)$, 11,608 configurations for $Br^-(H_2O)$ and 13,210 configurations for $I^-(H_2O)$.

1.3.2 Electronic structure calculations

In supervised machine learning techniques, the model is only as accurate as the data that is used to train that model. The quality of the input data is absolutely critical in determining the quality of the generated model. In the development of the MB-nrg potential energy functions it was ensured that the best possible reference data is used to fit the model. Since, the $X^-(H_2O)$ dimer complex is a relatively small system, the "gold-standard" correlated coupled cluster calculations can be performed with a reasonable computational cost. To decide the electronic structure method and basis sets for calculations of the two-body reference interaction energies, basis set convergence analysis for both CCSD(T) and CCSD(T)-F12b methods for the $Cl^-(H_2O)$ and $Br^-(H_2O)$ dimers was performed, as shown in Table 1.2. Based on the results, all two-body reference energies were calculated using the CCSD(T)-F12b[78,79] method in the complete basis set (CBS) limit, which was achieved via a two-point extrapolation[43,80] between the values obtained with the augmented correlation-consistent polarized valence triple-ζ (aug-cc-pVTZ) and quadruple-ζ (aug-cc-pVQZ) basis sets.[81–84] For the heavier halides, bromide and iodide, effective core potentials with 10 and 28 electrons were used, respectively.[85,86]

The gas-phase dipole polarizability of each halide ion was computed at the CCSD(T) level of theory using the even triply augmented quintuple zeta basis sets, t-aug-cc-pV5Z for F^- and Cl^-, and t-aug-cc-pV5Z-PP for Br^- and I^-. Triply augmented basis sets, which include additional diffuse functions were used specifically to account for the diffused nature of the electron density of halide anions which is particularly important in the calculation of electronic properties such as polarizability. The resulting polarizabilities are 2.4669, 5.3602, 7.1688, and

Table 1.2. CCSD(T) and CCSD(T)-F12b two-body interaction energies (in kcal/mol) for the $X^-(H_2O)$ ($X^- = Cl^-$, Br^-) dimers obtained using different basis sets, together with the BSSE (basis set superposition error) corrected energies.

Method/Basis set[a]	$Cl^-(H_2O)$		$Br^-(H_2O)$	
	V^{2B}	V^{2B}(BSSE corr)	V^{2B}	V^{2B}(BSSE corr)
CCSD(T)/AVTZ(-PP)	-15.8615	-15.0342	-13.7245	-12.9003
CCSD(T)/AVQZ(-PP)	-15.7331	-15.3648	-13.5305	-13.1945
CCSD(T)/AV5Z(-PP)	-15.7027	-15.4774	-13.4372	-13.2819
CCSD(T)/(Q5)(-PP)[b]	-15.6708	-15.5955	-13.3393	-13.3736
CCSD(T)-F12b/AVTZ(-PP)	-15.7623	-15.4336	-13.5357	-13.2385
CCSD(T)-F12b/AVQZ(-PP)	-15.6397	-15.5149	-13.3949	-13.3094
CCSD(T)-F12b/(TQ)(-PP)[c]	-15.5849	-15.5464	-13.3373	-13.3435
CCSD(T)-F12b/VTZ-F12(-PP)	-15.9214	-15.4709	-13.4658	-13.2211
CCSD(T)-F12b/VQZ-F12(-PP)	-15.7845	-15.5464	-13.3724	-13.3158

10.1184 Å^3, for F^-, Cl^-, Br^-, and I^-, respectively, which compare well with values previously reported in the literature.[87–89] All CCSD(T) and CCSD(T)-F12b calculations were performed with the quantum chemistry package Molpro, version 2015.1.[90]

1.3.3 Fitting procedure

Following the fitting protocol adopted for MB-pol,[57,58] the linear and nonlinear parameters of the MB-nrg potentials were optimized using singular value decomposition and the simplex algorithm, respectively, through the minimization of the regularized weighted sum of squared deviations calculated for the corresponding training set, S,

$$\chi^2 = \sum_{n \in S} w_n [V_{2B}^{model}(n) - V_{2B}^{ref}(n)]^2 + \Gamma^2 \sum_{l=1}^{874} c_i^2. \tag{1.6}$$

where, Γ is the regularization parameter, which is to used to avoid bias and ensure that no single parameter or group of parameters dominate the polynomials. After careful exploration, Γ was set to a value of 0.0005 in order to reduce the variation of the linear parameters without spoiling the overall accuracy of the fits. This commonly used regularization method is known as Tikhonov

regularization or ridge regression.[91]

In Eq. 1.6 the weights, w_n, were set to emphasize dimer configurations with lower total energy according to

$$w(E_i) = \left\{ \frac{\Delta E}{E_i - E_{\min} + \Delta E} \right\}^2, \tag{1.7}$$

where $E_{\min}$ is the lowest energy in the training set (i.e., dimer global minimum energy), and ΔE is a parameter used to favorably weight low-energy configurations. In this study, ΔE was chosen such that configurations with $E_i > 20$ kcal/mol have weights $w(E_i) \le 0.25$. Accordingly, $\Delta E = 50$ kcal/mol for $F^-(H_2O)$, 40 kcal/mol for $Cl^-(H_2O)$, and 30 kcal/mol for $Br^-(H_2O)$ and $I^-(H_2O)$. RMS errors of 0.2085 kcal/mol, 0.1273 kcal/mol, 0.0887 kcal/mol, and 0.0847 kcal/mol per dimer relative to the corresponding CCSD(T)-F12b reference data were obtained for $F^-(H_2O)$, $Cl^-(H_2O)$, $Br^-(H_2O)$, and $I^-(H_2O)$, respectively, for the entire training sets. RMS errors of 0.0686 kcal/mol, 0.0517 kcal/mol, 0.0377 kcal/mol and 0.0288 kcal/mol were obtained for $F^-(H_2O)$, $Cl^-(H_2O)$, $Br^-(H_2O)$, and $I^-(H_2O)$, respectively, for *low-energy* configurations with total energy, $E_i < 20$ kcal/mol. Mean unsigned errors of 0.1402 kcal/mol, 0.0857 kcal/mol, 0.0532 kcal/mol, and 0.0508 kcal/mol were obtained for $F^-(H_2O)$, $Cl^-(H_2O)$, $Br^-(H_2O)$, and $I^-(H_2O)$, respectively, for the entire training sets. Pearson's r was found to be 1.00 for all the four halide-water systems. The overall ability of the four MB-nrg $X^-(H_2O)$ ($X^- = F^-$, Cl^-, Br^-, I^-) PEFs to accurately reproduce the entire PES in the broad energy range is demonstrated in the correlation plots for the training sets with the corresponding CCSD(T)-F12b reference data shown in Figure 1.1.

1.4   Validation of the model

The minimum energy structures predicted by the MB-nrg PESs for the four $X^-(H_2O)$ dimers are depicted in Figure 1.2, while the corresponding binding energies are reported in Table 1.3. To assess the accuracy of the MB-nrg PESs, also listed in Table 1.3 are the binding energies that have been reported in the literature from calculations using correlated electronic
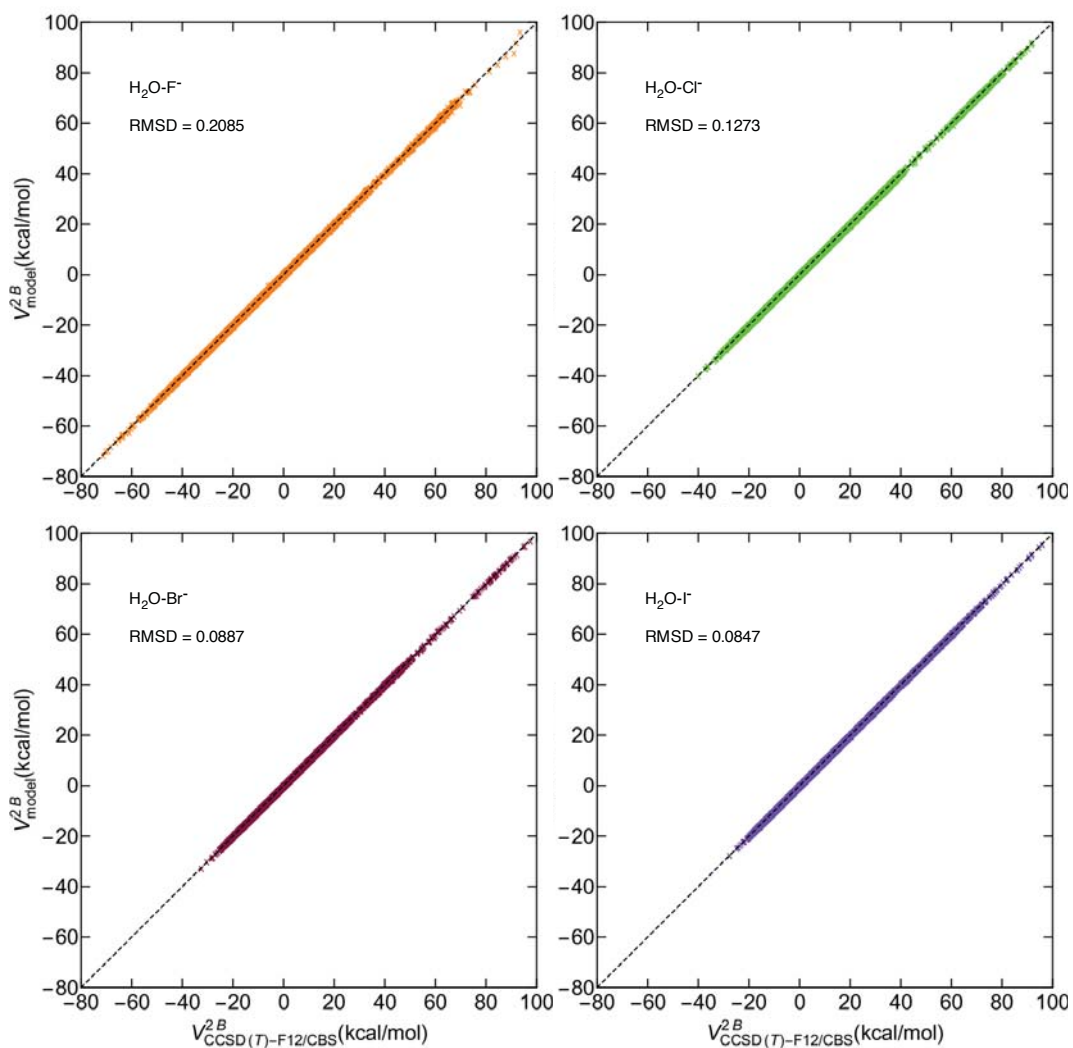
Figure 1.1. 2B energy correlation plots for the $X^-(H_2O)$ ($X^- = F^-$, Cl^-, Br^-, I^-) dimer training sets. Plotted on the *x*-axis are the CCSD(T)-F12b/CBS 2B energies, on the *y*-axis are the corresponding 2B energies calculated with the MB-nrg potentials.

18

structure methods, namely CCSD(T)-F12b, DF-MP2, and MP2,[76,92] recently developed analytical $F^-(H_2O)$ and $Cl^-(H_2O)$ PESs,[93] and both polarizable and point-charge force fields.[76,94] For all four $X^-(H_2O)$ dimers, the values predicted by the MB-nrg PESs are in quantitative agreement with the corresponding CCSD(T)-F12b/CBS results.
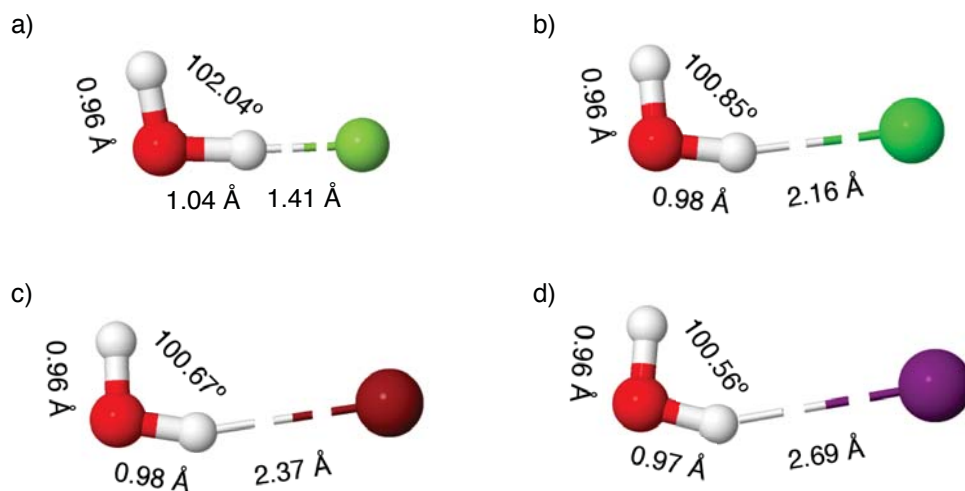
Figure 1.2. Minimum energy geometries for the $X^-(H_2O)$ dimers optimized with the MB-nrg potentials. a) $F^-(H_2O)$, b) $Cl^-(H_2O)$, c) $Br^-(H_2O)$, and d) $I^-(H_2O)$.

Table 1.3. Comparison between the binding energies (in kcal/mol) for $X^-(H_2O)$ dimers calculated using the MB-nrg potentials and the corresponding values reported in the literature obtained at the CCSD(T)-F12, DF-MP2, MP2 levels of theory as well as using analytical potential energy functions.

Method/Model	$F^-(H_2O)$	$Cl^-(H_2O)$	$Br^-(H_2O)$	$I^-(H_2O)$
$(eM)/(gBe-6)$[95]	26.99	15.38	13.38	11.38
Analytical PESs[93]	27.5	15.1	-	-
AMOEBA[94]	27.86	15.50	12.86	10.59
TTM-nrg[76]	27.91	14.62	12.64	10.65
MP2[92]	26.60	14.80	12.69	10.59
DF-MP2[76]	27.60	15.44	13.16	10.86
CCSD(T)-F12/CBS[76]	27.39	14.88	12.82	10.63
MB-nrg	27.25	14.74	12.76	10.60

To further assess the accuracy of the MB-nrg dimer PESs, one-dimensional radial scans

for different (θ, ϕ) orientations of X^- relative to H_2O (see Figure 1.3 for the definition of the reference coordinate system) are compared to the corresponding CCSD(T)-F12b/CBS results (Figure 1.4). Quantitative agreement between the MB-nrg and the CCSD(T)-F12b/CBS values is found for all four $X^-(H_2O)$ dimers at all distances and orientations. This demonstrates that the MB-nrg functional form is flexible enough to capture even the more complex short-range interactions where, due to the overlap of the X^- and H_2O electron densities, charge transfer through the hydrogen bond has to be accounted for. This is particularly evident in the case of the $F^-(H_2O)$ dimer, which exhibits a pronounced covalent character that cannot be correctly captured by classical force fields.[76]
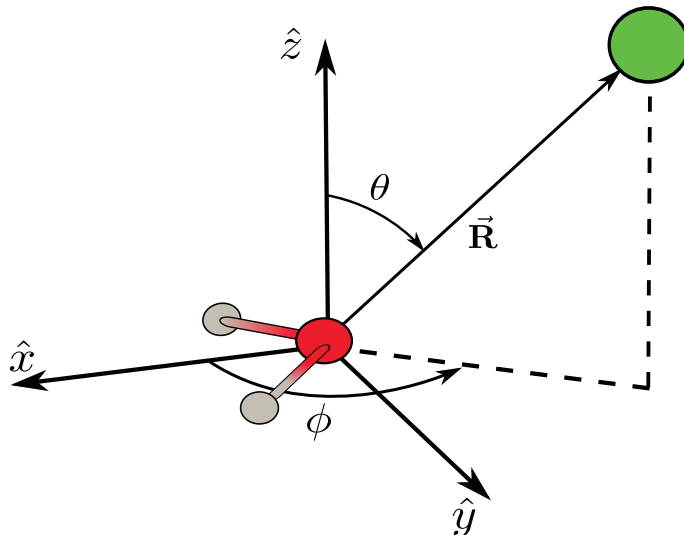
Figure 1.3. Reference coordinate system used in definition of the polar grids, radial scans, and potential energy angular profiles for the $X^-(H_2O)$ PESs. The water molecule, fixed in its vibrationally averaged geometry, lies in the $x-y$ plane with the x-axis along the HOH angle bisector.

Shown in the top panel of Figure 1.5 is the comparison between the potential energy angular profiles (PEAPs) along ϕ for planar configurations ($\theta = 90°$) calculated for each $X^-(H_2O)$ dimer at both CCSD(T)-F12/CBS and MB-nrg levels of theory. In these calculations the water molecule was kept fixed at its vibrationally averaged geometry and the $O–X^-$ distance was fixed to the minimum energy distance of each dimer for $\phi = 52.345°$ and $\theta = 90°$, corresponding
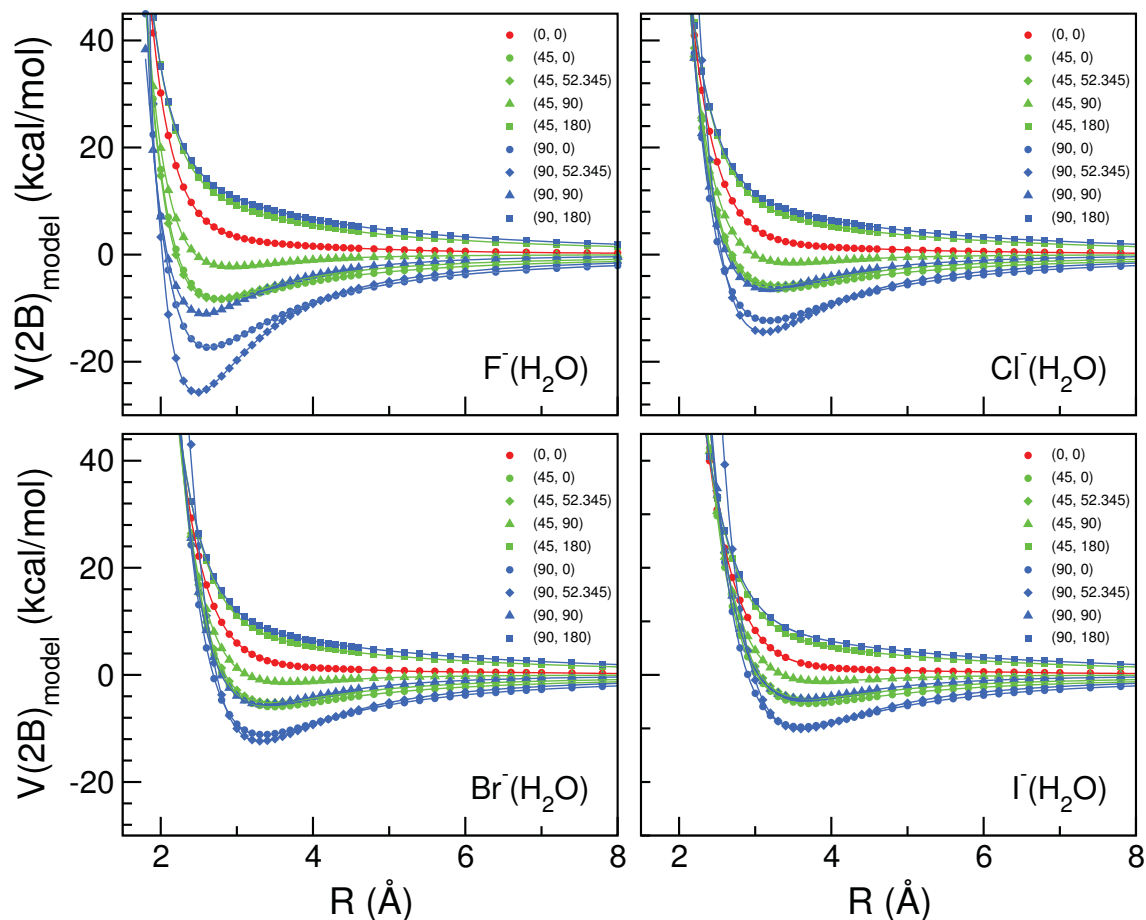
Figure 1.4. Radial scans of the $X^-(H_2O)$ ($X^- = F^-, Cl^-, Br^-, I^-$) dimer PESs. The symbols corresponds to the CCSD(T)-F12b/CBS values, while MB-nrg energies are shown with solid lines. The different orientations, θ, ϕ, of X^- relative to H_2O are given within the parentheses.

to 2.47 Å for H_2O-F^-, 3.09 Å for H_2O-Cl^-, 3.30 Å for H_2O-Br^-, and 3.59 Å for H_2O-I^-. The two minima in the PEAPs correspond to the two equivalent C_s minimum energy structures (see Figure 1.2) which are separated by a barrier with C_{2v} symmetry. Also shown in the bottom panel of Figure 1.5 are the PEAPs obtained with the TTM-nrg[76] and AMOEBA polarizable force fields.[94] For all H_2O-X^- dimers, the MB-nrg PESs accurately reproduce the CCSD(T)-F12b/CBS results at all orientations. In contrast, as already demonstrated in Ref. 76, the PEAPs calculated using conventional (polarizable) force fields exhibit significant deviations (as large as ~2 kcal/mol) from the reference data, which are particularly evident in the case of the H_2O-F^- dimer. These errors are attributed to charge penetration effects that are not accounted for in

common force fields. It has been shown that this problem can be alleviated to some extent by using damped valence electron distributions that mimic actual interacting electron clouds.[96]

This analysis thus reinforces the notion that classical potential energy functions (e.g., TTM-nrg and AMOEBA) are not capable of correctly describing short-range halide ion-water interactions, which, arising from the overlap of the monomer electron densities, are more quantum-mechanical in nature and display a non-negligible covalent character.
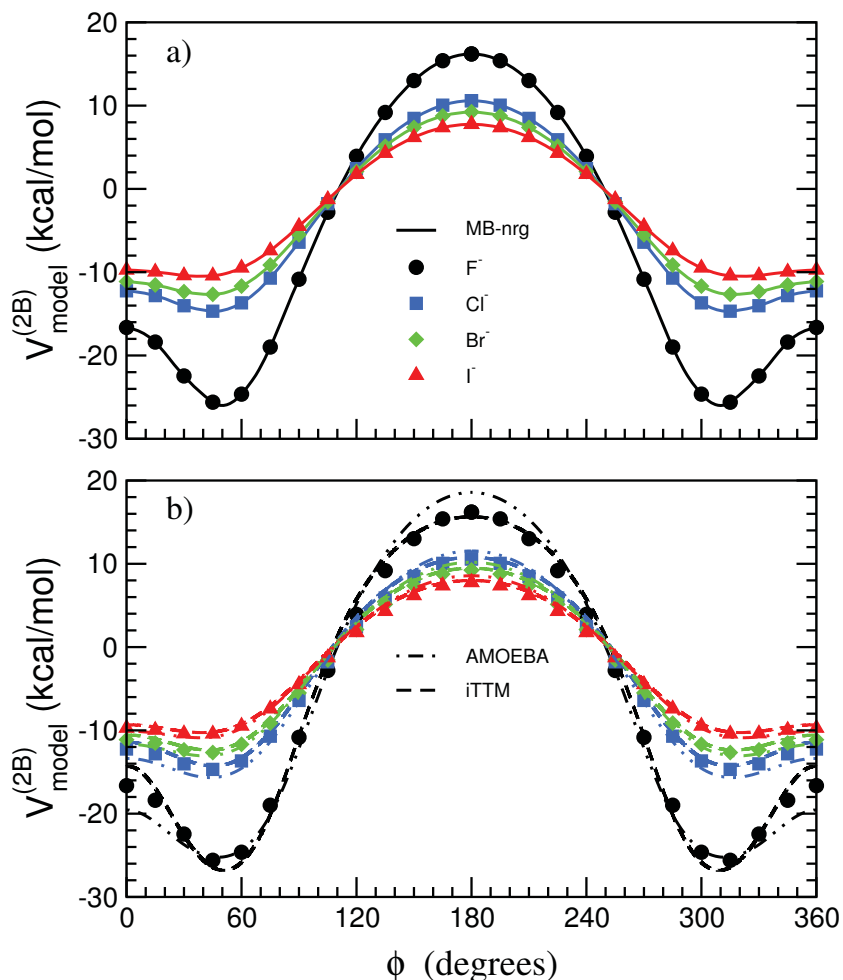
Figure 1.5. Potential energy angular profiles for the H_2O–X^- dimers. The MB-nrg energies are shown in a) as solid lines, and the corresponding TTM-nrg and AMOEBA values are shown in b) as dashed and dot-dashed lines, respectively. The symbols correspond to the CCSD(T)-F12b/CBS values.

1.4.1   Comparisons with DFT

In this section, the MB-nrg potentials for H_2O–X^- dimers are compared with various DFT models, with and without D3 dispersion corrections,[97] which are commonly employed in computer simulations to study the properties of ionic solutions. Specifically, this analysis includes results for the energetics and harmonic frequencies calculated with GGA functionals (BLYP[98,99], BLYP-D3, PBE[100], PBE-D3), meta-GGA functionals (TPSS[101], TPSS-D3), hybrid GGA functionals (PBE0[102], PBE0-D3, B3LYP[98,99,103], B3LYP-D3), and range-separated hybrid functionals (LC-ωPBE[69–71], LC-ωPBE-D3, ωB97X[104], ωB97XD[105]).
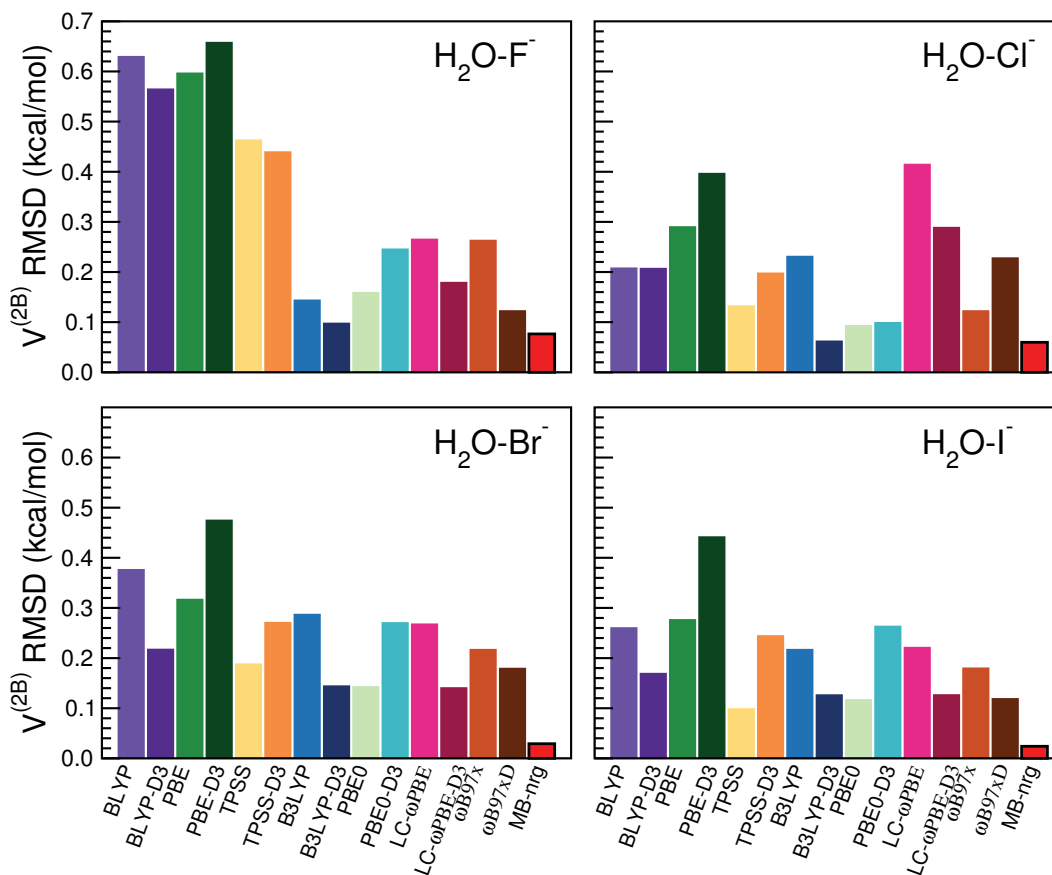
Figure 1.6. RMSDs associated with the 2B energies obtained from for various DFT models and the MB-nrg potentials for a set of $\sim$2000 dissimilar H_2O–X^- (X^- = F^-, Cl^-, Br^-, I^-) dimer configurations.

Figure 1.6 shows comparisons between the RMSDs associated with interaction energies

with respect to CCSD(T)-F12b/CBS values for a set of ~2000 dissimilar configurations for the four H_2O–X^- dimers with OX distance between 2.2 Å and 7.0 Å for fluoride, 2.2 Å and 8.0 Å for chloride, 2.9 Å and 7.8 Å for bromide, and 3.0 Å and 8.0 Å for iodide. The configurations were extracted from MD and PIMD simulations of aqueous ionic solutions carried out with the TTM-nrg potentials. The interaction energies for these configurations were in the range of -32 kcal/mol and +7 kcal/mol for H_2O–F^-, -15 kcal/mol and +25 kcal/mol for H_2O–Cl^-, -23 kcal/mol and +10 kcal/mol for H_2O–Br^-, and -14 kcal/mol and +12 kcal/mol for H_2O–I^-. This analysis directly reflects on the ability of the different models to accurately reproduce the global dimer PESs. Considerably large, halide-dependent errors are associated with all DFT models, both with and without D3 dispersion corrections. The halide-dependence is particularly worrisome, indicating that the accuracy of a specific DFT model is extremely sensitive to the different nature of the underlying intermolecular interactions for the different H_2O–X^- dimers. It is also important to note that adding the D3 dispersion correction does not necessarily lead to better agreement with the CCSD(T)-F12b/CBS data. GGA functionals display significant deviations, which can be as large as ~0.6 kcal/mol in the case of the H_2O–F^- dimer. Overall, the B3LYP functional with the D3 dispersion correction performs the best of all functionals analyzed in this study, with RMSDs of ~0.1 kcal/mol for the four H_2O–X^- dimers. Independently of the halide ion, the MB-nrg potentials are consistently in quantitative agreement with the CCSD(T)-F12b/CBS data, with RMSDs <0.02 kcal/mol.

Harmonic frequency calculations can provide insight into the overall shape of the H_2O–X^- PESs, directly reporting on the strength of the underlying intermolecular interactions. For example, the magnitude of the red shifts in the stretching frequencies of the OH bonds of the water molecules relative to the corresponding gas-phase values can be used as a measure of the relative hydrogen-bond strengths within the dimers. Figures 1.7 and 1.8 present comparisons between the deviations from CCSD(T)-F12b/aug-cc-pVQZ values for the hydrogen-bonded and free OH stretching frequencies of the water molecules in the H_2O–X^- dimers (see Figure 1.2 for representations of the dimer structures). In this analysis, the deviations of the MB-nrg harmonic

24
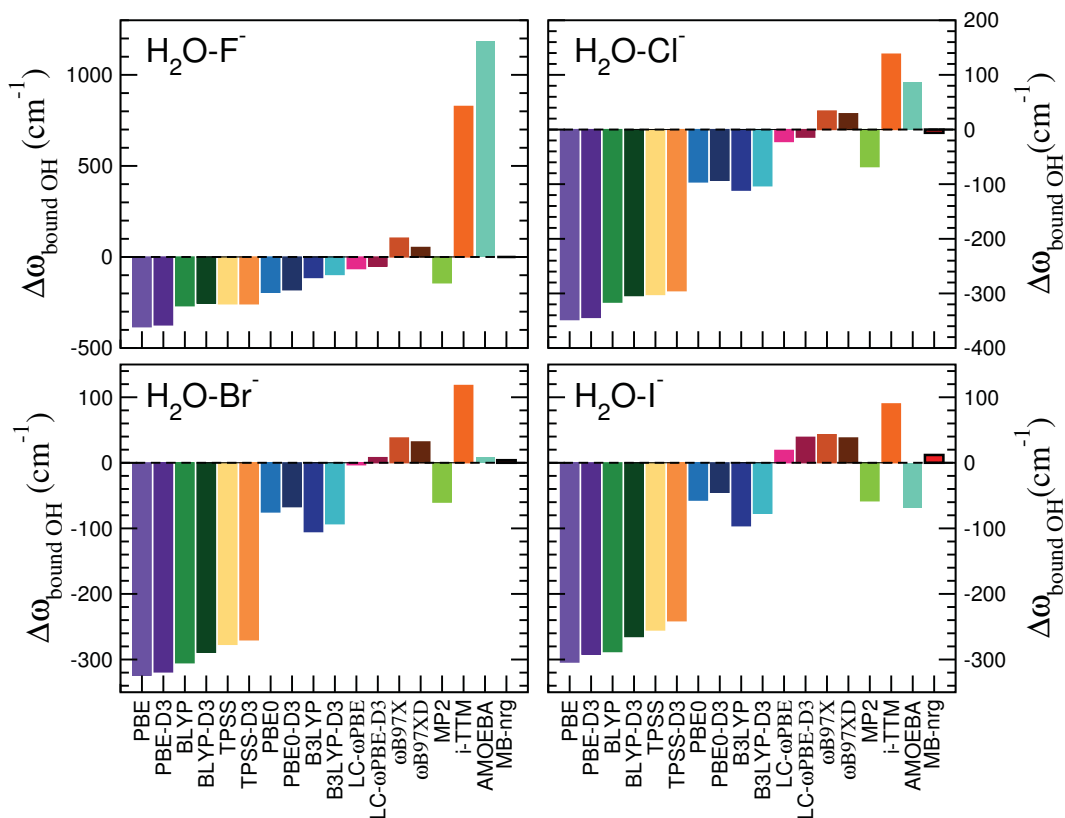
Figure 1.7. Deviations in the hydrogen-bonded OH stretching frequencies in the H_2O–X^- (X^- = F^-, Cl^-, Br^-, I^-) dimers relative to CCSD(T)-F12b reference values for the MB-nrg potentials, various DFT models, MP2 method, as well as the TTM-nrg and AMOEBA polarizable models.

frequencies relative to the reference data are compared with the corresponding values calculated with the same DFT models described above as well as at the MP2 level of theory, and with the TTM-nrg and AMOEBA polarizable models.

The errors in the interaction energies obtained with the different DFT models (Figure 1.6) are directly reflected in the harmonic frequencies. Except for the range-separated functionals, LC-ωPBE(-D3) and ωB97X(D), the hydrogen-bonded OH stretching frequencies predicted by all DFT models are significantly redshifted compared to the CCSD(T)-F12b values. In the case of GGA functionals, the deviations can be as large as a few hundred wavenumbers, indicating that these functionals predict the formation of hydrogen bonds that are too strong and thus provide a physically incorrect description of the local H_2O–X^- interactions. The DFT errors can be traced

25
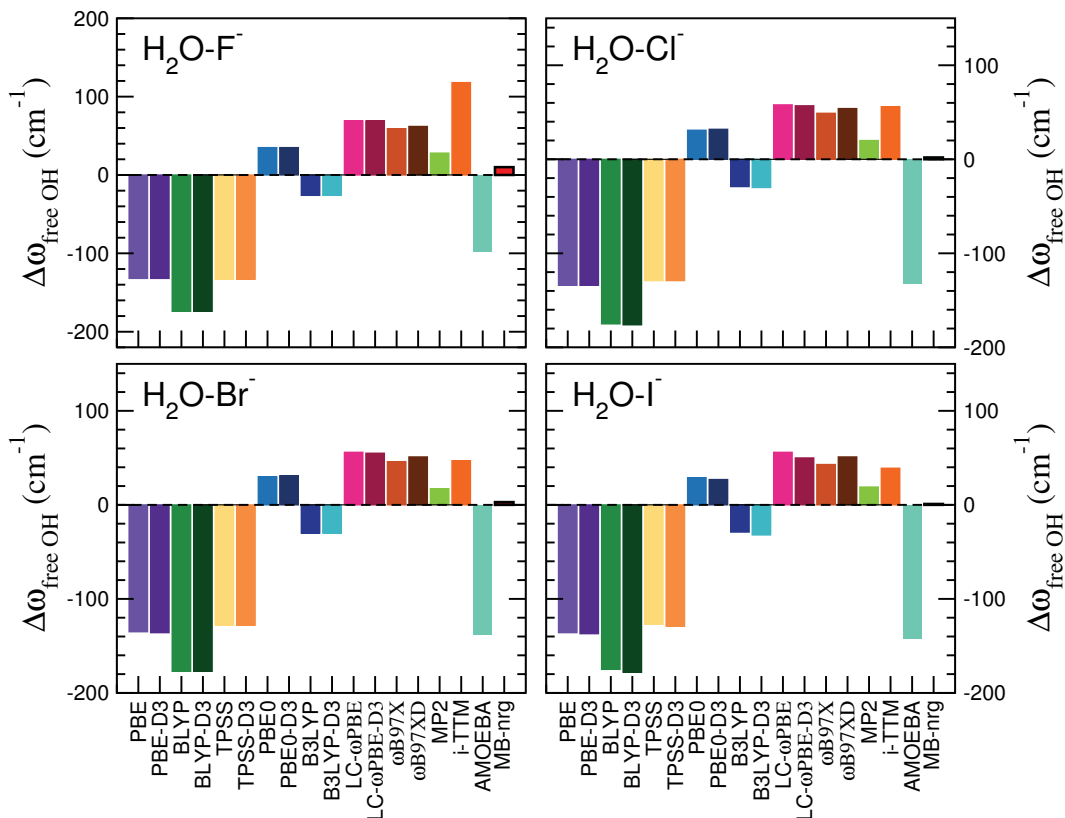
Figure 1.8. Deviations in the free OH stretching frequencies in the H_2O–X^- (X^- = F^-, Cl^-, Br^-, I^-) dimers relative to CCSD(T)-F12b reference values for the MB-nrg potentials, various DFT models, MP2 method, as well as with the TTM-nrg and AMOEBA polarizable models.

back to the self-interaction error, which is partially remedied by admixture of exact Hartree-Fock exchange, explaining the superior performance of hybrid and range-separated hybrid functionals as compared to GGA functionals. These deficiencies in the density functionals are well known and documented in the literature, including data on energies and vibrational frequencies of water and water clusters[106–110].

On the other hand, the stretching frequencies calculated with the polarizable TTM-nrg and AMOEBA models are in qualitative agreement with the reference values for the H_2O–Cl^-, H_2O–Br^-, and H_2O–I^- dimers. However, the deficiencies associated with the representation of the intermolecular interactions based on classical electrostatics clearly manifest themselves in the harmonic frequencies of the H_2O–F^- dimer. Being unable to correctly capture the covalent-

like nature of the H_2O–F^- interactions at short range, both TTM-nrg and AMOEBA models predict hydrogen-bonded OH stretching frequencies that are blueshifted from the CCSD(T)-F12b value by $\sim$800 cm^{-1} and $\sim$1200 cm^{-1}, respectively. The MB-nrg many-body potentials predict harmonic frequencies for both hydrogen-bonded and free OH stretches which are in excellent agreement with the reference values for all H_2O–X^- dimers, with deviations never exceeding 10 cm^{-1}. The level of accuracy achieved by the MB-nrg many-body potentials, which is comparable to that exhibited by the MB-pol water potential,[60] demonstrates that a physically correct description of both short- and long-range contributions is necessary for a consistently accurate representation of halide ion-water interactions.

This chapter, in part, is a reprint of the material as it appears in "Toward Chemical Accuracy in the Description of Ion-Water Interactions Through Many-Body Representations. 1. Halide-Water Dimer Potential Energy Surfaces", 2016. Bajaj, Pushp; Götz, Andreas W.; Paesani, Francesco; J. Chem. Theory Comput., 12, 2698, 2016. The dissertation author was the primary investigator and author of this paper.

Chapter 2

Vibrational spectra of halide-water dimer complexes

2.1   Introduction

Halide-water dimers have been the subject of much interest since they serve as proto-typical hydrogen-bonded complexes that exhibit large amplitude motion. In addition, since the potential energy surface (PES) of the halide-water dimers display two equivalent global minima with C_s symmetry separated by a C_{2v} saddle point along the in-plane water rocking motion, the intermolecular vibrational levels may split due to quantum tunneling.[77,111,112] This makes the theoretical assignment of the different absorption peaks observed in the experimental spectra particularly challenging, requiring both an accurate PES and a rigorous treatment of the nuclear motion at the quantum-mechanical level.

Due to its high proton affinity and, thus, relatively strong basic character, fluoride ion can establish strong hydrogen bonds with water, which are manifested in large redshifts of the OH stretching frequencies observed in the $F^-(H_2O)$ vibrational spectra. The strength of the halide-water hydrogen bonds then decreases from fluoride to iodide. This is accompanied by a reduction of the tunneling barrier on the underlying PES and consequent increase of the splitting of the vibrational levels. Previous investigations of the vibrational spectra of halide-water dimers include experimental measurements using cold traps and argon tagging techniques combined with harmonic and reduced-dimensionality anharmonic frequencies calculated on PESs obtained at the

MP2 level of theory.[111,113,114] Large shifts in the hydrogen-bonded OH stretching frequencies and increases in peak intensities were observed in the vibrational spectra of $F^-(H_2O)$, which can be attributed to the formation of strong hydrogen bonds and significant charge redistribution within the dimer.

Following the initial experimental measurements, six-dimensional calculations of the $Cl^-(H_2O)$ vibrational spectrum were carried out within the MULTIMODE framework using full-dimensional potential energy and dipole moment surfaces fitted to CCSD(T) electronic structure data.[115] More recently, anharmonic vibrational frequencies have been calculated for both $F^-(H_2O)$ and $F^-(D_2O)$ dimers using a variational method called GENIUSH and a semiglobal PES derived from CCSD(T)-F12a data.[112] The GENIUSH method employs the internal coordinates and direct product DVR (discrete variable representation) basis. The acronym GENIUSH stands for general (GE) rovibrational code with numerical (N), internal-coodinate (I), user-specified (US) Hamiltonians (H). Fully anharmonic vibrational frequencies, including couplings between all vibrational modes, have been reported for $Cl^-(H_2O)$[77]. This calculation was done, with the same PES used in Ref. 115, using a product basis with DVR functions (D) for the stretches and spherical harmonic type functions (S) for the bends and a symmetry adapted Lanczos eigensolver (L).[116,117] This method is referred to as DSL. The bend basis is appropriate for dealing with large amplitude bending motions. In all cases, good agreement was found between different theoretical predictions and the available experimental data.

In this study, we present a thorough analysis of the vibrational spectra of both $X^-(H_2O)$ and $X^-(D_2O)$ dimers, with X = F, Cl, Br, and I, obtained from DSL calculations using two sets of *ab initio* halide-water PEFs (TTM-nrg for Thole-type model energy[76] and MB-nrg for many-body energy[37]) recently reported in the literature. We note here that the TTM-nrg PEFs were originally introduced with the i-TTM acronym.[76] Since the TTM-nrg and MB-nrg PEFs only differ in the way many-body (MB) effects are represented, the analysis of the vibrational spectra presented here provides fundamental insights into the relative importance of short- and long-

range two-body (2B) interactions in determining the (inter)molecular dynamics. Furthermore, the direct comparison of the $X^-(H_2O)$ and $X^-(D_2O)$ spectra enables a quantitative assessment of the interplay between hydrogen-bond strength and nuclear quantum effects.

2.2 Computational methods

The vibrational frequencies of the $X^-(H_2O)$ and $X^-(D_2O)$ dimers were calculated using the method of Ref. 116 and 117, implemented in the RV4 code.[118] It uses coordinates derived from two Radau vectors and a Jacobi vector, a basis of products of potential-optimized discrete variable functions(PODVR)[119,120] for the stretch coordinates and a spherical harmonic type basis for the bend coordinates. Potential energy integrals are computed with Gauss quadrature. Eigenvalues and eigenvectros are determined with the symmetry-adapted Lanczos (SAL) algorithm.[121,122] Matrix-vector products are evaluated by doing sums sequentially.[123,124] In this study, we shall refer to the method as the DSL method. Since a thorough description of the DSL method is reported in Ref. 77, only the computational details specific to the present study are given here. All calculations in this study are for $J = 0$. Each basis function was

$$f_{\alpha_0}(r_0)f_{\alpha_1}(r_1)f_{\alpha_2}(r_2)u^{JMP}_{l_1 l_2 m_2 K}(\theta_1, \theta_2, \phi_2; \alpha, \beta, \gamma), \qquad (2.1)$$

where, $f_{\alpha_n}(r_n)$ are the PODVR functions for the three stretching coordinates, and $u^{JMP}_{l_1 l_2 m_2 K}$ is the parity adapted bend-rotation function. The latter was expressed as a linear superposition of two products of an associated Legendre function of θ_1, a spherical harmonic function of (θ_2, ϕ_2), and a Wigner function of the Euler angles (α, β, γ), with $P = 0$ and $P = 1$ corresponding to even and odd parity, respectively. The frame defining all coordinates and vectors used in the DSL calculations is shown in Figure **??**b). The basis set parameters, which were found to provide an optimal compromise between accuracy and computational cost, are listed in Table 2.1. This basis is called "basis I" in Ref. 77 and was shown to give levels up to 3000 cm^{-1} with errors less than 0.01 cm^{-1} for $Cl^-(H_2O)$. The PODVR basis functions are defined by a cut reference
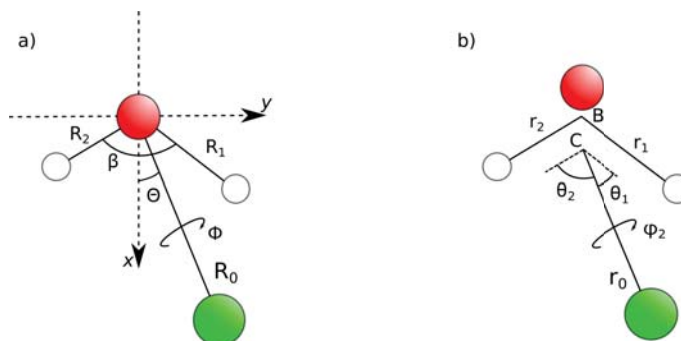
Figure 2.1. a) Internal coordinate system for the halide-water dimers. x-axis is placed along the H-O-H angle, β, bisector. b) Polyspherical coordinate system for the halide-water dimers based on Radau-Jacobi orthogonal vectors.

Table 2.1. The number of PODVR basis functions for each stretching coordinate given by N_{r_0}, N_{r_1}, and N_{r_2}. Maximum values of l and m indices of the spherical harmonic basis, l_x and m_x. The numbers of θ and ϕ quadrature points, N_θ and N_ϕ. The number of even-parity basis functions, N_{bas}.

Parameter	Value
N_{r_0}	24
$N_{r_1} = N_{r_2}$	7
$l_x = m_x$	25
N_θ	27
N_ϕ	54
N_{bas}	7.29×10^6

potential with other coordinates fixed at their values at the C_{2v} saddle point. These coordinate values can be found in the Supporting Information. Using the C_{2v} saddle point rather than the C_s equilibrium ensures that the stretch basis functions have symmetry when permuting the two H atoms of H_2O.

For comparison, the intramolecular vibrational frequencies of the water molecule within the $X^-(H_2O)$ and $X^-(D_2O)$ dimers were also calculated by combining the local-mode[125,126] and local-monomer[127] (LM) methods as described in Ref. 128. Within this LM scheme, the Hessian matrix at the optimized geometry of each dimer was calculated from finite-differentiation of

analytic first derivatives of both TTM-nrg and MB-nrg PEFs. Local modes[125,126,129] were then generated using a distance-based (Boys) localization criterion and frequency window of 500 cm^{-1} for both X$^-$(H$_2$O) and X$^-$(D$_2$O). The 3 highest-frequency (harmonic pseudo-frequency) modes, corresponding to "left" and "right" single O-H (O-D) stretches and H-O-H (D-O-D) bends, were identified and used to integrate the potential energy using Gauss-Hermite quadrature on a grid of 9 points in each dimension. The local-monomer[130,131] Hamiltonian was finally diagonalized to yield anharmonic frequencies and eigenvectors. Although this Hamiltonian was diagonalized in a reduced three-dimensional space for the water monomer, the potential energy was evaluated for the whole dimer, thereby including environmental effects. The expansion coefficients of the anharmonic wavefunction, in the harmonic basis, were used to assign bend overtones.

As mentioned above, two different PEFs (TTM-nrg[76] and MB-nrg[37]) were used to represent the underlying PESs of X$^-$(H$_2$O) and X$^-$(D$_2$O) dimers with X = F, Cl, Br, and I. In both PEFs, the intramolecular water distortion and the intermolecular water-water interactions are described by the many-body MB-pol PEF,[57–59] which has been shown to predict the properties of water from the gas to the condensed phase with high accuracy.[60–65] Both PEFs describe long-range ion-water interactions through permanent and induced electrostatics, within the Thole-type framework,[132,133] and two-body dispersion energy. TTM-nrg and MB-nrg, however, differ in the way short-range interactions are represented. In TTM-nrg, the short-range interactions are modeled using Born-Mayer type functions of all interatomic distances.[76] As discussed in Ref. 76, the Born-Mayer parameters were optimized by fitting each X$^-$(H$_2$O) TTM-nrg PEF to *ab initio* interaction energies calculated at the CCSD(T)-F12 level of theory in the complete basis set (CBS) limit for ~500 dimer configurations. The MB-nrg PEFs, on the other hand, use permutationally invariant polynomials in transformed variables of all interatomic distances to accurately represent quantum-mechanical short-range effects (e.g., charge penetration, charge transfer, and Pauli repulsion) that become increasingly important when the electron densities of individual monomers (i.e., X$^-$ and H$_2$O) overlap. The permutationally invariant polynomial of

each MB-nrg PEF was originally trained on the interaction energies calculated at the CCSD(T)-F12/CBS level of theory on $\sim$12,000 dissimilar $X^-(H_2O)$ dimer configurations representative of the corresponding PES.[37] The MB-nrg potentials were shown to accurately describe the corresponding halide-water dimer PESs and predict harmonic vibrational frequencies in close agreement with the corresponding CCSD(T)-F12/CBS reference data.[37] Refined versions of the original permutationally invariant polynomials as described in Section 1.2.2, in which both functional form and CCSD(T)-F12/CBS training sets were modified to improve the overall accuracy and stability of the MB-nrg PEFs, are used in this study.

It should be noted that no artificial constraints are applied, within the integration bounds of the internal coordinates, to either the TTM-nrg or the MB-nrg PEFs to obtain converged results in the present DSL calculations. As discussed in Refs. 76 and 37, both PEFs are derived from extensive training sets that effectively explore repulsive regions of the underlying PES and adopt functional forms where the combination of many-body classical electrostatics and short-range corrections provides a physically correct behavior at all internuclear separations. These two factors ensure that both PEFs are well behaved over a wide range of dimer configurations, including highly distorted (i.e., high potential energy) geometries. *Ad hoc* adjustments are commonly used to prevent the appearance of unphysical features on the calculated PESs (e.g., potential energy holes where the energy of a distorted molecular configuration is lower than the energy corresponding to the equilibrium geometry). Holes corresponding to configurations with short intermolecular distances and repulsive orientations were found on $X^-(H_2O)$ PESs previously reported in the literature.[77,115] Problematic regions were also found on the recent $F^-(H_2O)$ PES, which were attributed to the opening of dissociation channels.[112] Consequently, in the GENIUSH calculations of Ref. 112, the ranges of the coordinates for DVR functions were restricted to effectively avoid these problematic regions. The presence of holes on the PESs is particularly problematic when the Schrödinger equation is solved using a quadrature grid that spans the entire configuration space, as is the case in this study. No such holes appear on either the TTM-nrg or MB-nrg PEFs, used here.
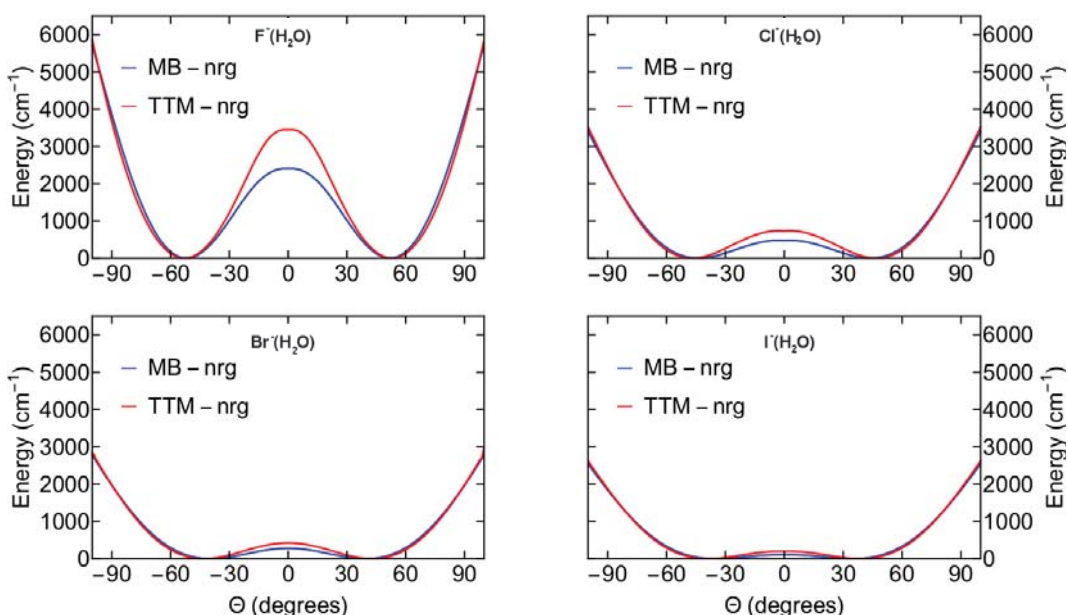
Figure 2.2. Minimum energy path along the tunneling coordinate Θ, for the four halide-water dimers.

2.3 Halide-water dimer potential energy landscape

Due to the C_{2v} symmetry of the water molecule, the PES of each $X^-(H_2O)$ dimer displays two equivalent global minima with C_s symmetry which are separated by a C_{2v} transition state along the in-plane water rocking motion coordinate. Both location and height of the barrier on each PES depend on the strength of the corresponding hydrogen bond established by each halide ion and the water molecule. The minimum energy angular path along Θ as defined in Figure **??**a), is obtained by doing a constrained optimization of all other coordinates keeping the Θ value fixed. It is shown in Figure 2.2 for all four halide-water PESs.

The barrier height systematically decreases from $F^-(H_2O)$ to $I^-(H_2O)$, reflecting the corresponding change in the nature of the underlying interactions, with F^- exhibiting stronger and more covalent-like interactions with the water molecule due to its more pronounced basic character. As the ion size and associated polarizability increase the interactions within the $X^-(H_2O)$ dimers become increasingly more electrostatic in nature. These changes in the

underlying interactions are quantitatively predicted by the MB-nrg PEFs, which, as shown in Ref. 37, accurately reproduces CCSD(T)-F12/CBS data for all dimer configurations. In contrast, as already discussed in previous studies,[37,76] the TTM-nrg PEFs, as well as all other models that rely on a purely classical description of the intermolecular interactions, are not capable of correctly describing short-range interactions arising from the overlap of the monomer electron densities. These intrinsic deficiencies of the TTM-nrg PEFs are particularly evident in the comparisons with the corresponding MB-nrg results shown in Figure 2.2. For all four $X^-(H_2O)$ dimers, the TTM-nrg PEFs always predict higher barriers, with the differences relative to the MB-nrg profiles becoming smaller as the classical electrostatic component of the interactions become larger (i.e., as both ion size and polarizability increase). The internal coordinates defining the positions of the global minimum (C_s configuration) and saddle point (C_{2v} configuration) on the PESs described by both TTM-nrg and MB-nrg PEFs, along with the corresponding potential energy values, are listed in Table 2.2 for all four $X^-(H_2O)$ dimers. The corresponding polyspherical coordinates based on the Radau-Jacobi orthogonal vectors are given in the Supporting Information.

To provide direct comparisons between the relative strength and anisotropy of the different halide-water interactions, two-dimensional contour plots of the four dimer PESs are shown in Figure 2.3 as a function of the water OH stretching coordinate R_1 (on the x-axis) and the OX stretching coordinate R_0 (on the y-axis), with all other coordinates defined in Figure **??**a) being kept fixed at the values corresponding to the minimum energy configurations (see Table 2.2). As expected, the overall shape of the four PESs changes significantly depending on the nature of the interactions, with the minimum energy region moving to larger halide-water separations and systematically elongating along R_0 as the ion size increases. The more covalent-like nature of the $F^-(H_2O)$ dimer becomes apparent in the relatively stronger attraction along R_1 for $R_0 \sim 4.5$ bohr. Although both TTM-nrg and MB-nrg PEFs correctly predict the overall shape of all four $X^-(H_2O)$ PESs, noticeable differences between the two sets of PEFs exist, which become progressively smaller from $F^-(H_2O)$ to $I^-(H_2O)$. In particular, the relatively larger differences between the TTM-nrg and MB-nrg PESs found for $F^-(H_2O)$ reinforce the notion that purely

Table 2.2. Internal coordinates for the C_s minimum energy structure and the C_{2v} saddle point structure of the $X^-(H_2O)$ dimers as predicted by the TTM-nrg and MB-nrg PESs. All structures are planar with $\Phi=180°$. Distances (R_i) in bohr, angles (Θ and β) in degrees, and potential energy (V) in cm^{-1}.

	Coordinate	global minimum (C_s)		saddle point (C_{2v})	
		TTM-nrg	MB-nrg	TTM-nrg	MB-nrg
$F^-(H_2O)$	R_0	4.728	4.642	4.793	4.857
	R_1	1.914	1.970	1.829	1.834
	R_2	1.789	1.808	1.829	1.834
	Θ	51.54	48.91	0.00	0.00
	β	105.74	102.01	90.33	90.78
	V	0.00	0.00	3451.08	2404.40
$Cl^-(H_2O)$	R_0	5.857	5.901	5.980	5.905
	R_1	1.849	1.855	1.819	1.823
	R_2	1.800	1.810	1.819	1.823
	Θ	44.46	40.55	0.00	0.00
	β	102.89	100.76	96.97	96.07
	V	0.00	0.00	732.83	474.64
$Br^-(H_2O)$	R_0	6.277	6.272	6.318	6.248
	R_1	1.839	1.846	1.818	1.822
	R_2	1.802	1.811	1.818	1.822
	Θ	41.13	37.37	0.00	0.00
	β	102.39	100.62	97.94	97.20
	V	0.00	0.00	422.805	277.31
$I^-(H_2O)$	R_0	6.832	6.795	6.803	6.742
	R_1	1.831	1.835	1.816	1.820
	R_2	1.804	1.811	1.816	1.820
	Θ	36.28	31.92	0.00	0.00
	β	101.96	100.61	99.00	98.48
	V	0.00	0.00	192.58	101.63

classical PEFs, like TTM-nrg, are unable to describe quantitatively short-range interactions where quantum-mechanical effects associated with the overlap of the monomer electron densities (e.g., charge penetration and transfer, and Pauli repulsion) become increasingly important.

Further insights into the energy landscape associated with the halide-water dimers are obtained from the analysis of the two-dimensional contour plots of the four PESs shown in Figure 2.4 as a function of the angle Θ (on the x-axis) and OX stretching coordinate R_0 (on
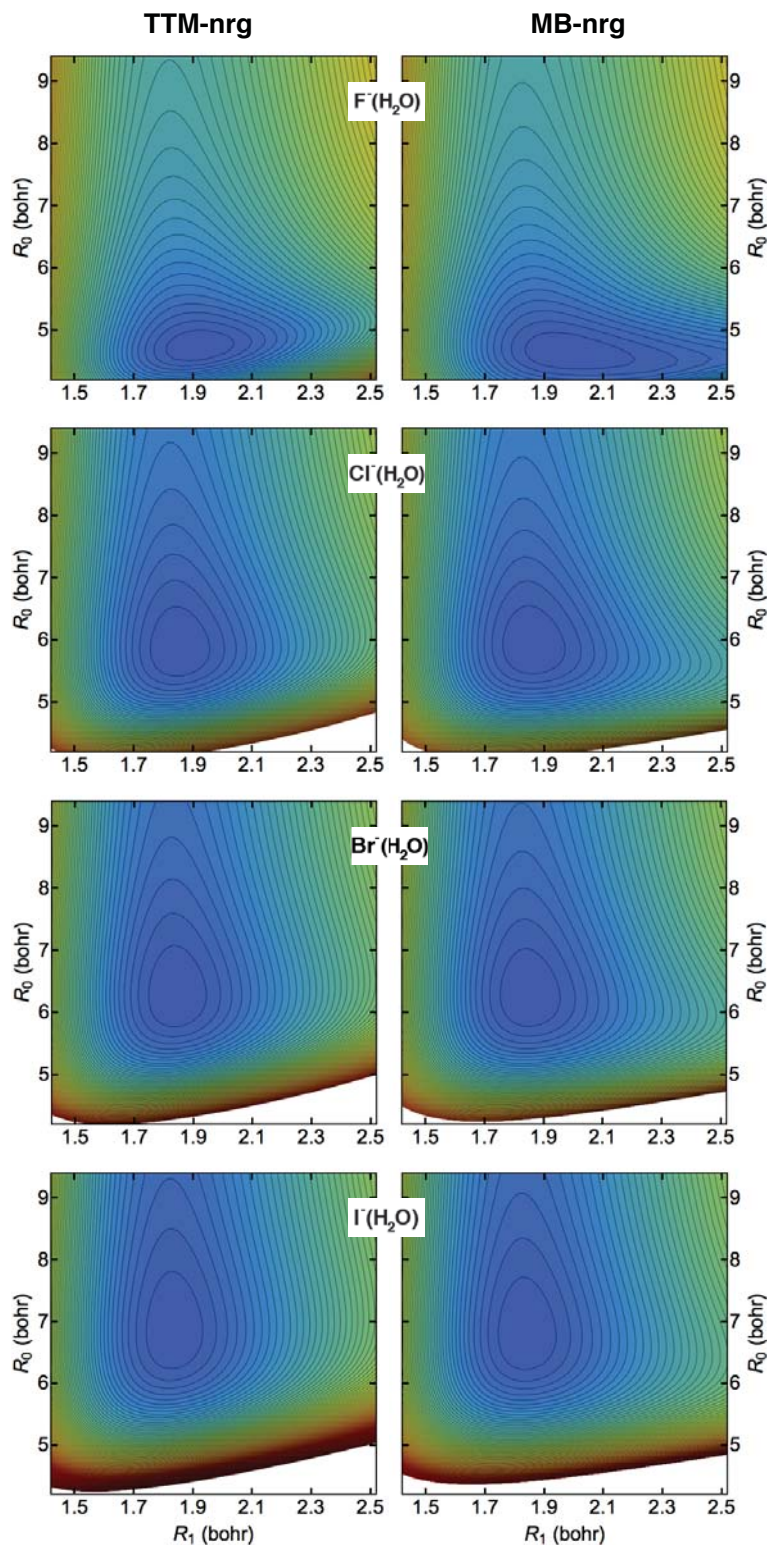
Figure 2.3. Two dimensional cuts of the TTM-nrg and MB-nrg PESs, for the four halide-water dimers, along two stretching coordinates R_1 and R_0. The energy spacing between the adjacent lines is 500 cm^{-1}.

the y-axis), with all other internal coordinates (Figure **??**a)) fixed at the values corresponding to the minimum energy configurations (Table 2.2). All four contour plots display two minima corresponding to the two hydrogen-bonded configurations of the dimer. It is important to note that, since each contour plot is calculated keeping the internal coordinates R_1, R_2, and β (Figure **??**a)) of the water molecule fixed at the values of the corresponding minimum-energy dimer configuration, the two energy minima are not symmetric by construction. Figure 2.4 clearly shows that, going from $F^-(H_2O)$ to $I^-(H_2O)$, the two energy minima move to smaller Θ and become shallower.

2.4   Anharmonic vibrational frequencies and tunneling splittings

Selected vibrational levels of the $X^-(H_2O)$ and $X^-(D_2O)$ dimers, calculated with the DSL method using both TTM-nrg and MB-nrg PEFs are listed in Tables 2.3 - 2.6. Along with the intramolecular water vibrational modes calculated with the LM method, as described previously. In the DSL calculations the vibrational states were identified by analyzing both probability densities and wavefunction amplitudes as functions of the coordinates of interest. Plots of the probability densities along θ_1 and θ_2 (Figure **??**b)) obtained with MB-nrg for the fundamental and the first overtone of the HOH bending vibration, the first overtone of the out-of-plane bending vibration, and the fundamental of the free OH stretching vibration of the $I^-(H_2O)$ dimer are provided in the Supplementary Material as examples. It should be noted that, due to inter-mode couplings, some states, marked with asterisks in the tables cannot be unambiguously identified. Also included in the tables, as a reference, are the available experimental data.[111,113,114]

The DSL results with MB-nrg are in close agreement with the corresponding experimental values for all dimers, except for $F^-(H_2O)$ for which the somewhat larger differences can be attributed to the covalent-like character of the fluoride-water interaction and the fact that, by construction, the MB-nrg PEF do not include the $HF+OH^-$ dissociation channel for the
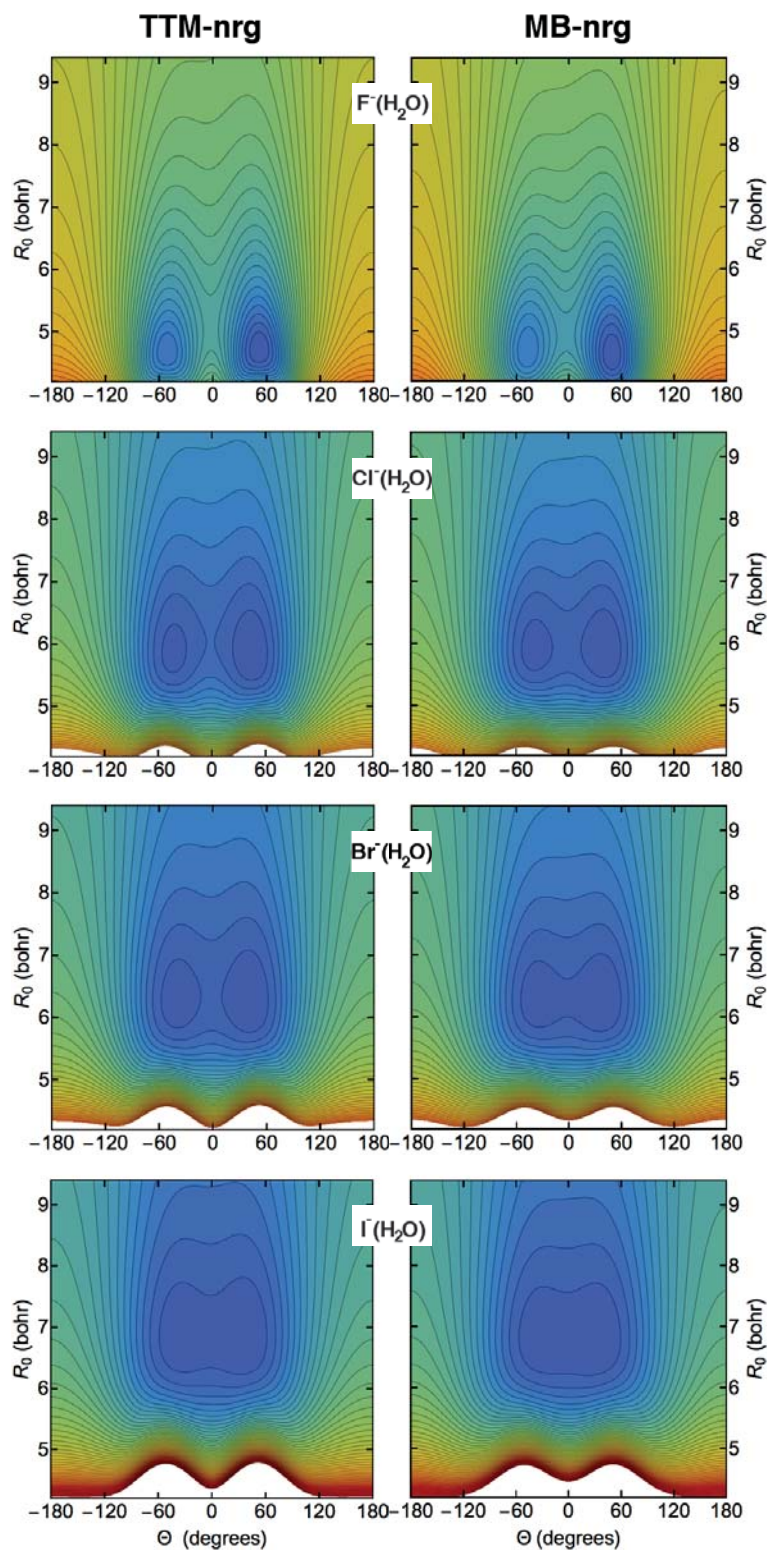
Figure 2.4. Two dimensional cuts of the TTM-nrg and MB-nrg PESs, for the four halide-water dimers, along the tunneling coordinate, Θ and stretching coordinate, R_0. The energy spacing between the adjacent lines is 500 cm^{-1}.

dimer. The failure of the TTM-nrg PEFs to correctly describe short-range quantum-mechanical interactions manifest itself in vibrational frequencies that are noticeably blueshifted compared to the corresponding values obtained with the MB-nrg PEFs for the high frequency stretching modes. The low frequency modes are, however, well-represented by the TTM-nrg PEFs. These modes are relatively less affected by the presence of the ion as compared to the stretching modes. Importantly, the agreement with experimental values for the TTM-nrg PEFs improves from $F^-(H_2O)$ to $I^-(H_2O)$, reflecting the increase in classical-like nature of the interactions as the ion charge density decreases. This reinforces the notion that classical polarizable PEFs, being unable to accurately represent the intermolecular energy landscape, are not suited for quantitative studies of vibrational spectra, as previously suggested in Refs. 76 and 37. For all dimers, the LM results are in good agreement with the corresponding DSL results, except for $F^-(H_2O)$ and $F^-(D_2O)$ described by the MB-nrg PEF. These shortcomings can be explained by considering the complexity of the underlying PES as well as strong inter-mode couplings which make the LM approximations less accurate.

The three fundamental vibrational transitions (bend, symmetric and asymmetric stretches) of an isolated water molecule, as predicted by the Partridge-Schwenke water monomer PES,[134] are 1594.78 cm^{-1}, 3657.04 cm^{-1} and 3755.96 cm^{-1} for H_2O and, 1178.23 cm^{-1}, 2671.33 cm^{-1} and 2787.59 cm^{-1} for D_2O.[134] From the analysis of the vibrational frequencies of each halide-water dimer, it is evident that the vibrational dynamics of the water molecule is significantly affected by the presence of the halide anion. In the binary complexes, it is clearly not always valid to label strech vibrations as symmetric and asymmetric stretches, because both OH stretches become more localized. The hydrogen-bonded OH stretch is significantly redshifted, up to $\sim$1200 cm^{-1} in $F^-(H_2O)$ due to the strong proton affinity of the fluoride anion, while the water free OH stretch vibrates at a much higher frequency, closer to that of the isolated water molecule. As expected, going from $F^-(H_2O)$ to $I^-(H_2O)$, the redshift of the hydrogen-bonded OH stretch decreases due to the weakening of the underlying intermolecular interactions. On the other hand, the water bend in the ion-water dimers is slightly blueshifted ($\sim$50 cm^{-1} for the $X^-(H_2O)$ dimers

Table 2.3. Selected vibrational levels of $F^-(H_2O)$ (first row) and $F^-(D_2O)$ (second row) obtained from DSL calculations with both TTM-nrg and MB-nrg PEFs. All values are in cm^{-1}. The two tunneling-split partners are given in the symmetric (ST) and anti-symmetric (AT) columns.

Mode	TTM-nrg			MB-nrg			Experiment
	ST	AT	LM	ST	AT	LM	
ZPE	5385.36	0.00		5176.75	0.00		
	3973.60	0.00		3695.05	0.00		
ν_{FO}	435.74	435.74		377.91	377.92		
	399.82	399.82		368.58	368.58		
ν_{ip}	577.09	577.09		556.74	556.75		
	453.82	453.82		411.95	411.95		
ν_{oop}	1021.91	1021.91		1119.17	1119.17		
	733.88	733.88		815.84	815.84		
$2\nu_{oop}$	2429.97	2429.97		2163.85	2164.03		
	1462.44	1462.44		1582.14	1582.15		
ν_{HOH}	1670.44	1670.44	1649.32	1748.34*	1748.36*	1675.96	1650
ν_{DOD}	1219.58	1219.58	1209.19	1258.01	1258.01	1394.58	
$2\nu_{HOH}$	3324.62	3324.77	3298.56			3321.87	
$2\nu_{DOD}$	2433.98	2433.99	2416.06	2535.16	2535.14	2740.40	
$\nu_{boundOH}$	3081.50	3081.47	3132.73	1435.86*	1435.86*	2109.81	1523
$\nu_{boundOD}$	2227.10	2227.10	2249.10	1076.44*	1076.44*	1576.15	
ν_{freeOH}	3804.10	3804.10	3809.53	3729.84*	3730.42*	3782.53	3687
ν_{freeOD}	2804.47	2804.47	2807.16	2839.46	2839.47	2963.79	

and ~ 40 cm^{-1} for the $X^-(D_2O)$ dimers) relative to the isolated water molecule since the bending motion becomes strained due to hydrogen bonding to the anion. For all vibrational states, the tunneling splitting increases going from $F^-(H_2O)$ to $I^-(H_2O)$, which can be explained by the lowering of the energy barrier between the two equivalent global minima along the tunneling coordinate Θ (Figure **??**a)).

The DSL vibrational frequencies calculated with the TTM-nrg and MB-nrg PEFs are, in general, smaller than those obtained within both harmonic and one-dimensional anharmonic approximations for $X^-(H_2O)$ dimers and their isotopologues (with X = Cl, Br, and I).[111] These

Table 2.4. Selected vibrational levels of $Cl^-(H_2O)$ (first row) and $Cl^-(D_2O)$ (second row) obtained from DSL calculations with both TTM-nrg and MB-nrg PEFs. All values are in cm^{-1}. The two tunneling-split partners are given in the symmetric (ST) and anti-symmetric (AT) columns.

Mode	TTM-nrg			MB-nrg			Experiment
	ST	AT	LM	ST	AT	LM	
ZPE	5152.60	0.23		5065.90	1.04		
	3784.50	0.01		3702.17	0.06		
ν_{ClO}	179.37	179.69		185.64	186.86		
	174.62	174.63		178.77	178.88		
ν_{ip}	335.52	344.78		287.13	316.60		309
	253.39	253.77		223.77	226.80		227
ν_{oop}	703.00	702.41		714.86	712.43		738
	511.61	511.60		519.05	518.92		
$2\nu_{oop}$	1367.51	1368.87		1380.08	1385.05		1404
	1005.50	1005.56		1015.68	1015.98		1028
ν_{HOH}	1656.44	1656.96	1639.26	1674.70	1674.88	1624.49	1653
ν_{DOD}	1217.60	1217.63	1208.20	1216.68	1216.88	1201.00	1219
$2\nu_{HOH}$	3274.24	3274.33	3237.45	3315.02	3316.78	3227.44	3289
$2\nu_{DOD}$	2411.94	2412.04	2392.03	2442.25	2442.35	2393.42	2429
$\nu_{boundOH}$	3414.45	3414.70	3385.90		3146.49*	3100.86	3146
$\nu_{boundOD}$	2503.72	2503.76	2487.66	2376.14	2376.16	2314.38	2341
ν_{freeOH}	3754.30	3754.01	3757.96	3705.73*	3703.66*	3698.84	3697
ν_{freeOD}	2766.47	2766.48	2770.96	2757.75	2757.79	2727.51	2737

differences, which are likely due to intrinsic limitations of the methods employed in Ref. 111, are particularly large for the more anharmonic modes involving the halide anions, such as the in-plane wag and hydrogen-bonded OH stretches.

As mentioned in the Section 2.1, among the halide-water dimers, $Cl^-(H_2O)$ has been extensively studied using different theoretical approaches. The vibrational spectrum of $Cl^-(H_2O)$ was obtained from both full-dimensional MULTIMODE[115] and DSL[77] calculations using a PES derived from high-level *ab initio* calculations.[115] Good agreement is found between the results

Table 2.5. Selected vibrational levels of $Br^-(H_2O)$ (first row) and $Br^-(D_2O)$ (second row) obtained from DSL calculations with both TTM-nrg and MB-nrg PEFs. All values are in cm^{-1}. The two tunneling-split partners are given in the symmetric (ST) and anti-symmetric (AT) columns.

Mode	TTM-nrg			MB-nrg			Experiment
	ST	AT	LM	ST	AT	LM	
ZPE	5097.33	2.30		5022.77	5.63		
	3741.17	0.15		3673.85	0.71		
ν_{BrO}	138.06	140.75		146.67	153.19		
	133.18	133.18		138.64	140.41		
ν_{ip}	241.54	274.88		209.21	281.71		
	198.79	205.62		171.93	191.29		
ν_{oop}	629.62	625.01		648.15	637.98		664
	457.91	457.63		468.35	467.13		
$2\nu_{oop}$	1339.63	1349.78		1237.78	1255.52		1262
	1023.21	1023.92		915.97	918.07		
ν_{HOH}	1654.97	1656.57	1635.92	1666.76	1671.13	1619.04	1647
ν_{DOD}	1216.95	1217.05	1207.06	1212.99	1213.62	1197.06	1216
$2\nu_{HOH}$	3275.90	3277.02	3237.36	3316.99	3319.25	3197.13	3238
$2\nu_{DOD}$	2414.42	2414.49	2394.87	2407.20	2407.53	2370.85	2429
$\nu_{boundOH}$	3490.31	3490.79	3467.34	3303.80*	3297.91*	3268.14	3296
$\nu_{boundOH}$	2559.59	2559.63	2548.22	2474.93	2475.03	2429.17	2451
ν_{freeOH}		3743.06	3746.27	3697.55*	3693.17*	3698.40	3695
ν_{freeOH}	2763.49	2763.43	2763.94	2764.93	2765.17	2728.10	2726

of Refs. 77 and 115 and the present DSL values obtained using both TTM-nrg and MB-nrg PEFs, with the frequencies reported here being consistently smaller for all vibrational modes. Considering that the present calculations were carried out with the same DSL method used in Ref. 77, these differences can be attributed to differences in the two PEFs used to represent the underlying $Cl^-(H_2O)$ PES. Variational rovibrational energy levels of $F^-(H_2O)$ and $F^-(D_2O)$ dimers, along with the associated tunneling splittings, have also recently been calculated using a newly developed semiglobal PES.[112] While close agreement is found between the vibrational

Table 2.6. Selected vibrational levels of $I^-(H_2O)$ (first row) and $I^-(D_2O)$ (second row) obtained from DSL calculations with both TTM-nrg and MB-nrg PEFs. All values are in cm^{-1}. The two tunneling-split partners are given in the symmetric (ST) and anti-symmetric (AT) columns.

Mode	TTM-nrg			MB-nrg			Experiment
	ST	AT	LM	ST	AT	LM	
ZPE	5032.21	16.37		4965.06	27.05		
	3696.71	3.25		3636.87	8.93		
ν_{IO}	110.39	128.89		117.30	147.65		
	103.92	110.19		97.62	121.72		
ν_{ip}	166.17	237.89		163.74	264.09		
	127.53	169.92		122.00	171.83		
ν_{oop}	571.48	547.43		591.24	554.28		
	408.89	404.22		428.61	416.78		
$2\nu_{oop}$	1065.37	1100.02		1078.75	1128.13		1098
	891.66	900.64		800.72	816.35		
ν_{HOH}	1655.23	1667.77	1633.08	1657.81	1679.94	1614.00	1639
ν_{DOD}	1217.15	1219.53	1206.08	1208.39	1215.94	1193.91	1208
$2\nu_{HOH}$	3278.71	3287.33	3233.18	3305.16	3319.76	3197.13	3246
$2\nu_{DOD}$	2416.42	2418.02	2394.45	2404.39	2409.82	2370.85	2401
$\nu_{boundOH}$	3563.51	3566.31	3538.18	3395.84*	3422.35*	3398.83	3393/3422
$\nu_{boundOD}$	2608.46	2609.41	2598.71	2550.55	2547.63	2515.35	2511/2527
ν_{freeOH}	3729.03	3730.23	3733.75	3696.56*	3702.08	3693.44	3692/3706
ν_{freeOD}	2751.61	2756.55	2757.17	2747.70	2740.96	2725.73	2728

frequencies reported in Ref. 112 and those obtained here with the MB-nrg PEF, the TTM-nrg values are significantly different, particularly for the stretching modes, due to already mentioned inaccuracies associated with the TTM-nrg description of short-range interactions within the fluoride-water dimer. To the best of our knowledge, no calculations of the vibrational spectra of $X^-(H_2O)$ and $X^-(D_2O)$ dimers with X = Br and I have been reported in the literature.

This chapter, in full, is a reprint of the material as it appears in "Vibrational Spectra of Halide-Water Dimers: Insights on Ion Hydration from Full-Dimensional Quantum calculations on many-body potential energy surfaces", 2018. Bajaj, Pushp; Wang, Xiao-Gang.; Carrington Jr.,

Tucker; Paesani, Francesco; J. Chem. Phys., 148, 102321, 2018. The dissertation author was the primary investigator and author of this paper.

Chapter 3

Hydrogen bond rearrangement through tunneling in the iodide-water trimer complex

3.1 Introduction

Determining the driving forces that govern ion hydration is critical to the molecular-level understanding of a broad range of chemical transformations occurring in aqueous solutions.[3,4,6,135–147] Because of long-range Coulomb interactions, ions do not exist as isolated species under equilibrium in the gas phase but form neutral ionic aggregates (e.g., ionic salts). Completely different behavior is observed when ions are dissolved in aqueous solutions. In this case, ion-ion interactions are mediated by the presence of water molecules that allow ions to exist as individual solvated species, up to saturation. Ion stabilization in aqueous solutions results from the interplay between ion-water interactions, which primarily depend on the nature of the ion, and entropic contributions, which are associated with solvent reorganization around the charged species. Although the water hydrogen-bond (H-bond) network is expected to adapt to the presence of ions, the extent to which its structural, thermodynamic, and dynamical properties change, remains an open question.[148]

Halide ions represent a prototypical group of ionic systems, which exhibits a relatively large variation in size, charge density, and polarizability. General correlations have been derived

between the ion's chemical nature and properties of the surrounding H-bond network, with smaller fluoride ions, on one hand, establishing stronger H-bonds with water, and larger and more polarizable iodide ions, on the other hand, inducing relatively larger structural rearrangements on the surrounding H-bond network, at least locally. Ultrafast vibrational spectroscopy experiments indicate that the dynamics of water in the first solvation shells of halide ions is significantly slowed down compared to that observed in pure water.[149] Ion specific effects have been found at the air/water interface suggesting that larger and more polarizable halide ions as iodide may exhibit relatively higher propensity for the interface than smaller halides and cations.[6,150]

Given recent advances in high-resolution vibrational spectroscopy which has been accompanied by continued progress in the development of accurate quantum dynamics methods, small halide-water clusters represent ideal systems for characterizing the interplay between ion-water and water-water interactions, energetic and entropic contributions, and nuclear quantum effects in H-bond rearrangements around individual halide ions.[75,77,92,112,115,151–162] Measurements of vibrational predissociation spectra combined with successive isotopic substitutions have allowed for precisely probing possible H-bonding arrangements and monitoring their evolution as a function of temperature.[1,163] In particular, vibrational spectra of the iodide-dihydrate complex, $I^-(H_2O)_2$,[1,163] measured at low temperature in the water OH bond stretching region exhibit a well-defined pattern consisting of four distinct peaks at 3344 cm^{-1}, 3516 cm^{-1}, 3619 cm^{-1}, and 3684 cm^{-1}, corresponding to specific H-bonding environments. As the temperature increases above 50 K, a new, broad peak starts emerging at 3440 cm^{-1} which is accompanied by the simultaneous disappearance of the initial pattern observed at low temperature, indicating that the complex undergoes significant temperature-dependent H-bond rearrangements.

In this study, state-of-the-art quantum simulations combined with many-body representations of the underlying intermolecular interactions, were used to provide a molecular-level interpretation of the temperature-dependent H-bond dynamics in $I^-(H_2O)_2$ observed experimentally in Refs. 163 and 1. Our analysis provides unambiguous evidence for H-bond rearrangements via tunneling mediated by the presence of the iodide ion. Selective isotopic substitutions, demon-

strate that tunneling is still observed, although to a lesser extent, in $I^-(D_2O)_2$, while it is largely suppressed in the asymmetric $I^-(HOD)(D_2O)$ isotopologue, in which the hydrogen atom remains locked-in in the free position at low temperature. As the water-water H-bond starts breaking at temperatures above $\sim$75 K, the complex transitions from a closed to an open configuration, which becomes the most stable structure of the complex above 150 K.

3.2   Computational methods

Recently developed many-body PEFs, MB-nrg,[37,75] were used to describe the iodide-water intermolecular interactions. Within the MB-nrg framework, the long-range ion-water interactions are described through permanent and induced electrostatics as per the Thole-type model,[132,133] and two-body dispersion interactions. The more complex and quantum mechanical short range two-body interactions, are represented by permutationally invariant polynomials (PIPs) comprised of transformed variables of all internuclear distances. The PIPs are derived from fits to interaction energies calculated at the CCSD(T)-F12/CBS level of theory, which is the current "gold-standard" in electronic structure calculations, for more than 12,000 dissimilar configurations of $X^-(H_2O)$ dimers, where $X^- = F^-$, Cl^-, Br^- and I^-. The intramolecular water distortions and the intermolecular water-water interactions are given by the many-body MB-pol PEF,[57–59] which has been shown to predict the properties of water from the gas to the condensed phase with unprecedented accuracy.[63–65] The accuracy of MB-nrg PEFs has been demonstrated through comparisons of harmonic and anharmonic vibrational spectra calculations, with CCSD(T)-F12/CBS reference data and experimentally obtained values, respectively, for all four halide-water dimers.[37,75]

To take into account nuclear quantum effects, path-integral[164] molecular dynamics (PIMD)[165] simulations were performed, where all atoms were treated as distinguishable particles. Path-integral methods take advantage of the isomorphism between the quantum partition function and the partition function corresponding to a classical ring polymer made of M interacting "beads"

connected by harmonic springs. In the limit $M \rightarrow \infty$, the fully quantum equilibrium properties are recovered. For finite values of M, the approximate partition function is expressed as follows, for one degree of freedom (q):

$$Q_M = \int dq_1...dq_M \exp[-\mathcal{K}_M/\beta - \beta \mathcal{U}_M] \qquad (3.1)$$

with

$$\mathcal{K}_M = \frac{mM}{2\hbar^2} \sum_{1 \leq n \leq M} (q_n - q_{n+1})^2, \mathcal{U}_M = \frac{1}{M} \sum_{1 \leq n \leq M} V(q_n) \qquad (3.2)$$

where $\mathcal{K}_M$ and $\mathcal{U}_M$ are the quantum kinetic and potential energies, respectively, m is the mass, and $q_{M+1} = q_1$. In order to study the temperature dependent evolution of the dynamics in the iodide-water dihydrate complex, the simulations were carried out at increasing temperatures ranging from 10 K to 200 K with decreasing number of beads. $M = 1024$ beads were used for 10 K, 512 beads were used for 30 K, 256 beads were used for 50 K and 75 K, and for 100 K and higher temperatures 128 beads were used. The number of beads at different temperatures were chosen based on the convergence of the total quantum PIMD energy.

The ring polymer instanton (RPI) method was used to identify the tunneling pathways and corresponding tunneling splitting patterns for the $I^-(H_2O)_2$ and $I^-(D_2O)_2$ complexes. Since the method is described in detail with relevant derivations elsewhere,[166] only a brief description is provided here. Similar to the theory behind the PIMD technique described above, this method is based on a discretized representation of Feynman's path-integral formulation of quantum mechanics. The instanton paths are obtained by minimizing the action of a ring-polymer consisting of beads linked together by harmonic springs, on the inverted potential energy surface, using the L-BFGS algorithm. The tunneling splitting is then approximated from the Boltzmann operator by fluctuations around the instanton paths connecting the equivalent minima. The RPI method has been used to calculate tunneling splittings for small water clusters, previously, with high accuracy.[2,167] A linear polymer of 2048 beads with $\beta\hbar = 60$, was found to provide

converged results for the tunneling splitting values for both $I^-(H_2O)_2$ and $I^-(D_2O)_2$.

The quantum free energies for the two H-bond bifurcation motions in the $I^-(HOD)(D_2O)$ complex at 10 K and 50 K were computed from biased PIMD simulations using the well-tempered metadynamics method for enhanced sampling.[168,169] In standard metadynamics, the system is evolved under a biased history-dependent potential that is constructed as the sum of gaussian functions deposited along the trajectory on predefined variables of interest, called collective variables (CVs), s_i.

$$V(\vec{s},t) = \sum_{k\tau < t} W(k\tau)exp\left(-\sum_{i=1}^{d} \frac{(s_i - s_i(q(k\tau)))^2}{2\sigma_i^2}\right) \tag{3.3}$$

where, τ is the gaussian deposition stride, σ_i is the width and $W(k\tau)$ is the height of the Gaussian for the ith CV. The added gaussian potentials discourage the system from revisiting the same configuration in the collective variable space and eventually force the system to explore new areas on the free energy surface (FES). In the long time limit, the sum of gaussian terms will almost exactly compensate the underlying FES and provide an estimate of the free energy along the chosen CV(s).[168]

$$V(\vec{s}, t \to \infty) = -F(\vec{s}) + C \tag{3.4}$$

In the well-tempered technique, which has been shown to be more efficient and accurate in providing free energy estimates,[169] the height of the gaussian is decreased with simulation time, as given below,

$$W(k\tau) = W_0 exp\left(-\frac{V(\vec{s}(q(k\tau)), k\tau)}{k_B \Delta T}\right) \tag{3.5}$$

where, W_0 is the initial gaussian height, k_B is the Boltzmann constant and ΔT is an input parameter that can be tuned to regulate the extent of free-energy exploration. The bias potential smoothly converges in the long time limit, but it does not fully compensate the underlying free energy:

$$V(\vec{s}, t \to \infty) = -\frac{\Delta T}{T + \Delta T} F(\vec{s}) + C \tag{3.6}$$

The CVs thus sample an ensemble at at temperature $T + \Delta T$ which is higher than the system temperature T. In the limit $\Delta T = 0$, the expression takes the form of standard molecular dynamics and at $\Delta T \rightarrow \infty$ it corresponds to ordinary metadynamics. In this study, the implementation of well-tempered metadynamics within the PLUMED plugin[170] was used to bias the PIMD simulations. As described in the main text, the H-O-I angle and H-O-I-O' dihedral in the $I^-(HOD)(D_2O)$ complex, were chosen as the CVs. The gaussian potentials were added on the values of the CVs corresponding to the centroid of the ring-polymer in the PIMD simulations. The parameter used to alter ΔT, called the "biasfactor", given as the ratio between the temperature of the CVs $(T + \Delta T)$ and the system temperature (T):

$$\gamma = \frac{T + \Delta T}{T} \tag{3.7}$$

was set to a value of 6.

3.3 Tunneling pathways and ground-state H-bond rearrangements

As shown in Figure 3.1, the minimum energy configuration of the iodide-dihydrate complex corresponds to a cyclic structure with a double-donor (DD) water molecule donating single H-bonds to both the iodide ion and the second water molecule, which, on the other hand, acts as a single-donor / single-acceptor (DA), donating one H-bond to the iodide ion and having one free OH bond. Since the four OH bonds in $I^-(H_2O)_2$ experience different H-bonding environments, they are characterized by distinct stretching frequencies spanning a range of $\sim$400 cm^{-1} as shown in Figure 3.1. For both $I^-(H_2O)_2$ and $I^-(D_2O)_2$, the anharmonic frequencies calculated by combining the local-mode[125,126] and local-monomer[127] methods with the iodide-water MB-nrg many-body potential energy function (PEF) of Ref. 37 are always within 25 cm^{-1} of the corresponding experimental values, which provides support for the accuracy of the overall theoretical approach employed in this study.[128]

Mode	I⁻(H₂O)₂		I⁻(D₂O)₂	
	Theory	Experiment	Theory	Experiment
IHB$_{AD}$/IDB$_{AD}$	3337	3344	2475	2480
IHB$_{DD}$/IDB$_{DD}$	3500	3504/3516	2578	2589
IH/ID	3594	3619	2663	2684
F$_{OH}$/F$_{OD}$	3684	3684	2719	2719
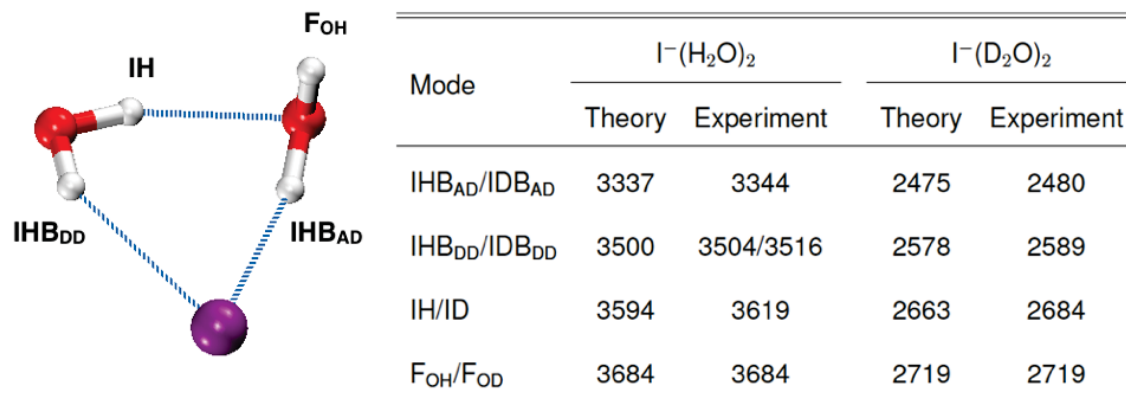
Figure 3.1. (*Left*) Global minimum energy configuration of the iodide dihydrate complex. (*Right*) Theoretical and experimental[1] OH/OD stretching frequencies (in cm^{-1}) in I⁻(H₂O)₂ and I⁻(D₂O)₂, respectively. See text for details.
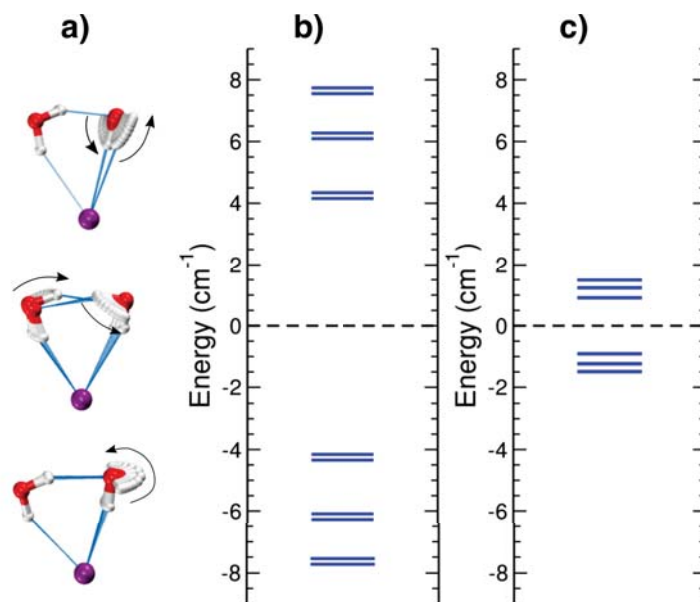
Figure 3.2. a) The three major tunneling pathways in the I⁻(H₂O)₂ and I⁻(D₂O)₂ clusters. b) Ground state tunneling splitting pattern of the I⁻(H₂O)₂ cluster due to the three tunneling pathways. c) Same as in b) but for the I⁻(D₂O)₂ isotopologue (doublets not resolved).

52

It has been established that tunneling pathways leading to H-bond rearrangements, and tunneling splittings of otherwise degenerate energy levels, exist in halide-water dimers[75,77,112] as well as in the water trimer, which, in its minimum energy configuration, exhibits a cyclic structure analogous to that of the iodide dihydrate complex.[2,171–173] To determine possible ground-state (0 K) tunneling pathways, and associated tunneling splittings, in $I^-(H_2O)_2$ and its isotopologue, $I^-(D_2O)_2$, quantum ring-polymer instanton (RPI) calculations[2,174] are carried out with the iodide-water MB-nrg PEF of Ref. 37. Three major tunneling pathways, namely, iodide-water H-bond bifurcation, water-water H-bond bifurcation, and flip rotation (see Figure 3.2a), are identified. The first two pathways involve the breaking and forming of a H-bond, while the third pathway corresponds to the out-of-plane rotation of the free OH bond of the DA water molecule. The associated energy splitting patterns calculated by diagonalizing the corresponding tunneling matrices[2] are shown in Figure 3.2b and 3.2c. Within the RPI formalism, the dimensions of the tunneling matrices represent the number of identical versions of each molecular complex, which are generated through permutations of the hydrogen and deuterium atoms, respectively, with each matrix element corresponding to the tunneling splitting associated with a distinct pathway connecting two different versions of the same complex.[2] As expected, given the heavier mass of deuterium and, consequently, lower vibrational zero-point energy associated with the OD bonds, the RPI calculations predict smaller tunneling splittings for $I^-(D_2O)_2$ than $I^-(H_2O)_2$.

Although the RPI results provide unambiguous evidence for the existence of tunneling pathways, determining the associated timescales is critical to guiding future comparisons with experimental vibrational spectra, which may become available as progress in the development of high-resolution techniques continues. To this purpose, the tunneling dynamics within the different isotopologues of the iodide dihydrate complex, $I^-(H_2O)_2$, $I^-(D_2O)_2$, and $I^-(HOD)(D_2O)$, is determined by monitoring the time evolution of the corresponding H-bond arrangements through propagation of the time-dependent Schrödinger equation under the action of the tunneling matrix. Figures 3.3a and 3.3b show, respectively, the probabilities for a hydrogen atom of $I^-(H_2O)_2$ and a deuterium atom of $I^-(D_2O)_2$, initially located in the free position ($t = 0$, blue trace), to
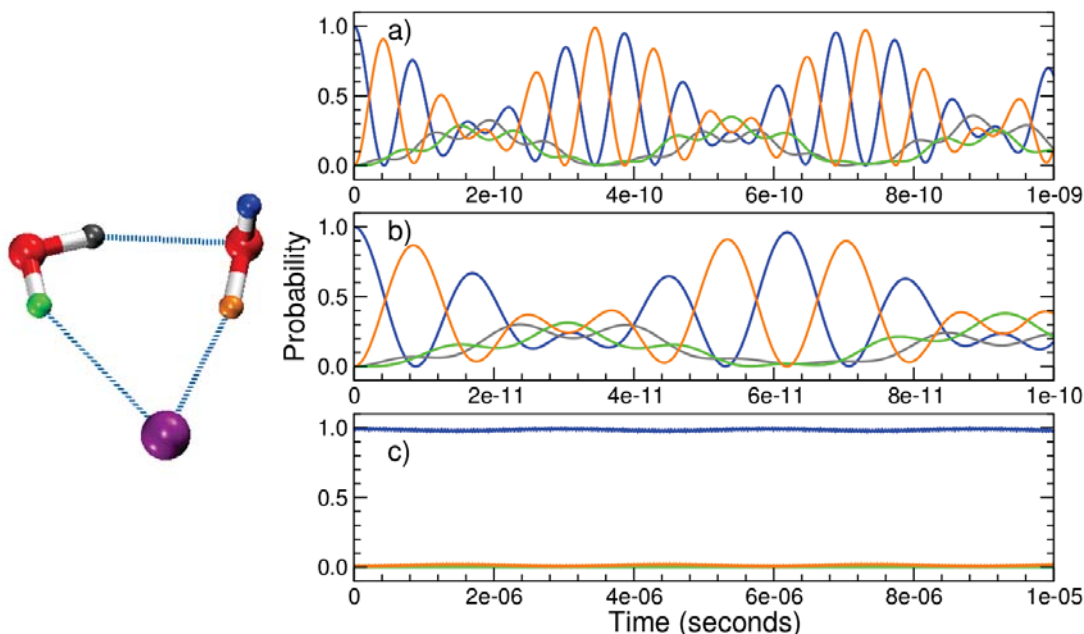
Figure 3.3. Time evolution of the probabilities of each of the four positions of the hydrogen atom in the $I^-(H_2O)_2$ (a), $I^-(D_2O)_2$ (b) and $I^-(HOD)(D_2O)$ (c) clusters. The colors of the four curves correspond to the four different positions of the hydrogen atom.

be found in any of the four different positions at a later time t. Also shown in Figure 3.3c are the corresponding probabilities for the hydrogen atom of HOD in $I^-(HOD)(D_2O)$. As expected from the tunneling splitting values, $I^-(H_2O)_2$ displays faster tunneling dynamics compared to $I^-(D_2O)_2$. On the other hand, in the ground state of $I^-(HOD)(D_2O)$, the hydrogen atom is predicted to remain effectively locked-in in the free position.

Direct insights into the effects of iodide on the water-water H-bond rearrangement are gained from the comparison reported in Table 3.1 between the tunneling matrix elements calculated for both $I^-(H_2O)_2$ and $I^-(D_2O)_2$, and the corresponding values for the water dimer and trimer.[2] Although both water-water H-bond bifurcation and flip rotation follow pathways similar to those found in pure water complexes, the tunneling probabilities are significantly different. In particular, the water-water H-bond bifurcation dynamics in the iodide dihydrate complex is orders of magnitude faster than in the water trimer. The presence of the iodide ion drastically weakens the neighboring water-water H-bond, the energy barrier for the water-water H-bond bifurcation is 0.52 kcal/mol in the iodide dihydrate complex, which is more than a factor

54

Table 3.1. Tunneling matrix elements, $-h$, in cm^{-1} for pure water clusters (from Ref. 2) and for $I^-(H_2O)_2$ and $I^-(D_2O)_2$ (this work). Note that the equivalent of the flip in the water dimer is a slightly different mechanism, but still it does not break any H-bond so it is similar enough for comparison.

	$(H_2O)_2$	$(H_2O)_3$	$I^-(H_2O)_2$	$(D_2O)_2$	$(D_2O)_3$	$I^-(D_2O)_2$
i-w bif	-	-	5.9	-	-	1.2
w-w bif	0.035	~ 0.01	1.7	2.7E-4	3.0E-5	0.29
flip	5.5*	50	0.09	0.6	18	3.4E-3

of four lower than that in the water trimer ($\sim$2.34 kcal/mol). Since minimal rearrangement of the oxygen atoms is required for the iodide-water H-bond bifurcation, the associated pathway is characterized by a potential energy barrier that is lower by $\sim$0.06 kcal/mol and narrower by $\sim$24°, in full width at half maximum, than that found along the water-water H-bond bifurcation (see Figure 3.4). It should be noted that the shape of the barrier depends on the chosen reaction coordinate. As a consequence, the iodide-water H-bond bifurcation is faster than the water-water H-bond bifurcation, resulting in a larger tunneling splitting. Importantly, the flip rotation in the pure water complexes is faster than all water-water H-bond bifurcations, since it does not require breaking any H-bond. However, the same trend is not followed in the iodide dihydrate complex for which the flip rotation is particularly slow. This slower dynamics is explained by considering that the energy barrier for the flip rotation (1.11 kcal/mol) in the iodide dihydrate complex is more than two times higher than those associated with the iodide-water (0.47 kcal/mol) and water-water (0.52 kcal/mol) H-bond bifurcations, and more than four times higher than those associated with flip rotation in the water trimer (0.24 kcal/mol).[2]

3.4 Temperature-dependence of H-bond dynamics

Previous studies determined that the water-water H-bond in the iodide dihydrate complex starts breaking at $\sim$100 K, which leads to an open configuration with two dangling water molecules H-bonded to the iodide ion. To monitor the equilibrium between closed and open
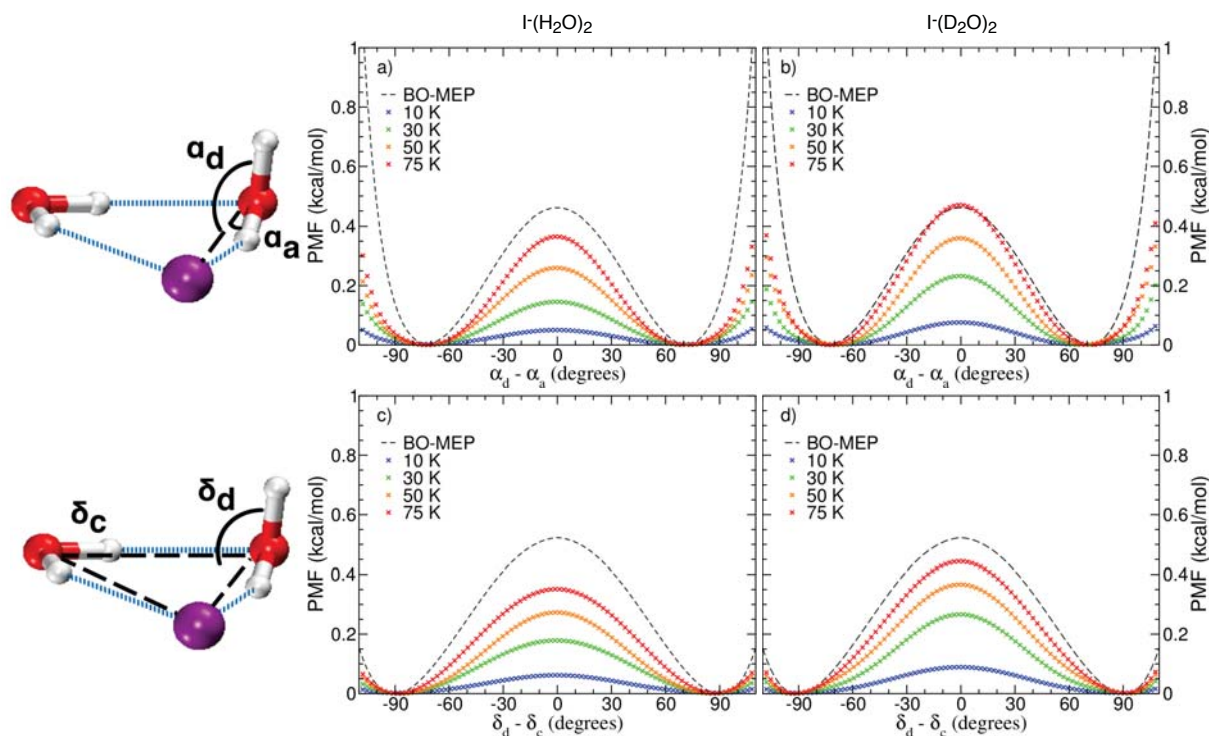
Figure 3.4. a) Potential of mean force (PMF) along the $\alpha_d - \alpha_a$ coordinate for the $I^-(H_2O)_2$ cluster. b) Same as in a) but for the $I^-(D_2O)_2$ isotopologue. c) PMF along the $\delta_d - \delta_c$ coordinate for the $I^-(H_2O)_2$ cluster. d) Same as in c) but for the $I^-(D_2O)_2$ isotopologue.

configurations and characterize the effects of tunneling on the H-bond dynamics as a function of temperature, path-integral molecular dynamics (PIMD) simulations are carried out for $I^-(H_2O)_2$ and $I^-(D_2O)_2$ between 10 K and 200 K. In agreement with the analysis of vibrational predissociation spectra[163], PIMD simulations predict that both complexes exist predominantly in closed configurations below 100 K (see Supporting Information).

Additional insights into the role played by tunneling in H-bonding rearrangements within $I^-(H_2O)_2$ and $I^-(D_2O)_2$ at finite temperature can be gained from the analysis of one-dimensional quantum free energies along the two collective variables describing iodide-water and water-water H-bond bifurcations calculated from the PIMD trajectories which are shown in Figure 3.4. For comparison, also shown are the associated minimum energy paths on the underlying Born-Oppenheimer potential energy surface. Below 50 K, both quantum free energy barriers for the two H-bond bifurcations are significantly lower than the corresponding Born-Oppenheimer

potential energy barriers. This implies that the OH and OD bonds in $I^-(H_2O)_2$ and $I^-(D_2O)_2$, respectively, undergo frequent interconversions between the four equivalent positions through the same large amplitude rotational tunneling motions identified by the RPI calculations, which emphasizes the purely quantum nature of both complexes at low temperature.

The interplay among ion-water and water-water interactions, entropic contributions, and nuclear quantum effects in the iodide dihydrate complex can be further characterized by investigating temperature-dependent H-bond rearrangements in the mixed isotopologue, $I^-(HOD)(D_2O)$. Isotopic substitution has been shown to be a powerful tool for determining H-bond rearrangements in water through vibrational spectroscopy, often enabling unambiguous spectral assignments which would be otherwise difficult to make due to strong inter-mode couplings.[1] Since the four distinct positions that the hydrogen atom can occupy within $I^-(HOD)(D_2O)$ are associated with different zero-point energies and entropic contributions, the total free energy of the complex in its closed configuration thus depends on the specific location of the hydrogen atom.

As shown in Figure 3.3c, the RPI calculations indicate that tunneling in $I^-(HOD)(D_2O)$ is completely suppressed at 0 K, with the hydrogen atom remaining locked-in in the free position. To monitor the evolution of the H-bond dynamics as a function of temperature, PIMD simulations are carried out to calculate two-dimensional quantum free-energy surfaces, using the well-tempered metadynamics biasing approach,[169] along the H-O-I angle and H-O-I-O' dihedral angle which are employed as collective variables describing the iodide-water and water-water H-bond bifurcation motions, respectively (top panels of Figure 3.5). Also shown in the bottom panels of Figure 3.5 are the one-dimensional quantum free-energy curves associated with the two H-bond bifurcations along with the corresponding Born-Oppenheimer minimum potential energy paths analogous to those shown in Figure 3.4.

At 10 K, the configuration with the hydrogen atom in the free position still corresponds to the most stable structure of $I^-(HOD)(D_2O)$, lying approximately 0.1 kcal/mol below the other three configurations with the hydrogen atom in H-bonded positions. It should be noted that configuration *4* (see Figure 3.5), with the hydrogen atom belonging to the DD water molecule
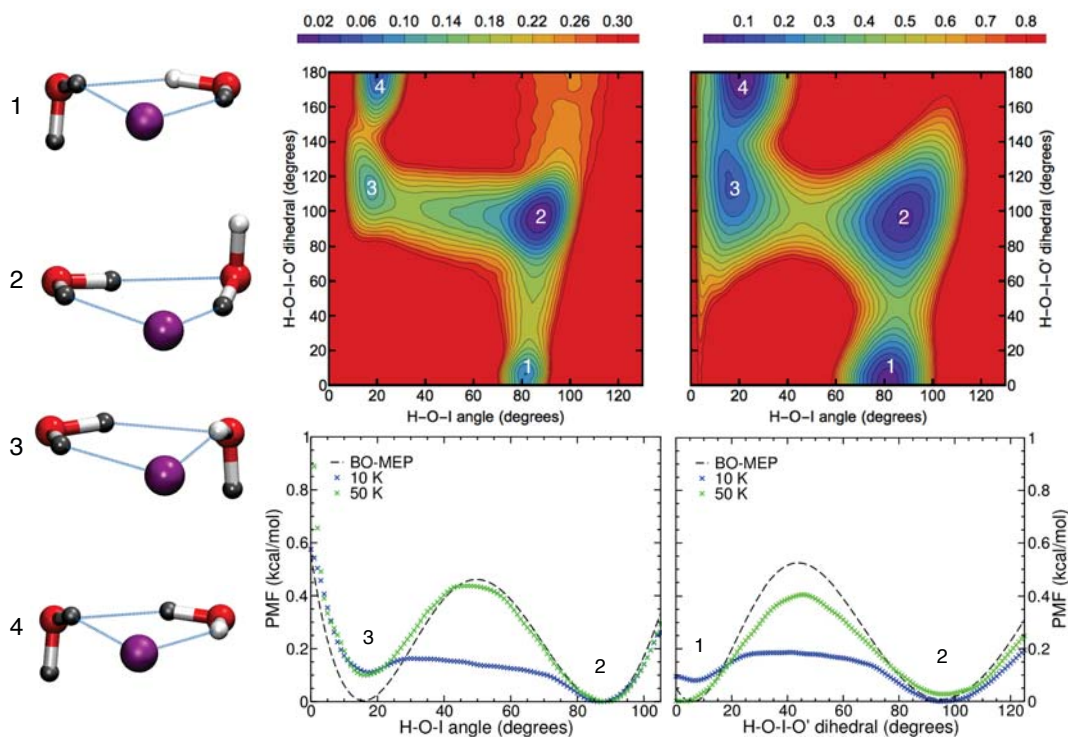
Figure 3.5. *Top*: Two dimensional PMF plots at 10 K (*left*) and 50 K (*right*), in kcal/mol, for the I⁻(HOD)(D₂O) complex along the H-O-I angle and H-O-I-O' dihedral. *Bottom*: One dimensional minimum PMF paths along the H-O-I angle (*left*) and the H-O-I-O' dihedral (*right*).

and H-bonded to the iodide ion, is not part of any direct bifurcation pathway and can only be reached through a second-order dynamical process involving the iodide-water H-bond bifurcation followed by the water-water H-bond bifurcation pathways. Besides breaking the symmetry of the 1D quantum free-energy profiles along both bifurcation pathways, the presence of the hydrogen atom in $I^-(HOD)(D_2O)$ also modifies the associated quantum free-energy barriers that become approximately three times higher than in the pure $I^-(H_2O)_2$ and $I^-(D_2O)_2$ complexes, but still appreciably lower than the corresponding barriers on the underlying Born-Oppenheimer potential energy surface. This suggests that tunneling may possibly occur in $I^-(HOD)(D_2O)$ at finite temperature although to a lesser extent than in $I^-(H_2O)_2$ and $I^-(D_2O)_2$. The average relative populations of the four different positions, however, will depend on the availability of accessible vibrational states at a particular temperature, governed by the Boltzmann distribution function. As shown in Figure 3.5, configuration 2 is at least 0.1 kcal/mol lower in free energy than the other configurations, which corresponds to a temperature of $\sim$50 K. Consequently, the other configurations will be stable and appreciably populated only at temperatures above 50 K.

Estimates of kinetic rates based on path-integral quantum transition state theory (PI-TST), with a neglect of any dynamical correction accounting for the possibility of barrier recrossing, indicates that the timescales for both iodide-water and water-water H-bond bifurcations in $I^-(HOD)(D_2O)$ at 10 K are on the order of milliseconds, and between 3 and 4 orders of magnitude slower than in $I^-(H_2O)_2$ and $I^-(D_2O)_2$ (see Supporting Information). It should be noted, however, that PI-TST only provides an approximation to a quantum rate, especially in the deep tunneling regime at low temperatures. In addition, compared to experiment, even small differences in barrier heights, which may be due to inaccuracies in the MB-nrg representation of the underlying Born-Oppenheimer potential energy surfaces, can result in large variations in the corresponding quantum rates. This implies that, in the present analysis, PI-TST rates can only serve to emphasize qualitative differences in the timescales associated with H-bonding rearrangements in $I^-(H_2O)_2$ and $I^-(D_2O)_2$, on one side, and $I^-(HOD)(D_2O)$, on the other side.

As the temperature increases, both 1D quantum free-energy profiles associated with the

iodide-water and water-water H-bond bifurcation pathways approach the corresponding Born-Oppenheimer minimum energy paths, leading to significantly faster H-bond rearrangements. At 50 K, PI-TST predicts timescales on the order of tens of nanoseconds for both bifurcations in $I^-(HOD)(D_2O)$, similar to those predicted for $I^-(H_2O)_2$ and $I^-(D_2O)_2$. Importantly, compared to 10 K, the two-dimensional free-energy surfaces shown in Figure 3.5 indicates that both H-bonded positions of the DD water molecule become relatively more stable at 50 K. This implies that local differences in zero-point energies become increasingly less important as the temperature increases, which thus explains the similarity between PI-TST rates predicted for the three different isotopologues at 50 K.

3.5   Conclusions

It is now established that, to a large extent, the unique properties of water can be traced back to its ability to form a dense yet highly dynamic H-bond network, in which both the number and strength continuously fluctuate. The continuous rearrangement of the H-bond network involves the forming and breaking of H-bonds, which is accompanied by simultaneous reorientation of individual water molecules through large amplitude angular jumps. By combining polarization-resolved, femtosecond mid-infrared, pump-probe spectroscopic measurements with molecular dynamics simulations, previous studies demonstrated that nuclear quantum effects play a nonnegligible role in the water reorientation dynamics in bulk solutions. Surface-specific isotope effects were also observed in mixtures of light and heavy water, while tunneling pathways leading to concerted H-bond rearrangements were identified in small water clusters from high-resolution spectroscopic measurements and quantum calculations.[2,167,172,173,175–179]

While some consensus on the molecular mechanisms responsible for H-bond rearrangements in pure water systems has started emerging in the past decade, the extent to which the structure and dynamics of the water H-bond network is altered by the presence of ions remains elusive. The traditional classification of small and highly charged ions as "structure makers"

and large, monovalent ions as "structure breakers", which finds support in measurements of macroscopic properties (e.g., viscosity and ion mobility), has been challenged by measurements carried out using different spectroscopic techniques, which suggest that dissolved ions have no influence on the water H-bond beyond the first hydration shell. However, this picture is at odds with that derived from infrared photodissociation spectra of sulfate ions in water clusters and recent femtosecond elastic second harmonic scattering measurements of highly dilute salt solutions. Alternative explanations of apparent long-range effects have also been proposed from computer simulations.

Halide-water clusters are ideal systems for characterizing the molecular mechanisms associated with H-bond rearrangements within the hydration shells of an ion, since, due to their relatively small sizes, they are amenable to high-level molecular modeling and, at the same time, can be studied experimentally using high-resolution vibrational spectroscopy. In this context, halide dihydrates hold a special place since are the smallest complexes in which two water molecules can be simultaneously H-bonded to each other and to the ion.

By combining accurate many-body representations of iodide-water and water-water interactions with state-of-the-art quantum dynamics simulations, this study provides first evidence for the existence of tunneling pathways in $I^-(H_2O)_2$. A detailed analysis of the underlying mechanisms indicates that tunneling leads to fast H-bond rearrangements mediated by the iodide ion. These rearrangements involve large amplitude rotations of the water OH bonds and result in the four hydrogen atoms exchanging their positions on a picosecond timescale even at low temperature. Identical pathways are observed, upon isotopic substitution, in $I^-(D_2O)_2$, although the associated H-bond dynamics is significantly slowed down. Further insights into the competition between iodide-water and water-water interactions, and the role played by nuclear quantum effects are gained from the analysis of H-bond rearrangements in the $I^-(HOD)(D_2O)$ isotopologue. By breaking the symmetry along the tunneling pathways, the presence of the hydrogen atom allows for precisely probing quantum free-energies associated with the four different bonding topologies within the complex. Due to local differences in zero-point energies

and entropic contributions, it is found that interconversion between the four different isotopomers of $I^-(HOD)(D_2O)$ is largely suppressed at low temperature, indicating that the mechanisms associated with H-bond rearrangements in the iodide-dihydrate complex can effectively be manipulated by isotopic substitutions. As the temperature increases, nuclear quantum effects become progressively less important, with all different isotopologues exhibiting similar H-bond dynamics above 75 K. It is interesting to note that alternatively to an increase in temperature, the interconversion in $I^-(HOD)(D_2O)$ could be facilitated by an inert "messenger-tag" molecule like D_2 or Ar (commonly used in predissociation vibrational spectroscopy) which would increase the density of states that are accessible at low temperatures.

Compared to the water trimer, the present results demonstrate that the iodide ion weakens the water-water H-bond, leading to significantly faster tunneling dynamics. Importantly, the flip rotation, which is the fastest motion in the water trimer becomes the slowest in the iodide dihydrate complex, due to a higher rotational barrier resulting from iodide-water interactions. Although these results clearly indicate that the iodide ion perturbs water-water H-bond rearrangements, the predicted faster dynamics in the iodide dihydrate complex is apparently at odds with ultrafast vibrational spectroscopy measurements of salt solutions, which suggest that the H-bond dynamics within the first hydration shell of iodide is significantly slowed down compared to that of pure water. This difference can be attributed to the presence of a free OH bond in the iodide dihydrate complex, which effectively triggers the overall H-bond rearrangement within the complex and enable faster water reorientation along both iodide-water and water-water H-bond bifurcation pathways. In turn, the present quantum simulations of the iodide dihydrate complex provides indirect evidence for the importance of cooperative effects in water H-bond rearrangements around iodide ions in solution, which, involving water molecules beyond the first hydration shell, thus slows down the overall dynamics, reversing the trend observed in the gas phase.

The present theoretical analysis thus raises the possibility that faster H-bond dynamics in the first hydration shell of iodide ions may be observed in frustrated systems, such as interfaces,

where water molecules H-bonded to the ion can be undercoordinated, with at least one dangling OH bond. Furthermore, since the H-bond rearrangement pathways identified in the iodide dihydrate complex directly depend on the nature of the iodide-water interaction, ion-specific effects on the H-bond dynamics are predicted to also exist in chloride dihydrate and bromide dihydrate complexes, which display similar minimum-energy cyclic structures, and possibly in the first hydration shell of both chloride and bromide ions in solution.

This chapter, in full, has been submitted for publication of the material as it may appear in "Ion-mediated hydrogen bond rearrangement through tunneling in the iodide dihydrate complex", 2018. Bajaj, Pushp; Richardson, Jeremy O.; Paesani, Francesco; Nature Chemistry, 2018. The dissertation author was the primary investigator and author of this paper.

Chapter 4

Halide ion micro-hydration: structure, energetics and spectroscopy of small halide-water complexes

4.1 Introduction

Decoding the structure and properties of aqueous ionic solutions across phases has been a monumental and long sought-after goal in the physical sciences. Ionic solutions are ubiquitous in nature and often mediate fundamental chemical, biological, environmental and industrial processes.[3,4,6,7,13,147,180,181] For instance, alkali and alkaline-earth metal ions like Ca^{2+}, Na^+, K^+ and Mg^{2+} play an important role in biological processes that are responsible for the rigidity and hardness of bones and teeth, blood clotting, muscle contraction, transport of water and nutrients through cell membranes, to name a few. Aqueous ions in sea spray aerosol (SSA) particles in the atmosphere alter their size, composition and physical and chemical properties. The presence and abundance of specific ions have been linked to the reactive uptake of gases, the hygroscopicity and interfacial reactions of aerosol particles.[11,182–184] SSA particles have huge impacts on Earth's climate, directly by scattering incoming solar radiation, and indirectly by changing cloud properties, all of which is a function of their size and composition.[185]

Properties of aqueous ionic solutions depend crucially on how ions affect the structure and dynamics of the water molecules around them, particularly the water hydrogen bonding (H-

bonding) network. While some ion characteristics like high charge density and electronegativity are considered disruptive to the water-water H-bonding environment. Low ion charge density and electronegativity are found to slightly strengthen the water-water H-bonds in the vicinity. A robust quantitative understanding of the magnitude and extent to which specific ions disrupt or enhance the water H-bonding network is yet to be achieved.[13,149] In this context, studies of small gas-phase clusters can provide molecular level insights into the fundamental questions regarding the strength of intermolecular interactions, the H-bonding arrangement, and reactivity.[158] The small size also makes these systems amenable for *ab initio* electronic structure calculations that are typically computationally intractable for bulk condensed phase systems. In turn, they can be used as model systems to test and validate ion-water interaction potentials.[56,76] Additionally, studying ion-water clusters with increasing size provides a systematic bottom up approach to understanding ion hydration, one hydration shell at a time.

Reported over the past couple of decades, many computational studies have focussed on determining the structures, relative energies and vibrational spectra of aqueous ionic clusters.[92,151,157,159,186–188] Halide ion hydration presents a particularly challenging problem, where due to strong and directional halide-water H-bonds, the water-water H-bonding network in the vicinity of the ion could be significantly affected.[158] Moreover, the strength of the halide-water intermolecular interactions changes drastically going from fluoride to iodide ion. Early theoretical investigations used *ab initio* models based on density functional theory (DFT) and perturbation theory based methods like MP2, with relatively small electronic basis sets, to describe the molecular interactions.[92,151,152,157,186,189] However, due to the high computational cost associated with *ab initio* electronic structure calculations, such studies are often limited to small system sizes (less than 10 molecules). More recently, the development of analytical polarizable interaction models has facilitated studies of gas-phase clusters through molecular dynamics simulations and vibrational spectra calculations.[75,77,115,160,190] The results vary significantly depending on the accuracy of the interaction model used and the nuanced competition between ion-water and water-water intermolecular interactions. An accurate way to account for

anharmonic electronic effects and a robust description of nuclear quantum effects are needed for a quantitative agreement with experimental measurements. That is why, despite many efforts a unified understanding of the structural, thermodynamic and spectroscopic properties has not been achieved.

In this study, we provide insights into the interplay between halide-water and water-water H-bonding strength and arrangement in halide-water clusters, and how it impacts the vibrational spectroscopy and thermodynamic properties of these gas phase clusters. Replica exchange molecular dynamics (REMD) simulations of $X^-(H_2O)_n$ clusters, where $X^- = F^-$, Cl^-, Br^- and I^-, and $n = 3\text{-}6$, are performed using recently developed, transferable many-body potential energy functions (PEFs) for halide-water interactions, called MB-nrg.[37,75] We explore the various minimum energy structural isomers of the $X^-(H_2O)_n$ clusters, their relative energies and anharmonic vibrational spectra. We, then, study the temperature dependent evolution of the clusters through calculations of the relative populations of the different isomers as a function of temperature. This article provides the foundation for a systematic approach to understanding halide ion hydration with increasing system size and complexity, going from small clusters to bulk condensed phase systems.

4.2   Computational methods

Following the MB-pol, many-body polarizable potential for water,[57–59] the MB-nrg PEFs for halide-water interactions are based on the many-body expansion of the interaction energy.[37] The two-body halide-water interaction energy is described through a combination of permanent and induced electrostatics (as per the Thole-type model[66]) and dispersion interactions, in the long range, and a set of permutationally invariant polynomials (PIPs), derived from highly accurate electronic structure calculations, in the short range. The PIPs are made up of transformed variables of all internuclear distances, and fitted to reproduce interaction energies calculated at the CCSD(T)-F12/CBS level of theory for more than 12000 dissimilar $X^-(H_2O)$

dimer configurations, in order to accurately reproduce the complex quantum in the short range. All higher order many-body interactions are included implicitly through classical induction forces using a modified version of the Thole-type model. A more detailed description of the MB-nrg functional form and development is provided in Ref. 37 and 75.

Within the MB-nrg framework, the intramolecular water distortions and intermolecular water-water interactions are described using the MB-pol water model which has been shown to reproduce the properties of water across all phases, from small gas-phase clusters to bulk liquid water and interfaces with unprecedented accuracy.[61–63,65,167] Through comparisons with various DFT models and classical polarizable models, the MB-nrg PEFs have been shown to accurately reproduce the global halide-water dimer potential energy surface, the harmonic and anharmonic vibrational frequencies of all four halide-water dimers.[37,56,75] An accurate and consistent description of both water-water and ion-water many-body interactions, provides a unique capability to study ion hydration like never done before.

Classical molecular dynamics (MD) simulations were performed in combination with the replica exchange (RE-) method[191] for efficient, ergodic sampling of the potential energy surface. In the REMD technique, multiple replicas of the system are run at different temperatures in parallel, with frequent exchange between the replicas, based on a metropolis criterion,[192]

$$P(\beta_A \leftrightarrow \beta_B) = \min[1, e^{-\Delta}],$$

$$\Delta = [\mathscr{U}_M(q_A) - \mathscr{U}_M(q_B)](\beta_B - \beta_A) + [\mathscr{K}_M(q_A) - \mathscr{K}_M(q_B)](1/\beta_B - 1/\beta_A),$$

where, $\beta = 1/k_B T$, with k_B being the Boltzmann's constant. For each of the $X^-(H_2O)_3$ and $X^-(H_2O)_4$ clusters, 64 replicas were used in the temperature range of 10 K to 200 K. For the $X^-(H_2O)_5$ clusters, 64 replicas were run in parallel in the temperature range of 10 K to 150 K and for the $X^-(H_2O)_6$ clusters, 96 replicas were employed in the temperature range of 10 K to 200 K. The specific choice for the number of replicas and the temperature range was made to optimize the computational cost and sampling of the global potential energy surfaces. The simulations were performed using an in-house C++ REMD code.

The intramolecular vibrational frequencies of the water molecules in the low energy

isomers for all $X^-(H_2O)_n$ clusters were calculated using a combined local-mode[125,126] and local-monomer[193] approach, as described in Ref. 128. The Hessian matrix was computed at the optimized geometry of each cluster from finite-differentiation of analytic first derivatives of the MB-nrg halide-water PEFs. Local modes[125,126,129] were then created using a distance-based (Boys) localization scheme in a frequency window of 500 cm^{-1}. The three highest-frequency modes, corresponding to the two stretching modes and one bending mode of a water molecule, were identified and used to integrate the potential energy using Gauss-Hermite quadrature on a grid of 9 points in each dimension. The "local-monomer" Hamiltonian[130,131] was diagonalized, in this reduced three-dimensional space composed of the local modes for each water monomer, to yield anharmonic eigen-frequencies and eigenvectors. Since, for each quadrature grid point, the potential energy was evaluated for the whole cluster, environmental effects are included in the calculations, to some extent.

4.3   Structure and spectra of $X^-(H_2O)_n$ clusters

Configurations were extracted from the REMD simulation trajectories at regular time intervals, and optimized to explore all possible minimum energy structural isomers of all the $X^-(H_2O)_n$ clusters, where $X^- = F^-$, Cl^-, Br^- and I^-, and $n = 3\text{-}6$. Ten unique lowest energy isomers (five for $X^-(H_2O)_3$) were then obtained using an interatomic distances based RMSD criterion, for each $X^-(H_2O)_n$ cluster. The minimum energy isomers obtained this way for all four halide-water systems, are shown in Figures 4.1 through 4.4. Clearly, the $Cl^-(H_2O)_n$, $Br^-(H_2O)_n$ and $I^-(H_2O)_n$ systems display structures that are very similar to each other. The $F^-(H_2O)_n$ clusters display qualitatively different structural arrangements from the other halide ion-water clusters. This is consistent with previous experimental investigations using vibrational predissociation spectroscopy, which show that chloride, bromide and iodide ions show similar structural arrangements in small aqueous clusters while fluoride ion clusters are exceptionally different.[158] It is also well established that the stability of the structures depends on the subtle

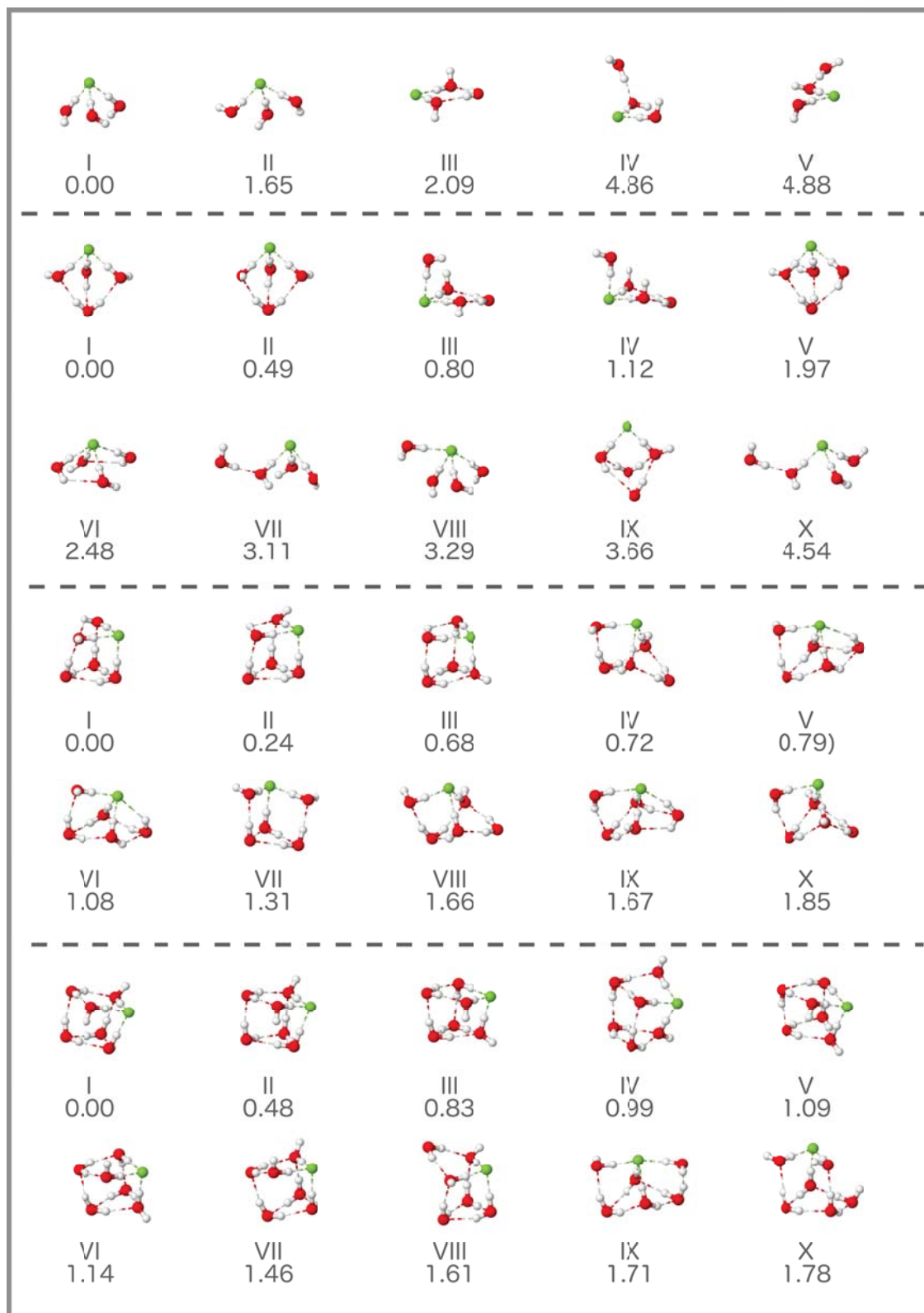**Figure 4.1.** Minimum energy structural isomers of the $F^-(H_2O)_n$ ($n = 3$-6) clusters along with their relative binding energies.
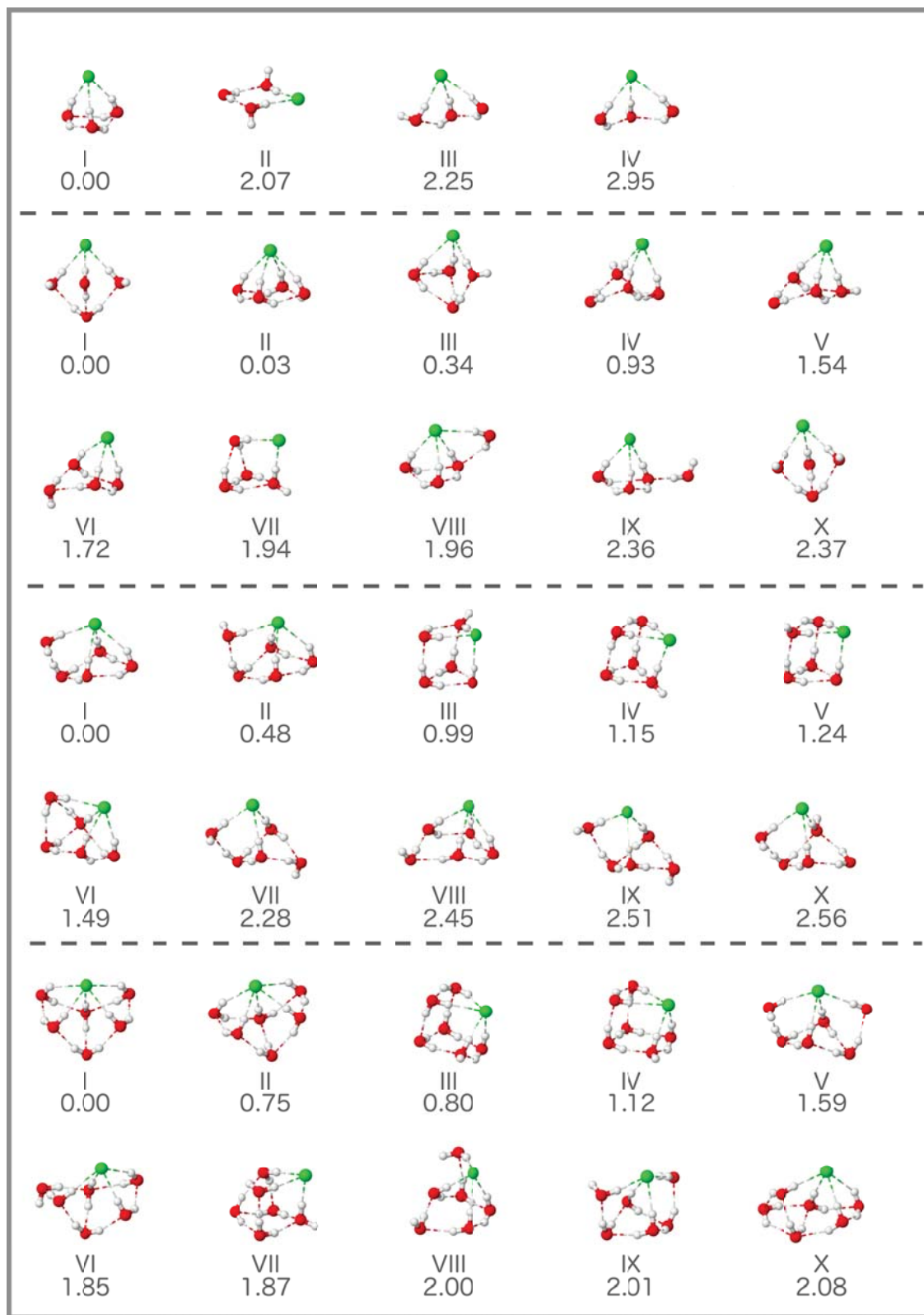
Figure 4.2. Minimum energy structural isomers of the $Cl^-(H_2O)_n$ ($n = 3\text{-}6$) clusters along with their relative binding energies.

balance between ion-water and water-water interactions.

Due to the small size and consequently high charge density and high covalent character of the fluoride ion, it forms strong, directional H-bonds with water. This effectively "pins" the water molecules in a particular arrangement, which in turn, significantly weakens the water-water H-bonding in the first hydration shell because of both, electronic effects and geometric constraints. This effect is seen for all cluster sizes and is particularly evident in the lowest energy structure of the $F^-(H_2O)_3$ cluster, where there are no water-water H-bonds due to the strong, short and directional fluoride-water H-bonds. The heavier halides are bigger in size and can accommodate more water molecules around them through relatively weak and less directional H-bonds. This allows the water molecules more freedom to reorient and optimize the number and strength of water-water H-bonds. As a result, the minimum energy isomers for all chloride-, bromide- and iodide-water clusters have a greater number of total (halide-water plus water-water) H-bonds compared to fluoride-water clusters.

It is noteworthy that, many of the isomers for all four halide-water systems, particularly for the larger cluster sizes, can be interconverted into each other by a simple rotation of one or two water molecules, changing slightly the H-bond topology. This simple rotation could lead to isomers that are significantly different in energy (0.2-0.7 kcal/mol). This suggests that many-body cooperative effects might be responsible for the stability of certain H-bond arrangements over others. Many-body effects and their role in determining the H-bonding topologies in $OH^-(H_2O)_n$ clusters were recently studied in great detail through highly accurate CCSD(T) calculations of the many-body interaction energies, and subsequent absolutely localized molecular orbital energy decomposition (ALMO-EDA) analysis.[194] It was found that many-body charge transfer and induction effects vary considerably depending on the relative distance and orientation of the fragment molecules, and play an important in determining the stability of a particular isomer. Hydroxide ions and fluoride ions have similar size, charge distribution and H-bonding strength. This further supports the notion that having an accurate description of many-body intermolecular interactions is necessary for a quantitative understanding of the structure and properties of ion-

water clusters.[63,158,194–196] An extensive analysis of the many-body effects in the halide-water clusters studied here, will be the subject of a future article.

Previous studies have also reported minimum energy isomers for the halide-water clusters studied here, obtained using *ab initio* electronic structure methods.[92,151,152,157,186,189] One aspect that is often debated is whether halide ions prefer the *surface* or *interior* position, with respect to the three-dimensional arrangement of the cluster. It is commonly found that the lowest energy arrangement of fluoride hydrates is the interior-type structure, where the ion is relatively more spherically solvated. While the heavier halide ion hydrates form surface-type structures, in the lowest energy arrangements, where the ion is on top of the water molecules. This has been attributed to the high covalent character and strong interactions with water, of the fluoride ion which are very different from the other halide ions. However, a conclusive agreement on the possible structural isomers and their relative stability is missing.[189] Contrary to previous studies, in our analysis no such interior-type structures were found as stable isomers for any of the $X^-(H_2O)_n$ ($n = 3\text{-}6$) clusters, at least in the ten lowest energy isomers reported here.

As mentioned above, the stability of the clusters depends on the competition between halide-water and water-water intermolecular interactions. The small basis sets and/or approximate DFT methods, used most commonly, have been shown to produce significant system-dependent errors in binding energies, many-body interaction energies and vibrational frequencies in pure water, cation-water and anion-water clusters.[37,56,64,65,76,194,197,198] In many cases, it was found that large error cancellations in the many-body interaction energies give a false impression of high accuracy in total binding energy comparisons for particular structural isomers. It is important to note that, it is the relative error in the ion-water and water-water interactions that is the key, which varies greatly depending on the specific ion and the molecular configurations.[37,56,65,194] Among the DFT models, only the most sophisticated range-separated dispersion-corrected hybrid functionals approach chemical accuracy in describing many-body ion-water interactions. However, such functionals are rarely employed in molecular dynamics simulations or extensive minima search algorithms due to the prohibitively high computational cost.

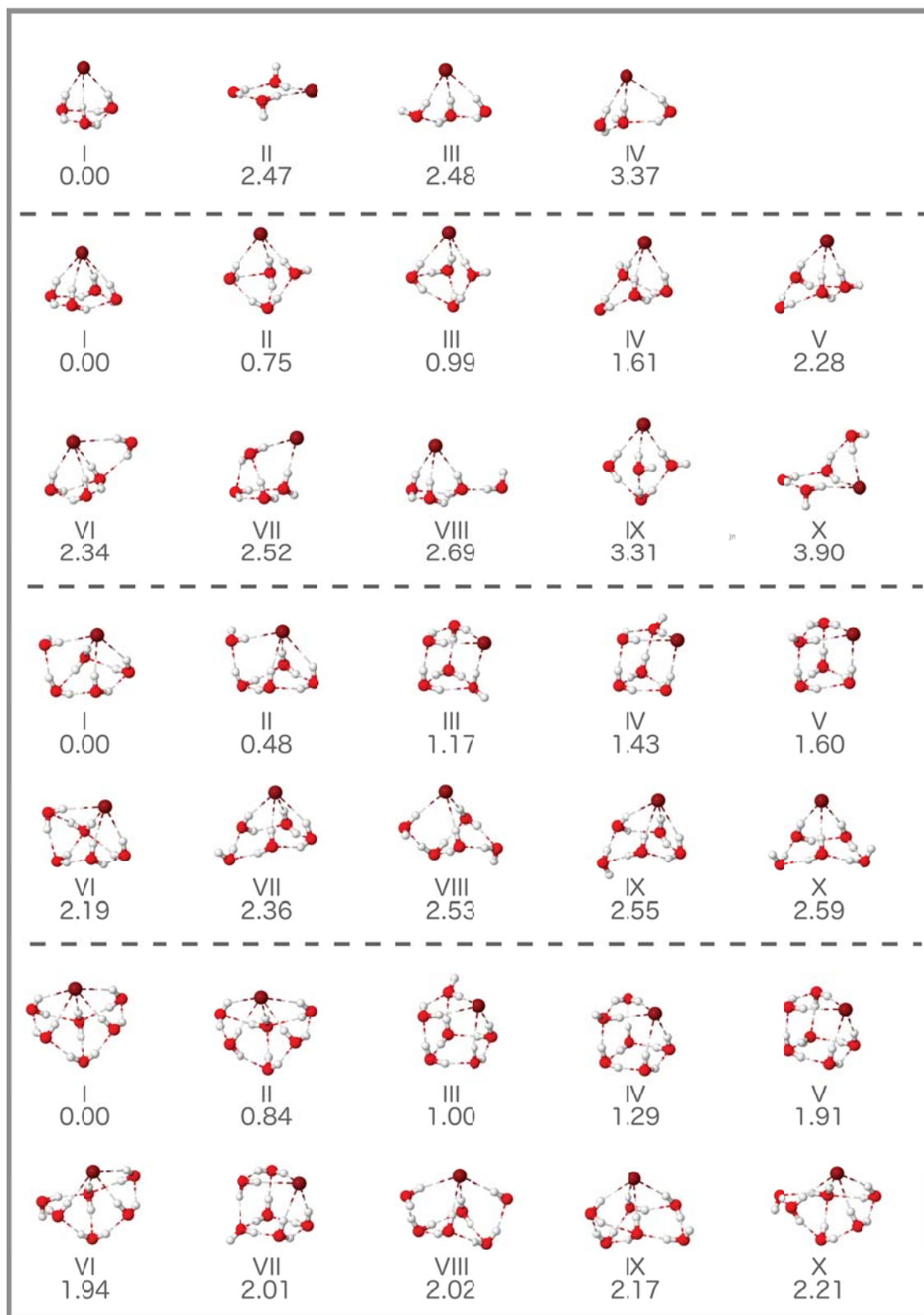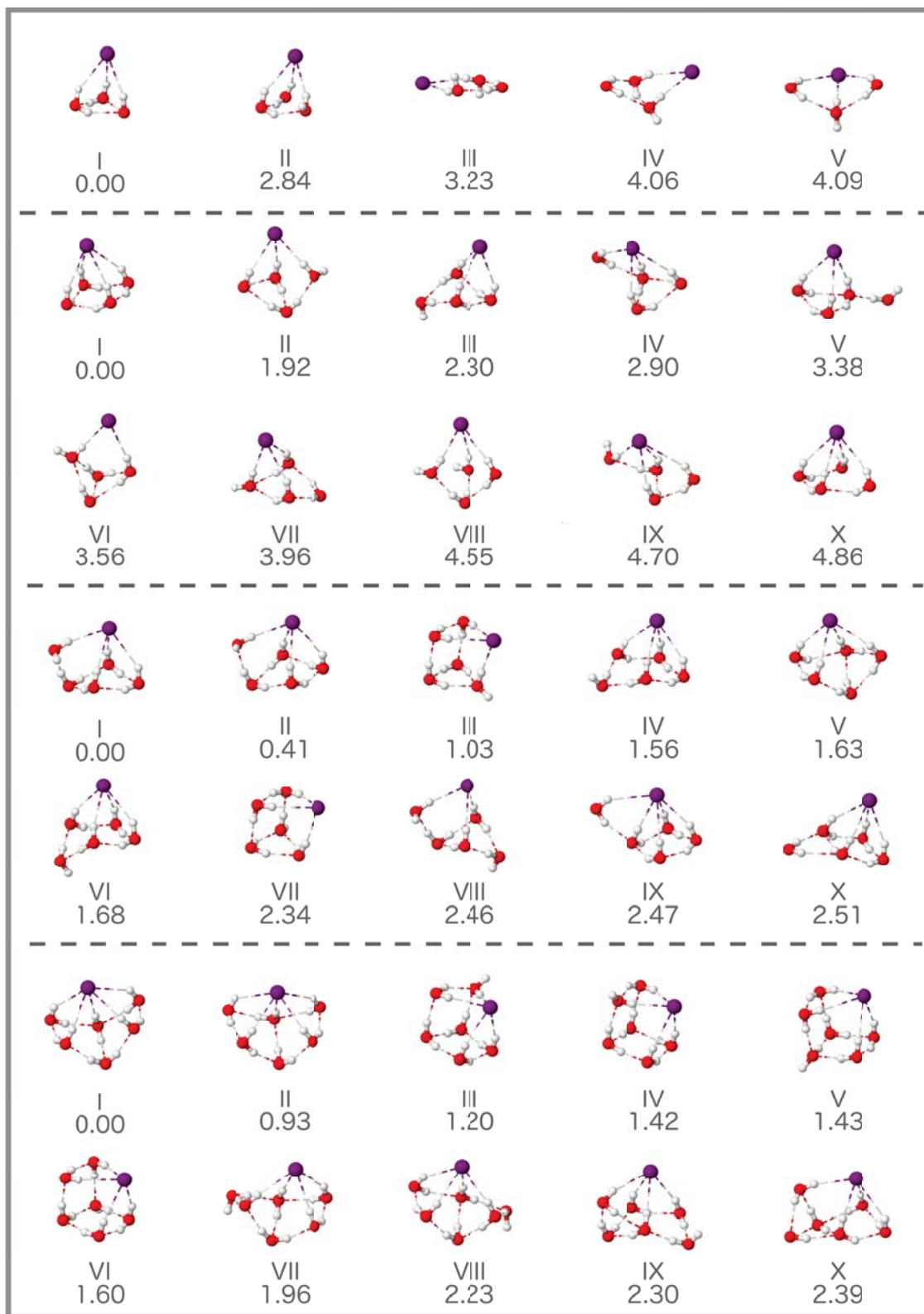**Figure 4.3.** Minimum energy structural isomers of the $Br^-(H_2O)_n$ ($n = 3$-6) clusters along with their relative binding energies.

Figure 4.4. Minimum energy structural isomers of the $I^-(H_2O)_n$ ($n = 3$-6) clusters along with their relative binding energies.

74

To provide further insights into the nature of halide-water interactions in $X^-(H_2O)_n$ clusters, anharmonic vibrational spectra of the global minimum energy isomers were calculated which are a direct probe of the strength of intermolecular interactions. Shown in Figure 4.5, the calculations were performed using the combined local-mode[125,126] and local-monomer approach[127] as introduced in Ref 128. Most notably, the more red shifted peaks in the hydrogen bonded OH stretching region move to higher frequencies, going from $F^-(H_2O)_n$ clusters to $I^-(H_2O)_n$ (along the columns in Figure 4.5). These peaks correspond to the OH bonds that are H-bonded to the halide ions. This is a manifestation of the decreasing strength of the halide-water H-bond, going from F^- to Cl^-, to Br^- and I^-. On the other hand, the opposite trend can be seen for the peaks corresponding to the OH bonds forming inter-water H-bonds lying in $\sim$3450-3550 cm^{-1} region. Going from Cl^- to I^-, particularly for three and four water clusters, these peaks shift slightly toward lower frequencies indicating increasing strength of water-water H-bonds. These trends are consistent with previously reported experimental measurements.[153,158] The remarkably high basic character of F^- and consequently much stronger H-bonding ability, compared to other halides, results in qualitatively different structures and spectra of the $F^-(H_2O)_n$ clusters compared to the other halide-water clusters. Interestingly, due to the symmetrical arrangement of the chloride-, bromide-, and iodide-water clusters, the peaks in their vibrational spectra overlap and are more localized, as compared to the fluoride-water clusters.

The spectra calculated here, can be directly compared to experimental vibrational spectra measured using infrared predissociation spectroscopy using cold ion traps and "messenger" technique, where the cluster will likely appear in its minimum energy configuration. However, experimental spectra at finite temperatures measure the response from an ensemble of different molecular configurations, particularly the low energy isomers discussed above. For a one-to-one comparison with finite temperature measurements, the theoretical spectra of the individual isomers must be weighted by the thermal, preferably quantum, distribution at that temperature.[128] This is certainly an interesting and worthy endeavor but, it is not a focus of this study.
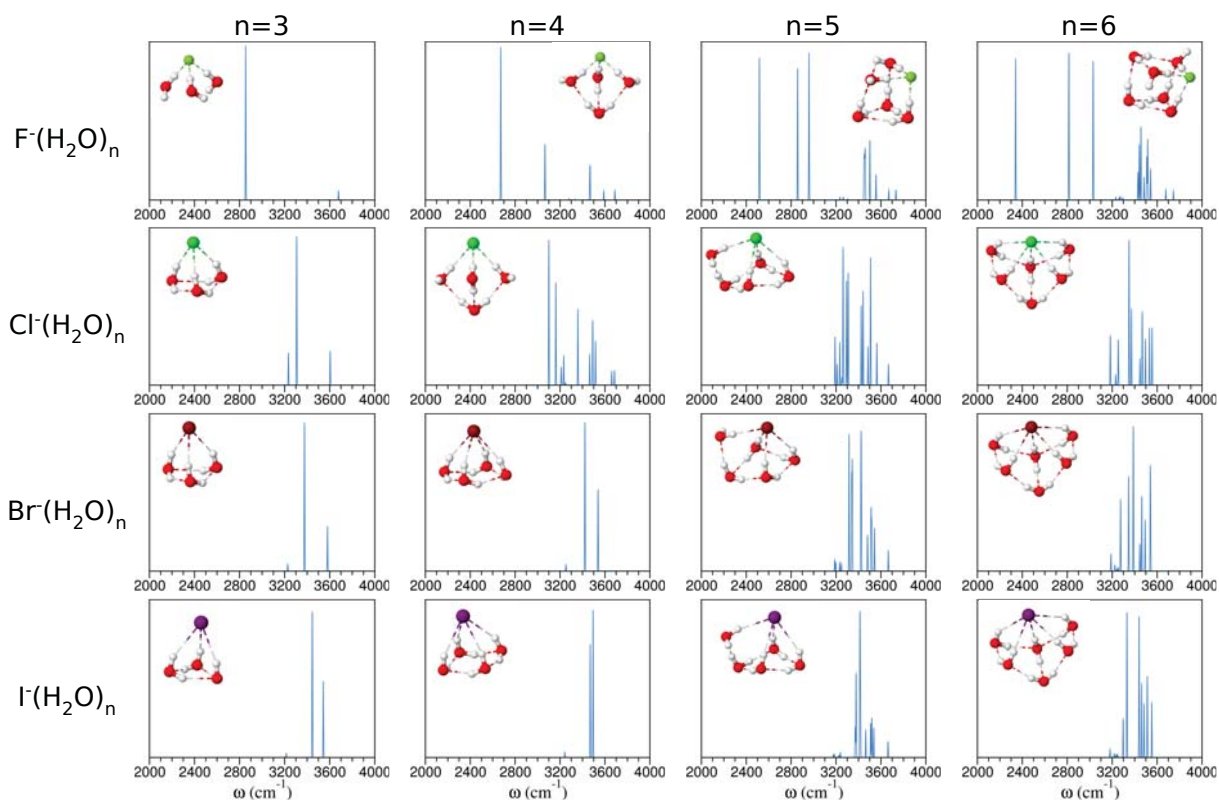
Figure 4.5. Calculated anharmonic vibrational spectra of global minimum energy structural isomers of the $X^-(H_2O)_n$ clusters, where $X^- = F^-$, Cl^-, Br^- and I^-, and $n = 3$-6.

4.4 Temperature dependent evolution of $X^-(H_2O)_n$ clusters

In order to study the temperature dependent evolution of the $X^-(H_2O)_n$ clusters, classical populations of the different isomers were calculated in a range of temperatures from 10 K to 150 K, depicted in Figure 4.6. Configurations were extracted from the simulation trajectories at regular time intervals and optimized to the nearest local minimum on the potential energy surface. Considering only the positions of the heavy atoms, the optimized configuration was then classified as one of the 10 stable isomers (5 for $X^-(H_2O)_3$) using a RMSD criterion. As expected, the results show that at low temperatures only the lowest energy isomer dominates the equilibrium Boltzmann distribution for each cluster. At higher temperatures, for most chloride-, bromide- and iodide-water clusters, the next higher energy isomer was found to contribute increasingly to the distribution. Higher energy isomers contribute little to the distribution even at 150 K. In the case of fluoride-water clusters, however, multiple isomers gain comparable populations with increasing temperature. As mentioned before, in order to obtain a quantitative understanding and make direct comparisons with experiments, quantum distribution of the different isomers is needed, which is not a focus of this study.

4.5 Conclusions

Halide-water clusters act as important model systems for understanding ion hydration, at the molecular level, being the smallest molecular systems where the interplay between halide-water and water-water interactions can be studied intimately. Moreover, a systematic study of increasing cluster sizes provides a bottom-up approach toward investigating bulk ion hydration in condensed phase systems. However, the anharmonic, quantum mechanical halide-water interactions and the competition halide-water and water-water interactions present a challenging problem for theoretical and computational modeling.

In this study, we provide insights into the specific ion effects among the halide ions through investigations of the H-bonding strength and arrangement in $X^-(H_2O)_n$ clusters, where
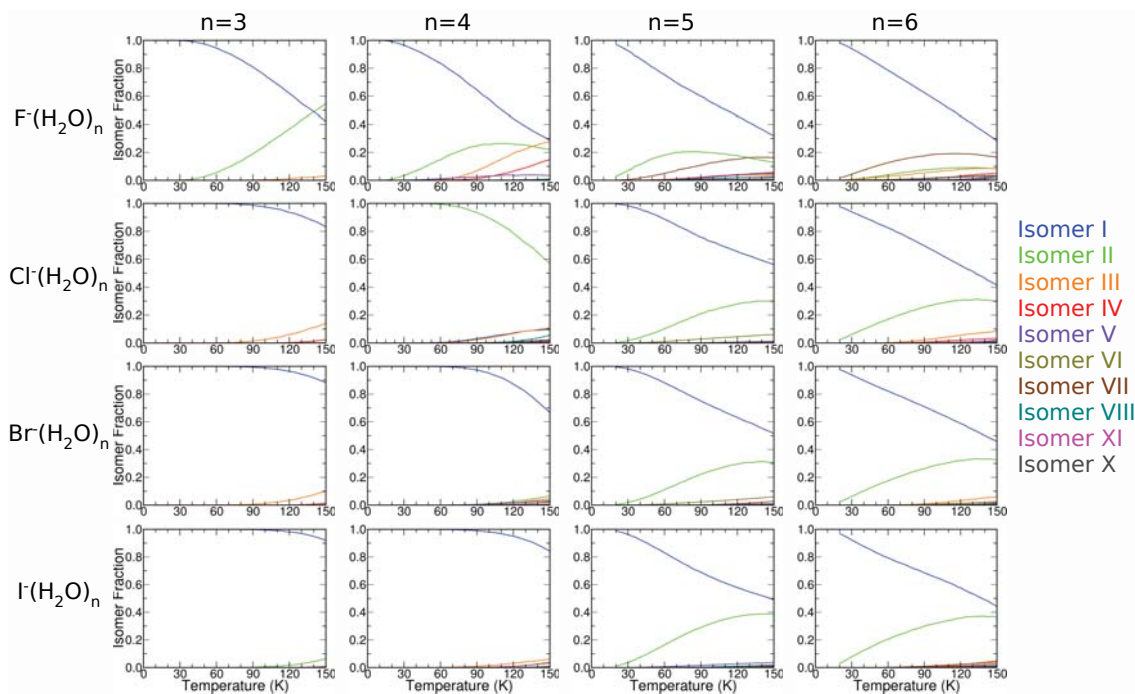
Figure 4.6. Temperature dependent relative populations of the minimum energy isomers for the $X^-(H_2O)_n$ clusters, where $X^- = F^-$, Cl^-, Br^- and I^-, and $n = 3\text{-}6$.

$X^- = F^-$, Cl^-, Br^- and I^-, and $n = 3\text{-}6$. Through REMD simulations combined with *ab initio* based many-body PEFs, called MB-nrg, to describe halide-water interactions, we identify and report low energy structural isomers for all four halide-water systems. While chloride-, bromide- and iodide-water clusters exhibit similar structural arrangements, due to similar H-bonding strengths. Fluoride-water clusters display qualitatively different configurations, highlighting the exceptionally strong intermolecular interactions between fluoride ion and water. In general, it is found that all four halide-ions prefer exterior positions in the cluster, forming "surface"-type structures, in order to optimize the number and strength of halide-water and water-water H-bonds. Anharmonic vibrational spectra, calculated using the MB-nrg PEFs, are reported for the global minimum energy isomers for all $X^-(H_2O)_n$ clusters which are a direct probe of the structure and strength of intermolecular interactions. The vibrational spectra further quantify the dramatic changes in the halide-water and water-water H-bonding strengths going from fluoride to iodide ion. Finally, we report the evolution of the clusters as a function temperature by computing the

classical populations of the different structural isomers for a range of temperatures.

Future work will focus on determining the role of nuclear quantum effects in the temperature dependent distribution of the structural isomers of the halide-water clusters and their vibrational spectra, which will enable direct comparisons with experimental measurements. It should be noted that, the MB-nrg halide-water potentials used in this study include many-effects through classical electrostatics, permanent and induced. The short-range, quantum mechanical two-body effects are described using permutationally invariant polynomials (PIPs), that are fitted to electronic structure data at CCSD(T)-F12/CBS level of theory, in addition to classical electrostatics and dispersion forces. In future developments of the model, the three-body (3B) halide-water PIPs will be introduced to describe the short-range quantum mechanical 3B effects, in addition to classical induction, which would further improve the overall accuracy of the model. It would interesting to see what, if any, effect that has on the relative order of stability of the different isomers for the $X^-(H_2O)_n$ clusters.

This chapter, in part is currently being prepared for submission for publication of the material. Bajaj, Pushp; Lin, Jason K.; Riera, Marc; Gazca, Jessica; Mendoza, Yaira; Paesani, Francesco; "Halide ion microhydration: structure, energetics and spectroscopy of small halide-water clusters". The dissertation author was the primary investigator and author of this material.

Bibliography

[1] Yang, N.; Duong, C. H.; Kelleher, P. J.; Johnson, M. A.; McCoy, A. B. *Chem. Phys. Lett.* **2017**, *690*, 159–171.

[2] Richardson, J. O.; Althorpe, S. C.; Wales, D. J. *J. Chem. Phys.* **2011**, *135*, 124109.

[3] Collins, K. D.; Neilson, G. W.; Enderby, J. E. *Biophys. Chem.* **2007**, *128*, 95–104.

[4] Kunz, W. *Curr. Opin. Colloid Interface Sci.* **2010**, *15*, 34–39.

[5] Jungwirth, P.; Winter, B. *Annu. Rev. Phys. Chem.* **2008**, *59*, 343–366.

[6] Tobias, D. J.; Stern, A. C.; Baer, M. D.; Levin, Y.; Mundy, C. J. *Annu. Rev. Phys. Chem.* **2013**, *64*, 339–359.

[7] Knipping, E. M.; Lakin, M. J.; Foster, K. L.; Jungwirth, P.; Tobias, D. J.; Gerber, R. B.; Dabdub, D.; Finlayson-Pitts, B. J. *Science* **2000**, *288*, 301.

[8] Knipping, E. M.; Dabdub, D. *Environ. Sci. Technol.* **2003**, *37*, 275–284.

[9] Simpson, W. R. et al. *Atmos. Chem. Phys.* **2007**, *7*, 4375–4418.

[10] Calvert, J. G.; Lazrus, A.; Kok, G. L.; Heikes, B. G.; Walega, J. G.; Lind, J.; Cantrell, C. A. *Nature* **1985**, *317*, 27–35.

[11] Foestieri S. D., G. C., Cornwell; Helgestad, T. M.; Moore, K. A.; Lee, C.; Novak, G. A.; Sultana, C. M.; Wang, X.; Bertram, T. H.; Prather, K. A.; Cappa, C. D. *Atmos. Chem. Phys.* **2016**, *16*, 9003–9018.

[12] Collins, K. D. *Methods* **2004**, *34*, 300–311.

[13] Marcus, Y. *Chem. Rev.* **2009**, *109*, 1346–1370.

[14] Jungwirth, P.; Tobias, D. J. *J. Phys. Chem. B* **2001**, *105*, 10468–10472.

[15] Jungwirth, P.; Tobias, D. J. *J. Phys. Chem. B* **2002**, *106*, 6361–6373.

[16] Dang, L. X. *J. Phys. Chem. B* **2002**, *106*, 10388–10394.

[17] Dang, L. X.; T-M., C. *J. Phys. Chem. B* **2002**, *106*, 235–238.

[18] Peterson, P. B.; J., S. R. *Chem. Phys. Lett.* **2004**, *397*, 51–55.

[19] Peterson, P. B.; J., S. R. *J. Phys. Chem. B* **2006**, *110*, 14060–14073.

[20] Liu, D.; G., M.; Levering, L. M.; Allen, H. C. *J. Phys. Chem. B* **2004**, *108*, 2252–2260.

[21] Raymond, E. A.; L., R. G. *J. Phys. Chem. B* **2004**, *108*, 5051–5059.

[22] Winter, B.; Weber, R.; Schmidt, P. M.; Hertel, I. V.; Faubel, M.; Vrbka, L.; Jungwirth, P. *J. Phys. Chem. B* **2004**, *108*, 14558–14564.

[23] Ghosal, S.; Hemminger, J. C.; Bluhm, H.; Mun, B. S.; Hebenstreit, E. L. D.; Ketteler, G.; Ogletree, D. F.; Requejo, F. G.; Salmeron, M. *Science* **2005**, *307*, 563–566.

[24] Chang, T.-M.; Dang, L. X. *Chem. Rev.* **2006**, *106*, 1305–1322.

[25] Peterson, P. B.; J., S. R. *Annu. Rev. Phys. Chem.* **2006**, *57*, 333–364.

[26] Perera, L.; Berkowitz, M. L. *J. Chem. Phys.* **1991**, *95*, 1954–1963.

[27] Perera, L.; Berkowitz, M. L. *J. Chem. Phys.* **1992**, *96*, 8288–8294.

[28] Perera, L.; Berkowitz, M. L. *J. Chem. Phys.* **1993**, *99*, 4222–4224.

[29] Caldwell, J.; Dang, L. X.; Kollman, P. A. *J. Am. Chem. Soc.* **1990**, *112*, 9144–9147.

[30] Dang, L. X.; E., S. D. *J. Chem. Phys.* **1993**, *99*, 6950–6956.

[31] Grossfield, A.; Ren, P.; Netz, R. R. *J. Chem. Phys.* **2009**, *112*, 7455–7467.

[32] Stuart, S. J.; Berne, B. J. *J. Phys. Chem.* **1996**, *100*, 11934–11943.

[33] Stuart, S. J.; Berne, B. J. *J. Phys. Chem. A* **1999**, *103*, 10300–10307.

[34] Warren, G. L.; Patel, S. *J. Phys. Chem. C* **2008**, *112*, 7455–7467.

[35] Yu, H.; Whitfield, T. W.; Harder, E.; Lamoureux, G.; Vorobyov, I.; Anisimov, V. M.; MacKarell Jr., A. D.; Roux, B. *J. Chem. Theory Comput.* **2010**, *6*, 774–786.

[36] Horinek, D.; Mamatkulov, S. I.; Ponder, J. W. *J. Am. Chem. Soc.* **2003**, *125*, 15671–15682.

[37] Bajaj, P.; Götz, A. W.; Paesani, F. *J. Chem. Theory Comput.* **2016**, *12*, 2698–2705.

[38] Hankins, D.; Moskowitz, J. W.; Stillinger, F. H. *J. Chem. Phys.* **1970**, *53*, 4544.

[39] Xantheas, S. S. *J. Chem. Phys.* **1994**, *100*, 7523.

[40] Elrod, M. J.; Saykally, R. J. *Chem. Rev.* **1994**, *94*, 1975–1997.

[41] Xantheas, S. S. *Chem. Phys.* **2000**, *258*, 225–231.

[42] Defusco, A.; Schofield, D. P.; Jordan, K. D. *Mol. Phys.* **2007**, *105*, 2681–2696.

[43] Góra, U.; Podeszwa, R.; Wojciech, C.; Szalewicz, K. *J. Chem. Phys.* **2011**, *135*, 224102.

[44] Richard, R. M.; Lao, K. U.; Herbert, J. M. *J. Chem. Phys.* **2014**, *141*, 014108.

[45] Lao, K. U.; Liu, K.; Richard, R. M.; Herbert, J. M. *J. Chem. Phys.* **2016**, *144*, 164105.

[46] Kebarle, P. *Annu. Rev. Phys. Chem.* **1977**, *28*, 445–476.

[47] Mark, T. D.; Castleman, A. W. *Adv. At. Mol. Phys.* **1985**, *20*, 65–172.

[48] Castleman Jr., A. W.; Keesee, R. G. *Acc. Chem. Res.* **1986**, *19*, 413–419.

[49] Hiraoka, K.; Fujimaki, S.; Aruga, K.; Yamabe, S. *Chem. Phys. Lett.* **1993**, *208*, 491–496.

[50] Meot-Ner, M. *J. Am. Chem. Soc.* **1984**, *106*, 1265–1272.

[51] DeLuca, M. J.; Niu, B.; Johnson, M. A. *J. Chem. Phys.* **1988**, *88*, 5857.

[52] Markovich, G.; Giniger, R.; Levin, M.; Cheshnovsky, O. *J. Chem. Phys.* **1991**, *95*, 9416–9419.

[53] Marvovich, G.; Pollack, S.; Giniger, R.; Cheshnovsky, O. *J. Chem. Phys.* **1994**, *101*, 9344.

[54] Kima, J.; Beckerb, I.; Cheshnovsky, O.; Johnson, M. A. *Chem. Phys. Lett.* **1998**, *297*, 90–96.

[55] Neumark, D. M. *Annu. Rev. Phys. Chem.* **2001**, *52*, 255–277.

[56] Riera, M.; Mardirossian, N.; Bajaj, P.; Götz, A. W.; Paesani, F. *J. Chem. Phys.* **2017**, *147*, 161715.

[57] Babin, V.; Leforestier, C.; Paesani, F. *J. Chem. Theory Comput.* **2013**, *9*, 5395–5403.

[58] Babin, V.; Medders, G. R.; Paesani, F. *J. Chem. Theory Comput.* **2014**, *10*, 1599–1607.

[59] Medders, G. R.; Babin, V.; Paesani, F. *J. Chem. Theory Comput.* **2014**, *19*, 2906–2910.

[60] Medders, G. R.; Götz, A. W.; Morales, M. A.; Bajaj, P.; Paesani, F. *J. Chem. Phys.* **2015**, *143*, 104102.

[61] Medders, G. R.; Paesani, F. *J. Chem. Theory Comput.* **2015**, *11*, 1145–1154.

[62] Medders, G. R.; Paesani, F. *J. Am. Chem. Soc.* **2016**, *138*, 3912–3919.

[63] Paesani, F. *Acc. Chem. Res.* **2016**, *49*, 1844–1851.

[64] Cisneros, G. A.; Wikfeldt, K. T.; Ojamäe, L.; Lu, J.; Xu, Y.; Torabifard, H.; Bartók, A. P.; Csányi, G.; Molinero, V.; Paesani, F. *Chem. Rev.* **2016**, *116*, 7501–7528.

[65] Reddy, S. K.; Straight, S. C.; Bajaj, P.; Pham, H. C.; Riera, M.; Moberg, D. R.; Morales, M. A.; Knight, C.; Götz, A. W.; Paesani, F. *J. Chem. Phys.* **2016**, *145*, 194504.

[66] Burnham, C. J.; Anick, D. J.; Mankoo, P. K.; Reiter, G. F. *J. Chem. Phys.* **2008**, *129*, 154519.

[67] Tang, K. T.; Toennies, J. P. *J. Chem. Phys.* **1984**, *80*, 3726–3741.

[68] Johnson, E. R.; Becke, A. D. *J. Chem. Phys.* **2005**, *123*, 024101.

[69] Vydrov, O. A.; Scuseria, G. E. *J. Chem. Phys.* **2006**, *125*, 234109.

[70] Vydrov, O. A.; Heyd, J.; Krukau, A. V.; Scuseria, G. E. *J. Chem. Phys.* **2006**, *125*, 074106.

[71] Vydrov, O. A.; Scuseria, G. E.; Perdew, J. P. *J. Chem. Phys.* **2007**, *126*, 154109.

[72] Kannemann, F. O.; Becke, A. D. *J. Chem. Theory Comput.* **2010**, *6*, 1081–1088.

[73] Otero-de-la Roza, A.; Johnson, E. R. *J. Chem. Phys.* **2013**, *138*, 204109.

[74] Braams, B. J.; Bowman, J. M. *Int. Rev. Phys. Chem.* **2009**, *28*, 577.

[75] Bajaj, P.; Wang, X.-G.; Carrington Jr., T.; Paesani, F. *J. Chem. Phys.* **2018**, *148*, 102321.

[76] Arismendi-Arrieta, D. J.; Riera, M.; Bajaj, P.; Prosimiti, R.; Paesani, F. *J. Phys. Chem. B* **2016**, *120*, 1822.

[77] Wang, X.-G.; Carrington Jr., T. *J. Chem. Phys.* **2014**, *140*, 204306.

[78] Adler, T. B.; Knizia, G.; Werner, H. J. *J. Chem. Phys.* **2007**, *127*, 221106.

[79] Knizia, G.; Adler, T. B.; Werner, H. J. *J. Chem. Phys.* **2009**, *130*, 054104.

[80] Hill, J. G.; Peterson, K. A.; Knizia, G.; Werner, H. J. *J. Chem. Phys.* **2009**, *131*, 194105.

[81] Dunning, T. H. *J. Chem. Phys.* **1989**, *90*, 1007–1023.

[82] Kendall, R. A.; Dunning, T. H.; Harrison, R. J. *J. Chem. Phys.* **1992**, *96*, 6796–6806.

[83] Woon, D. E.; Dunning, T. H. *J. Chem. Phys.* **1993**, *98*, 1358–1371.

[84] Dunning T.H., J.; Peterson, K. A.; Wilson, A. K. *J. Chem. Phys.* **2001**, *114*, 9244–9253.

[85] Peterson, K. A.; Figgen, D.; Goll, E.; Stoll, H.; Dolg, M. *J. Chem. Phys.* **2003**, *119*, 11113–11123.

[86] Peterson, K. A.; Shepler, B. C.; Figgen, D.; Stoll, H. *J. Phys. Chem. A* **2006**, *110*, 13877–13883.

[87] Woon, D. E.; Dunning, T. H. *J. Chem. Phys.* **1994**, *100*, 2975–2988.

[88] Hättig, C.; Hess, B. A. *J. Chem. Phys.* **1998**, *108*, 3863–3870.

[89] Trumm, M.; Martinez, Y. O. G.; Réal, F.; Masella, M.; Vallet, V.; Schimmelpfennig, B. *J. Chem. Phys.* **2012**, *136*, 044509.

[90] Werner, H.-J. et al. MOLPRO, version 2015.1, a package of ab initio programs. 2015.

[91] Tikhonov, A. N. *Soviet Math.* **1963**, *4*, 1035–1038.

[92] Kim, J.; Lee, H. M.; Suh, S. B.; Majumdar, D.; Kim, K. S. *J. Chem. Phys.* **2000**, *113*, 5259–5272.

[93] Wang, Y.; Bowman, J. M.; Kamarchik, E. *J. Chem. Phys.* **2016**, *144*, 114311.

[94] Shi, Y.; Xia, Z.; Zhang, J.; Best, R.; Wu, C.; Ponder, J. W.; Ren, P. *J. Chem. Theory Comput.* **2013**, *9*, 4046–4063.

[95] Werhahn, J. C.; Akase, D.; Xantheas, S. S. *J. Chem. Phys.* **2014**, *141*, 064118.

[96] Wang, Q.; Rackers, J. A.; Chenfeng, H.; Rui, Q.; Narth, C.; Lagardere, L.; Gresh, N.;

Ponder, J. W.; Piquemal, J.; Ren, P. *J. Chem. Theory Comput.* **2015**, *11*, 2609–2618.

[97] Grimme, S.; Antony, J.; Ehrlich, S.; Krieg, H. *J. Chem. Phys.* **2010**, *132*, 154104.

[98] Becke, A. D. *Phys. Rev. A* **1988**, *38*, 3098.

[99] Lee, C.; Yang, W.; Parr, R. G. *Phys. Rev. B* **1988**, *37*, 785.

[100] Perdew, J. P.; Burke, K.; Ernzerhof, M. *Phys. Rev. Lett.* **1996**, *78*, 1396.

[101] Tao, J. M.; Perdew, J. P.; Staroverov, V. N.; Scuseria, G. E. *Phys. Rev. Lett.* **2003**, *91*, 146401.

[102] Adamo, C.; Barone, V. *J. Chem. Phys.* **1999**, *110*, 6158.

[103] Becke, A. D. *J. Chem. Phys.* **1993**, *98*, 5648.

[104] Chai, J.-D.; Head-Gordon, M. *J. Chem. Phys.* **2008**, *128*, 084106.

[105] Chai, J.-D.; Head-Gordon, M. *Phys. Chem. Chem. Phys.* **2008**, *10*, 6615.

[106] Staroverov, V. N.; Scuseria, G. E.; Tao, J.; Perdew, J. P. *J. Chem. Phys.* **2003**, *119*, 12129–12137.

[107] Cohen, A. J.; Mori-Sánchez, P.; Yang, W. *Chem. Rev.* **2012**, *112*, 289–320.

[108] Xu, X.; Goddard, W. A. *J. Phys. Chem. A* **2004**, *108*, 2305–2313.

[109] Howard, J. C.; Enyard, J. D.; Tschumper, G. S. *J. Chem. Phys.* **2015**, *143*, 214103.

[110] Gillan, M. J.; Alfè, D.; Michaelides, A. *J. Chem. Phys.* **2016**, *144*, 130901.

[111] Horvath, S.; McCoy, A. B.; Elliott, B. M.; Weddle, G. H.; Roscioli, J. R.; Johnson, M. A. *J. Phys. Chem. A* **2010**, *114*, 15561568.

[112] Sarka, J.; Lauvergnat, D.; Brites, V.; Császár, A. G.; Léonard, C. *Phys. Chem. Chem. Phys.* **2016**, *18*, 17678–17690.

[113] Roscioli, J. R.; Diken, E. G.; Johnson, M. A. *J. Phys. Chem. A* **2006**, *110*, 4943.

[114] Horvath, S.; McCoy, A. B.; Roscioli, J. R.; Johnson, M. A. *J. Phys. Chem. A* **2008**, *112*, 1233712344.

[115] Rheinecker, J.; Bowman, J. M. *J. Chem. Phys.* **2006**, *125*, 133206.

[116] Wang, X.-G.; Carrington Jr., T. *J. Chem. Phys.* **2002**, *117*, 6923.

[117] Wang, X.-G.; Carrington Jr., T.; J., T.; McKellar, A. R. W. *J. Chem. Phys.* **2005**, *123*, 034301.

[118] Wang, X.-G.; Carrington Jr., T. *RV4 is a package of programs to compute rovibrational levels and wavefunctions of tetra-atomic molecules*.

[119] Echave, J.; Clary, D. C. *Chem. Phys. Lett.* **1992**, *190*, 225–230.

[120] Wei, H.; Carrington Jr., T. *J. Chem. Phys.* **1992**, *97*, 3029–3037.

[121] Chen, R.; Guo, H. *J. Chem. Phys.* **2001**, *114*, 1467.

[122] Wang, X.-G.; Carrington Jr., T. *J. Chem. Phys.* **2001**, *114*, 1473.

[123] Bramley, M. J.; Carrington Jr., T. *J. Chem. Phys.* **1993**, *99*, 8519.

[124] Manthe, U.; Köppel, *J. Chem. Phys.* **1990**, *93*, 345.

[125] Cheng, X.; Steele, R. P. *J. Chem. Phys.* **2014**, *141*, 104105.

[126] Cheng, X.; Talbot, J. J.; Steele, R. P. *J. Chem. Phys.* **2016**, *145*, 124112.

[127] Wang, Y.; Bowman, J. M. *J. Chem. Phys.* **2011**, *134*, 154510.

[128] Brown, S. E.; Gtz, A. W.; Cheng, X.; Steele, R. P.; Mandelshtam, V. A.; Paesani, F. *J. Am. Chem. Soc.* **2017**, *139*, 7082–7088.

[129] Jacob, C. R.; Reiher, M. *J. Chem. Phys.* **2009**, *130*, 084106.

[130] Wang, Y.; Shepler, B. C.; Braams, B. J.; Bowman, J. M. *Chem. Phys. Lett.* **2010**, *491*, 1.

[131] Wang, Y.; Bowman, J. M. *J. Phys. Chem. Lett.* **2013**, *4*, 1104–1108.

[132] Thole, B. T. *Chem. Phys.* **1981**, *59*, 341–350.

[133] Duijnen, P. T. v.; Swart, M. *J. Chem. Phys. A* **1998**, *102*, 2399–2407.

[134] Partridge, H.; Schwenke, D. W. *J. Chem. Phys.* **1997**, *106*, 4618.

[135] Sneen, R. A. *Acc. Chem. Res.* **1973**, *6*, 46–53.

[136] Pregel, M.; Dunn, E.; Nagelkerke, R.; Thatcher, G.; Buncel, E. *Chem. Soc. Rev.* **1995**, *24*,

449–455.

[137] Nahar, S.; Tajmir-Riahi, H. *J. Inorg. Biochem.* **1995**, *58*, 223–234.

[138] Woodson, S. A. *Curr. Opin. Chem. Biol.* **2005**, *9*, 104–109.

[139] Draper, D. E. *Biophys. J.* **2008**, *95*, 5489–5495.

[140] Siuzdak, G.; Ichikawa, Y.; Caulfield, T. J.; Munoz, B.; Wong, C. H.; Nicolaou, K. *J. Am. Chem. Soc.* **1993**, *115*, 2877–2881.

[141] Tan, Z.-J.; Chen, S.-J. *Biophys. J.* **2006**, *91*, 518–536.

[142] Nostro, P. L.; Ninham, B. W. *Chem. Rev.* **2012**, *112*, 2287 – 2322.

[143] Endo, M. *J. Pharm. Sci.* **2006**, *100*, 519–524.

[144] Orlov, S.; Hamet, P. *J. Memb. Biol.* **2006**, *210*, 161–172.

[145] Harrison, R. G.; Tammet, H. *Space Sci. Rev.* **2008**, *137*, 107–118.

[146] others,, et al. *Nat. Commun.* **2016**, *7*, 11594.

[147] Winter, M.; Brodd, R. J. *Chem. Rev.* **2004**, *104*, 4245.

[148] Pollard, T. P.; Beck, T. L. *Curr. Opin. Colloid Interface Sci.* **2016**, *23*, 110 – 118.

[149] Bakker, H.; Kropman, M.; Omta, A. *J. Phys. Condens. Matter* **2005**, *17*, S3215.

[150] Jungwirth, P.; Tobias, D. J. *Chem. Rev.* **2006**, *106*, 1259–1281.

[151] Combariza, J. E.; Kestner, N. R.; Jortner, J. *J. Chem. Phys.* **1994**, *100*, 2851.

[152] Xantheas, S. S. *J. Phys. Chem.* **1996**, *100*, 9703–9713.

[153] Ayotte, P.; Bailey, C. G.; Weddle, G. H.; Johnson, M. A. *J. Phys. Chem. A* **1998**, *102*, 3067.

[154] Choi, J.-H.; Kuwata, K. T.; Cao, Y.-B.; Okumura, M. *J. Phys. Chem. A.* **1998**, *102*, 503–507.

[155] Ayotte, P.; Weddle, G. H.; Kim, J.; Kelley, J.; Johnson, M. A. *J. Phys. Chem. A.* **1999**, *103*, 443–447.

[156] Ayotte, P.; Nielsen, S. B.; Weddle, G. H.; Johnson, M. A.; Xantheas, S. S. *J. Phys. Chem. A* **1999**, *103*, 10665–10669.

[157] Lee, H. M.; Kim, D.; Kim, K. S. *J. Chem. Phys.* **2002**, *116*, 5509.

[158] Robertson, W. H.; Johnson, M. A. *Annu. Rev. Phys. Chem.* **2003**, *54*, 173–213.

[159] Ayala, R.; Martinez, J. M.; Pappalardo, R. R.; Marcos, E. S. *J. Chem. Phys.* **2004**, *121*, 7269.

[160] Kamarchik, E.; Bowman, J. M. *J. Phys. Chem. A* **2010**, *114*, 12945–12951.

[161] Toffoli, D.; Sparta, M.; Christiansen, O. *Chem. Phys. Lett.* **2011**, *510*, 36–41.

[162] Kamarchik, E.; Toffoli, D.; Christiansen, O.; Bowman, J. M. *Spectrochim. Acta. Part A* **2014**, *119*, 59–62.

[163] Wolke, C. T.; Menges, F. S.; Tötsch, N.; Gorlova, O.; Fournier, J. A.; Weddle, G. H.; Johnson, M. A.; Heine, N.; Esser, T. K.; Knorke, H.; Asmis, K. R.; McCoy, A. B.; Arismendi-Arrieta, D. J.; Prosmiti, R.; Paesani, F. *J. Phys. Chem. A* **2015**, *119*, 1859–1866.

[164] Feynman, R. P. *Statistical Mechanics*; Benjamin, 1972.

[165] Parrinello, M.; Rahman, A. *J. Chem. Phys.* **1984**, *80*, 860.

[166] Richardson, J. O. *J. Chem. Phys.* **2018**, *148*, 200901.

[167] Richardson, J. O.; Pérez, C.; Lobsiger, S.; Reid, A. A.; Temelso, B.; Shields, G. C.; Kisiel, Z.; Wales, D. J.; Pate, B. H.; Althorpe, S. C. *Science* **2016**, *351*, 1310.

[168] Laio, A.; Parrinello, M. *Proc. Natl. Acad. Sci.* **2002**, *99*, 12562–12566.

[169] Barducci, A.; Bussi, G.; Parrinello, M. *Phys. Rev. Lett.* **2008**, *100*, 020603.

[170] Tribello, G. A.; Bonomi, M.; Branduardi, D.; Camilloni, C.; Bussi, G. *Comput. Phys. Commun.* **2014**, *185*, 604–613.

[171] Pugliano, N.; Saykally, R. J. *Science* **1992**, *257*, 1937–1940.

[172] Keutsch, F. N.; Saykally, R. J. *Proc. Natl. Acad. Sci.* **2001**, *98*, 10533–10540.

[173] Keutsch, F. N.; Cruzan, J. D.; Saykally, R. J. *Chem. Rev.* **2003**, *103*, 2533–2578.

[174] Richardson, J. O.; Althorpe, S. C. *J. Chem. Phys.* **2011**, *134*, 054109.

[175] Wales, D. J. *J. Am. Chem. Soc.* **1993**, *115*, 11180–11190.

[176] Wales, D. J.; Walsh, T. R. *J. Chem. Phys.* **1996**, *105*, 6957.

[177] Wales, D. J.; Walsh, T. R. *J. Chem. Phys.* **1997**, *106*, 7193.

[178] Liu, K.; Brown, M. G.; Carter, C.; Saykally, R. J.; Gregory, J. K.; Clary, D. C. *Nature* **1996**, *381*, 501–503.

[179] Pérez, C.; Muckle, M. T.; Zaleski, D. P.; Seifert, N. A.; Temelso, B.; Shields, G. C.; Kisiel, Z.; Pate, B. H. *Science* **2012**, *336*, 897–901.

[180] Etacheri, V.; Marom, R.; Elazari, R.; Salitra, G.; Aurbach, D. *Energy Environ. Sci.* **2011**, *4*, 3243.

[181] Jungwirth, P.; Cremer, P. S. *Nature Chem.* **2014**, *6*, 261–263.

[182] Estillore, A. D.; Morris, H. S.; Or, V. W.; Lee, H. D.; Alves, M. R.; Marciano, M. A.; Laskina, O.; Qin, Z.; Tivanski, A. V.; Grassian, V. H. *Phys. Chem. Chem. Phys.* **2017**, *19*, 21101–21111.

[183] Hudait, A.; Allen, M. T.; Molinero, V. *J. Am. Chem. Soc.* **2017**, *139*, 10095–10103.

[184] Kelleher, P. J.; Menges, F. S.; DePalma, J. W.; Denton, J. K.; Johnson, M. A.; Weddle, G. H.; Hirshberg, B.; Gerber, R. B. *J. Phys. Chem. Lett.* **2017**, *8*, 4710–4715.

[185] Cochran, R. E.; Ryder, O. S.; Grassian, V. H.; Prather, K. A. *Acc. Chem. Res.* **2017**, *50*, 599–604.

[186] Baik, J.; Kim, H. M.; Majumdar, D.; Kim, K. S. *J. Chem. Phys.* **1999**, *110*, 9116–9127.

[187] Yoo, S.; Lei, Y. A.; Zeng, X. C. *J. Chem. Phys.* **2003**, *119*, 6083.

[188] Tobias, D. J.; Jungwirth, P.; Parrinello, M. *J. Chem. Phys.* **2001**, *114*, 7036.

[189] Wen, H.; Huang, T.; Liu, Y.-R.; Jiang, S.; Peng, X.-Q.; Miao, S.-K.; Wang, C.-Y.; Hong, Y.; Huang, W. *Chem. Phys.* **2016**, *479*, 129–142.

[190] Mallory, J. D.; Mandelshtam, V. A. *J. Phys. Chem. A* **2018**, *122*, 4167–4180.

[191] Geyer, C. J. *Markov chain Monte Carlo maximum likelihood, in: Computing Science and Statistics: Proc. 23rd Symp. Interface*; 1991; pp 156–163.

[192] Metropolis, N.; Rosenbluth, M. N.; Rosenbluth, A. H.; Teller, E.; Teller, J. *J. Chem. Phys.* **1953**, *21*, 1087.

[193] Wang, Y.; Huang, X.; Shepler, B. C.; Braams, B. J.; Bowman, J. M. *J. Chem. Phys.* **2011**, *134*, 094509.

[194] Egan, C. K.; Paesani, F. *J. Chem. Theory Comput.* **2018**, *14*, 1982–1997.

[195] Medders, G. R.; Babin, V.; Paesani, F. *J. Chem. Theory Comput.* **2013**, *9*, 1103–1114.

[196] Riera, M.; Brown, S. E.; Paesani, F. *J. Phys. Chem. A* **2018**, *122*, 5811–5821.

[197] Howard, J. C.; Enyard, J. D.; Tschumper, G. S. *J. Chem. Phys.* **2015**, *143*, 214103.

[198] Howard, J. C.; Tschumper, G. S. *J. Chem. Theory Comput.* **2015**, *11*, 2126–2136.